The Dissertation Committee for Timothy Thomas Diller certifies that this is the approved version of the following dissertation:

# Development, Characterization, and Modeling of an Electronic Particulate Matter Sensor for Internal Combustion Engines

Committee:

_____
Matthew J. Hall, Supervisor

_____
Ronald D. Matthews, Co-supervisor

_____
Ofodike Ezekoye

_____
Laxminarayan Raja

_____
Philip Varghese

# Development, Characterization, and Modeling of an Electronic Particulate Matter Sensor for Internal Combustion Engines

By

**Timothy Thomas Diller, B.S.; M.S.**

**Dissertation**

Presented to the Faculty of the Graduate School of

The University of Texas at Austin

in Partial Fulfillment

of the Requirements

for the degree of

**Doctor of Philosophy**

The University of Texas at Austin

December 2009

# ACKNOWLEDGEMENTS

I would like to express my sincere gratitude to my advisor Dr. Matt Hall, whose straightforward and forthright style gave me the right balance of independence and guidance. I hope to be able to strike the same balance in my own future career as an advisor of graduate students.

I would like to acknowledge the contributions of Prof. Raja and Prof. Matthews to the technical content of this work. I am grateful also to the other members of the committee, Prof. Ezekoye and Prof. Varghese for their time and input in reviewing this manuscript and agreeing to serve on my committee.

Thanks to Brett Henderson, Balky Nair, and Jim Steppan of Ceramatec for their involvement in the sensor development and paper writing efforts and to Phanindra Garimella and Bart Moffett at the Cummins Engine Company for their assistance in setting up and debugging the engine test stand.

Thanks to Curtis Johnson, Danny Jares, and Mike Slotboom in the machine shop for their fine work and plentiful advice. Thanks to the undergraduate researchers who helped in the lab: Sean, Sid, Vyshak, Sundeep, and Jeremy.

I am appreciative to VB, Brian, Ted, Jon, Chad, Jude, Murat, Kyung-Jin, Steffen, Jakob, and the rest of the members of the Engines Research Group for the companionship and camaraderie over the last four years.

The support of my parents Ken and JoAnn Diller has been invaluable in this graduate venture. Words will never suffice to express my gratitude.

Finally, and most importantly, I want to acknowledge the love, support, and longsuffering patience of my dear wife Hannah, and my children Ian, Eliza, and Caroline, who were my daily motivation to stay productive. Dear Ones, this is for you.

# Development, Characterization, and Modeling of an Electronic Particulate Matter Sensor for Internal Combustion Engines

Timothy Thomas Diller, Ph.D.
The University of Texas at Austin, 2009

Supervisor: Matthew J. Hall

U.S. Federal regulations requiring on-board diagnostics of diesel particulate filters have created a demand for compact, inexpensive, fast, and accurate sensors for measuring the particulate matter (PM) content of diesel exhaust. An electronic sensor capable of measuring the carbonaceous fraction (soot) of PM has been developed at The University of Texas at Austin. The behavior and performance of this sensor was characterized in both an older style non-emission controlled diesel engine and a modern heavy-duty diesel certified in 2008 to meet current federal emissions standards. The ability of the sensor to detect particulates at the regulated level of 15 mg/bhp-hr downstream of a leaking particulate filter was demonstrated. Under optimal conditions, the sensor was shown to have a resolution of 0.003 mg/bhp-hr, or 0.005 mg/$m^3$.

The sensor operated by measuring the flux of charged particles, ions, and electrons to an electrode immersed in an exhaust gas flow. Two distinct modes of operation were demonstrated. In the first, the sensor detected particles carrying residual charge from the combustion process. In this mode, the sensor was shown to be relatively insensitive to particle morphology and to be sensitive to exhaust gas velocity. In the second, charge carriers (particles, electrons, and ions) were created in the strong electric field produced by a second electrode at high voltage. In this mode, the sensor was found to be relatively insensitive to exhaust gas velocity, but quite sensitive to the orientation of

the sensor in the exhaust flow. The size and number density of the particles was found to have a strong influence on the sensor sensitivity: as number density increased with increasing load or decreasing EGR rate, so did sensor sensitivity. Thus, as changes in engine operating condition affect particle morphology, the behavior of the sensor changes. A numerical model of the discharge mechanism in the form of an atmospheric pressure glow discharge was implemented to model the charge creation and transport. The model accurately predicted the nanoamp-level electrode currents produced in a real sensor to within a half order of magnitude with no empirical fits. The model tended to over-predict the sensitivity of sensor output to applied voltage but matched the observed sensitivity within an order of magnitude. Due to the lack of modeling flow field effects it predicted a 250% increase in sensitivity for a gap width reduced by 50% where a comparison of real sensors showed a decrease in sensitivity of 25% with a 50% reduction in gap width.

# TABLE OF CONTENTS

# TABLE OF FIGURES

# Chapter I: Introduction and Background

## MOTIVATION

### Particulate Matter in the Environment

Airborne particulate matter (PM) is ubiquitous in the troposphere and originates from a wide variety of sources worldwide, both natural and man-made. "Particulate Matter" is a catch-all term which, according to the usual convention, comprises particles as small as 1 nanometer up to several tens of micrometers in diameter, that is, those particles which remain suspended in the atmosphere for more than a few hours. In general, the particles generated by human activity account for between 6-23% of the total content of PM in the atmosphere, depending on location. Depending on the size of the particles, they can remain suspended in the atmosphere for hours or weeks, but relative to gaseous pollutants, their atmospheric lifetime is relatively short. (The lifetimes of two important greenhouse gases, $CH_4$ and $CO_2$, for example, are measured in years and decades, respectively.) For this reason, the effects of particulate pollution are generally regional, although there are some important cases of long-distance atmospheric transport [1].

Among the more problematic of the types of PM are those generated in the combustion of fossil fuels, particularly those generated from mobile sources (vehicles), where capture of the particles is difficult due to the constraints of vehicle design. Among the mobile sources, diesel-powered vehicles are by far the largest producers of PM.

### Health and Ecological Impacts

Airborne PM has been implicated in a wide array of negative health conditions, particularly those involving respiratory ailments. A large body of research detailing the effects on human health has been synthesized by the U.S. EPA in the report "Health Assessment Document for Diesel Engine Exhaust"[2]. In summary, the health effects occur in both the short term and the long term. In the short term, exposure to particulates

in diesel exhaust can cause temporary irritation and inflammation of the respiratory pathways and can exacerbate existing conditions such as asthma and allergic symptoms. With chronic exposure, these inflammatory effects can lead to long-term respiratory and pulmonary problems.

Over the longer-term, the particulates in diesel exhaust have a particularly problematic effect. The particles in diesel exhaust generally have a layer of adsorbed compounds which include known carcinogens. $PM_{2.5}$, particulate matter with an effective aerodynamic diameter of less than 2.5$\mu$m, is not well filtered by the human respiratory system, making it ideal for deep lung penetration. $PM_{2.5}$ therefore acts as an effective carrier for the adsorbed carcinogens, leading to its classification as "likely to be carcinogenic to humans by inhalation." Certain geographic areas in particular tend to accumulate PM in the ambient air and are of special concern, such as inner-city urban areas and school parking lots, where idling by diesel powered school buses poses a particular health risk for children.

In addition to the impacts on human health, recent research has shown that airborne PM can disperse over long distances and that it therefore plays an important role in global warming. Although some aerosols are effective at reflecting radiation to space, diesel PM tends to be radiation absorbing. As much as 50% or more of the warming effect in some regions, particularly the Arctic, is due to black-carbon aerosols, through atmospheric radiation absorption and secondary reinforcing effects such as lowering of the albedo at glacial surfaces [3]. Thus, the control of diesel PM is important for human health, both through its direct effects and its secondary effects through the environment.

**Federal Emissions Regulations**

Federal air quality standards limit the emissions from motor vehicles of particulate matter (PM), oxides of nitrogen ($NO_x$), carbon monoxide, and hydrocarbons (HC's). For diesel engines, the pollutants of primary concern are PM and $NO_x$. A June 2005 final ruling by the U.S. EPA instituted a requirement for on-board portable

emissions measurement of PM for emissions certification of on-road diesel vehicles equipped with a diesel particulate filter (DPF). The ruling applies to both light-duty diesel vehicles, which are chassis certified, and heavy-duty diesel vehicles, for which the engine is certified on a dynamometer. For light-duty vehicles, the limit is 0.01 g/mi. The PM emission limit for heavy-duty engines is 0.01 g/bhp-hr. Heavy-duty vehicles are also required to carry an on-board diagnostic (OBD) system to detect a failure of the DPF resulting in emissions greater than 1.5 times the emission limit. Detailed specifications for the measurement of particulate matter from diesel engines is given in the U.S. Code of Federal Regulations, Title 40, Section 86, Subpart N. The sampled exhaust is diluted and brought below 52°C to precipitate gas-to-solid particulates and collected on a filter, the empty weight of which was carefully measured and for which the effects of ambient humidity are controlled through the use of a reference filter in contact with the ambient air [4]. Because certifications are detailed and very specific in protocol, they are carried out in a carefully controlled laboratory setting, and laboratory grade instruments are required for measuring the emissions with a high degree of precision for certification purposes.

One significant problem with the federal emission regulations is that, appearances to the contrary, the method is insufficiently specific to avoid a large variability due to the measurement method. This is especially the case for measurements made downstream of a DPF. The choice of filter material can affect the measured mass by a factor as great as 3.5. Similar variability can be demonstrated for differences in dilution ratio and sample temperature at the filter [1]. This variability is intimately related to the behavior of the aerosols in the exhaust gas, and the details of the measurement method have a substantial impact on whether the aerosols present constitute PM only or also other non-PM aerosols [5]. Thus, there is some speculation that the method specification may change and that a control of the rate of the number of particles emitted per unit power may also be implemented.

Future regulation is nearly certain to regulate the number of particles in addition to the mass of the particles emitted. Although the regulations are not yet established, early work on regulation development in the European Union and the trend toward harmonizing regulations for North America, Europe, and Japan indicates that limits of around $10^{11}$ #/kW-hr are a good guess at a future regulatory level for heavy-duty diesels [5].

**Exhaust After-treatment Systems**

To meet the Federal Emission Standards for particulate matter from diesel engines, diesel particulate filters are becoming increasingly common in after-treatment. Regulations are evolving such that all light-duty and heavy-duty diesel engines will require a DPF to meet the standards worldwide [5]. In 2010, engine makers will have to implement on-board diagnostic systems to detect a catastrophic failure of the DPF. In 2010, this standard will require detection of 4 times the limit for PM. In 2013 and after, this will change to detection of 1.75 times the limit. Thus, in order to meet the requirements for OBD, it is critical to have a sensor capable of detecting soot near the federal limit of 10 mg/bhp-hr that is portable, lightweight, inexpensive, and reliable.

Due to the tightening of federal standards for PM, vehicle emissions of PM have dropped dramatically. However, there has been a marked increase in the number of particles emitted by emission-controlled diesel engines, especially in the sub 2.5$\mu$m-diameter range[5,8,14]. Human health is most critically affected by particles smaller than 10 $\mu$m in diameter, and ironically it is these particles that are increasing so dramatically in number even as the mass of PM decreases in response to regulation, providing further motivation for regulation of PM in terms of number density as well as mass density in the near- to mid-term future.

## CHARACTERISTICS OF PM PRODUCED IN DIESEL ENGINES

### Theory of Formation

The combustion of diesel fuel in an engine happens in both premixed and diffusion modes. In a diesel-cycle engine, direct injection of fuel into the cylinder results in a gradient of fuel to air ratio. At the edges of the injection spray jet, the fuel vaporizes completely and mixes with the air in the cylinder in a turbulent region. Premixed flames form from the combustion of this completely vaporized fuel. Regions nearer the center of the jet either have a rich ratio of fuel to air or have incompletely vaporized fuel droplets. Combustion of this rich or incompletely vaporized fuel results in a diffusion flame since the combustion rate is limited by the rate at which oxygen can diffuse to the flame surface. Diffusion flame combustion is responsible for the formation of the bulk of the mass of PM emitted. At the temperatures present in the cylinder during fuel injection, various competing pyrolysis processes dominate when oxygen is scarce, that is, in the diffusion flame regions, leading to the formation of soot particles through a complex series of reactions.[1,6]

### Size & Number Distribution

Particles form in three primary modes: *nucleation*, in which hydrocarbons and sulfates nucleate into very small (< 50nm diameter) particles during cooling and diluting of the exhaust gas, which begins during expansion in the cylinder and continues in the exhaust pipe and in the mixing with ambient air; *accumulation*, primarily intermediate-sized (between 50nm and 500 nm) agglomerations of nucleation mode particles forming branched chain-like structures; and *coarse*, a relatively minor fraction of the overall PM consisting of large particles (> 500nm diameter) which build up on surfaces and are entrained in the exhaust due to flow pulsations. A size distribution typical of diesel engine exhaust pre-fuel-reformulation (2007) is shown in Figure I-1. Size distributions tend to follow log-normal distributions with one, two, or three peaks reflecting the three modes. The concentrations are substantially different for mass and number weightings as

noted in the figure.

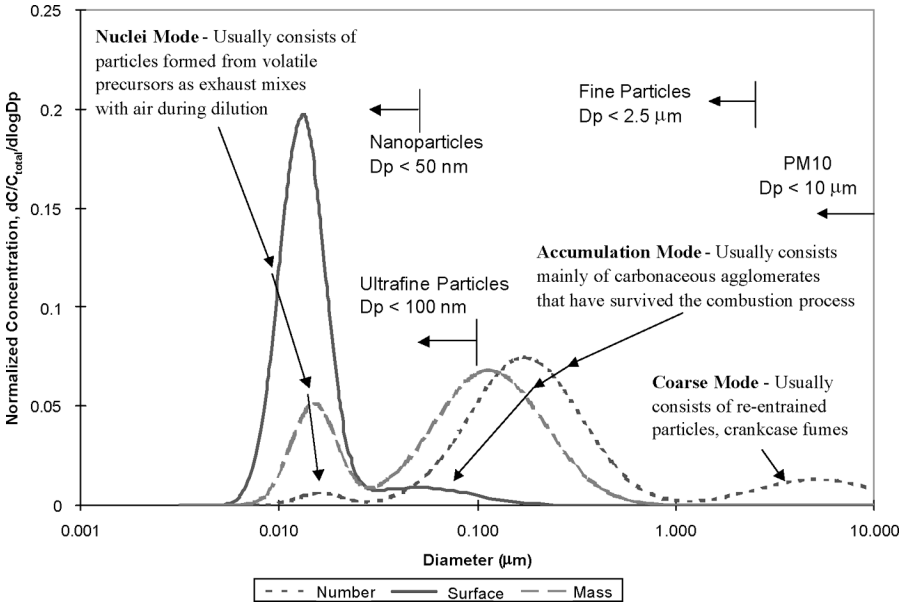


**Figure I-1 Typical engine exhaust size distributions showing both mass and number weightings [7].**

PM typically consists of a carbonaceous (soot) fraction, a soluble organic fraction (SOF) made up of various volatile components, typically originating in unburned fuel and oil, and a small fraction composed of metal and mineral ash. The fraction of fuel turned to PM as well as the size distribution of the resulting particles is sensitive to the initial composition of the fuel and the conditions in the cylinder during combustion. Depending on the fuel composition and the operation conditions, the SOF can make up from as little as 10% to as much as 90% of the overall mass of PM [8]. The reduction in 2007 of the maximum allowable sulfur content of diesel fuel from 500 parts per million (ppm) to 15 ppm brought about reductions in the emissions of PM. Lenni [9] observed reductions of 80-90% in the mass of PM emitted by buses operating on urban drive cycles. A study by Boehman et al. [10] showed that the SOF content stayed between 52-62% between low-sulfur, ultra-low-sulfur and biodiesel blends while overall PM mass dropped by 20-25% in a Cummins engine tested at steady state. Much of the PM mass reduction from

removal of sulfur from fuel is thought to be due to the reduction in $SO_3$ gas-to-particle reactions which provide critical nucleation sites for nucleation mode particle formation [1,8]. Additional minor sources of PM are the lubricating oil, which primarily contributes to the organic fraction, and ash, a byproduct of wear and the mineral component of lubricants and fuels.

The mass of soot produced per mass of fuel burned in a diesel engine is generally a function of the air-fuel mixing and the diffusion flame temperature according to the following relationship developed by Ahmad and Plee [11].

$$\frac{m_{soot}}{m_{fuel}} = C_{mix} \exp\left(\frac{E_a}{RT_f}\right)$$

where $C_{mix}$ is an empirical coefficient expressing the air-fuel mixing, $E_a$ is the activation energy, and $T_f$ is the diffusion flame temperature. Easley and Mellor [12] published data for a common-rail direct-injection diesel engine running at various conditions and found from 0.1 to 4 mg soot per g injected fuel. Values for $C_{mix}$ and $E_a$ were generally constant at a given operating condition, and the soot to fuel ratio was found to vary with flame temperature according to the relation above. Changes in intake air properties, and therefore in global equivalence ratio, were responsible for the variation in flame temperature.

PM evolution continues during the expansion and exhaust strokes, and down the exhaust pipe. A substantial evolution of the exhaust gas occurs after mixing with ambient air, when the sulfur and nitrogen compounds condense from the exhaust gases in gas-to-solid reactions, forming the bulk of the nucleation mode particles [1,8,13,14].

During the combustion process, the ion density is high in the cylinder. The soot particles formed in the accumulation mode become charged due to the ionizing environment. Rapid cooling occurs during the expansion and exhaust strokes of the engine, and the ionization state of the particles is frozen. Thus the accumulation mode particles carry residual, or *natural,* charge from the combustion process, typically

between 1 and 5 elementary charges [15]. Estimates of the fraction of particles charged by this process vary from 30%[16] to as high as 88% [15] of particles. The charge fraction of the particles depends on the fuel injection method (direct injection engines have higher charge fraction than indirect injection) and engine speed and load. Particles formed during dilution typically acquire charge slowly, if at all, through charge diffusion and do not carry a significant proportion of the charge in the exhaust and thus do not substantially change the charge density of the exhaust gas [7].

**Composition of PM**

The composition and size distribution of PM emitted from diesel engines operating in steady-state varies due to changes in operating conditions: load, engine speed, exhaust temperature, ambient humidity (and thus water content in the exhaust), injection pressure and timing, EGR, number of injections per cycle, and fuel type (sulfur content and feed-stock, petroleum or plant-based) all have an impact [13,17,18,19]. Transient operation introduces variability in the size distributions dependent on the specifics of the fuel injection system: swirl patterns, in-cylinder temperatures, and fuel/air ratios, all of which are varying in time. In general, both medium to high-load steady-state operation and accelerations tend to increase the relative distribution of accumulation mode particles, whereas at idle, during low load steady-state operation, and especially during decelerations, nucleation mode particle count and the SOF tend to increase [8]. The effect of dilution (from EGR or the low equivalence ratio at idle, for example) is generally to increase the number of nucleation mode particles [20]. However, the lack of sulfur in the fuel substantially reduces the formation of nucleation mode particles, in particular during steady-state operation.

The fuel used in the engines of this study was ultra-low sulfur diesel with sulfur concentration 15 ppm or less. In the time between this work and the prior work of Warey, the diesel fuel standard was changed, reducing the allowable sulfur concentration from 500 ppm to 15 ppm [21]. The impact of this fuel switch should be primarily on the

emission of the volatile precursors of nucleated sulfate particles. The effect on the carbonaceous accumulation mode particles is expected to be minimal [1].

**Influence of Engine Design**

The influence of engine design is also substantial. In general the reduction of PM mass emissions has not been accompanied by a reduction in the particle number emissions. Over time, in fact, control strategies implemented to reduce the PM mass emissions in order to meet regulation have resulted in a substantial increase in the number of particles emitted. Among the important changes in engine design that have impacted PM emissions have been electronic engine control and fuel injection pressure.

Kreso et al. [22] studied 10L Cummins engines from the model years 1988, 1991, and 1995, a time of rapid change in engine control and fuel injection technology to examine the effects of EGR on emissions. They found that "The total number of particles increased while the total volume of particles decreased from the 1988 to 1991 to 1995 engines." Total particulate concentrations for the 1988 engine were in the range of 27-37 $mg/m^3$, depending on the operating mode (EPA Modes 9 and 11 were tested), whereas the 1995 engine operating at similar conditions had total particulate emissions in the range 8-14 $mg/m^3$. The change in each case was attributed primarily to the reduction in the mass of solids emitted, not the organic fraction. Number densities, however, showed the opposite trend, with nearly two orders of magnitude increase from the 1988 engine to the 1995, from about $4x10^7$ particles/$cm^3$ to about $1x10^9$ particles/$cm^3$. Most of the number density increase came from nucleation-mode particles rather than accumulation mode particles.

**Effects of EGR**

The effect of EGR on both the mass and morphology of PM emissions is fairly well known from the literature [1,22,23-27]. EGR is used primarily as a method of reducing emissions of $NO_x$ from diesel engines, and it is generally accompanied by an

increase in the mass of PM emitted. While cooled-EGR systems limit this increase in PM to some extent, there is still a substantial increase in the mass, and a significant change in the size distribution of the particles occurs.

Kreso et al. [22] showed that adding 16% EGR reduced the number density of particles 24nm and smaller by two or more orders of magnitude while simultaneously increasing the number density of larger particles, especially those of 100nm and larger diameter. Desantes et al. [25] reported reductions up to 90% in the number density of <20nm particles in the exhaust of an 11L 6-cylinder turbo-charged heavy-duty diesel engine, dependent on the load and speed conditions. Particles having electrical mobility diameters greater than 40 nm universally increased in number with the addition of EGR. Additional work by Wagner et al [26] on a 1.9L 4-cylinder turbo-charged light-duty diesel engine corroborated these trends, although somewhat less dramatically due to their low load conditions and their EGR strategy, which kept the boost and fuel levels rather than the oxygen-fuel ratio constant. In all of the studies, it was the smallest particles whose number densities were most affected by the addition of EGR.

Lee, Zhu and Song [27] reported that with EGR systems that alter boost pressure to maintain the combustion stoichiometry, an increase of 92% in the total emitted PM mass has been seen at 13% EGR. They reported on the morphology of the particles using TEM microscopy and noted the change with EGR rate. Increasing EGR from 0 to 13% at constant oxygen to fuel ratio induced a 30% increase in the mean diameter of the primary particles from 16nm to 21nm, and a substantial decrease in the number of primary particles per aggregate, from 150 to under 50. While their study did not include overall number density, it suggests the importance of aggregation in the morphological changes that come with EGR.

### PM Sensing and Measurement Technologies

Methods for characterizing the size distribution and concentration of PM are based on several physical principles. Some methods physically trap the PM on a filter and

record the captured mass, as discussed previously. Others use the optical, aerodynamic, or electrical properties of the particles to determine their shapes, sizes, or densities. Additionally, some real-time estimation of particulate concentration or mass is done using computer algorithms. Each method is useful in a different kind of application, based on the requirements of precision, accuracy, cost and portability.

Nearly all laboratory-grade methods include some level of dilution, in order to simulate the mixing of exhaust gas with ambient air and the resulting condensation of the non-carbonaceous particles. Laboratory dilution is in reality constrained by the practical considerations of processing the diluted exhaust gas. In an exhaust stack emission, the dilution ratio is effectively infinite. The divergence of laboratory-dilution effects from real-world ambient air mixing decreases with lower concentrations of gas-to-solid precursors, namely $NO_X$ and $SO_X$ species.

**Conventional Methods**

Measurement methods which directly measure the mass of the particles are termed *gravimetric methods*. These methods generally involve an integral-type bulk measurement of the particles trapped on a filter through which the exhaust gas is drawn. For heavy-duty engines, the measurements are made at a series of steady-state operating conditions spanning the full operational map of an engine with respect to load and speed. Another type of gravimetric measurement records changes in the resonant frequency of a probe in the exhaust gas stream as individual particles attach and detach from the probe.

The EPA specifies a standard method of making measurements of particulate mass concentration in the laboratory using dilution and carefully controlled filters, as mentioned above. The method used in this work is described in detail later. In brief, it used weighed filters and direct sampling of undiluted exhaust gas. The EPA method was deemed impractical and inappropriate for reasons discussed later.

One gravimetric sampling system under development uses a partial flow dilution tunnel with real-time weighed filter measurements as part of a portable emissions measurement system (PEMS). It can reproduce the method specified by the EPA but is not yet capable of reliably detecting the federal not-to-exceed (NTE) levels for PM and suffers from filter contamination from NTE levels of PM. That is, having once exceeded the federal limit, it cannot then accurately measure sub-NTE PM levels. This is a laboratory grade instrument well suited to research, development, and certification of engines but far too expensive for real-time monitoring of in-use engines [28].

The tapered element oscillating microbalance (TEOM) sensor provides a time-resolved measurement for PM by measuring the change in resonant frequency of a filter attached to the end of a tapered element. Diluted PM-laden gas passes through the filter, and PM is deposited on the filter, changing its mass. The frequency response of the filter-tapered element system is determined by measuring the response to electronically excited oscillations in the tapered element. The accumulated mass on the filter can be calculated from well-understood principles of dynamics. The instantaneous mass emission rate (in mass/time) is given by differentiating the signal. TEOM sensors are sensitive to the absorption and desorption of the volatile components of PM and water in the exhaust and require careful control of the environmental variables, but they are one of few direct measurements of particulate mass; they provide an *instantaneous* measurement of mass content of a gas, and their output correlates well to gravimetric measurements. Because of their complexity, expense, and sensitivity to vibration, humidity, and other factors, they must be carefully isolated from their environment and are generally only suited to laboratory-based measurements, not on-vehicle operation [1,29]

Quartz crystal microbalance (QCM) sensors operate on a similar principal to TEOM sensors by measuring the change in resonant frequency of a piezo-electric quartz crystal exposed to diluted PM-laden exhaust flow. Continuous adsorption and desorption of soot particles onto the surface provide a real-time measurement of the mass-concentration of PM in the exhaust flow. QCM sensors may be more robust with respect

to environmental sensitivity but suffer from a limited range of sensitivity, a problem, the importance of which may be decreasing as engine emission levels continue to decrease. Portable sensors of this type are available for on-road testing, but due to the system size and cost, they are unsuitable for inclusion in mass production vehicles [30].

**Electrical Methods**

Various types of sensors take advantage of the electrical properties of soot particles, including the sensor studied in this work.

The spark discharge soot sensor (SDSS) is a type of sensor under development. It operates by measuring the changes in minimum spark discharge voltage due to varying levels of soot in the exhaust gas. Many cross-effects must be accounted for including mass flow rate, A/F ratio, and temperature, but a signal with a 5 (ms) time resolution is possible. At the time of publication the SDSS could discriminate PM levels of 10's of ($mg/m^3$) but was sensitive to soot deposition on the sensor and is most reliable for exhaust temperatures below 350°C [31].

An electronic PM sensor similar to the one studied in this work is under development at the *Hochschule für Technik und Wirtschaft* Dresden for use in on-board diagnostic of DPF's in off-road vehicles. It differs principally from the sensor described in this work in that it uses a higher electrode voltage of the opposite polarity (-1500V), and multiple flat planar electrodes. As of 2008 there was no peer-reviewed literature describing its function [32].

**Mobility Methods**

Two types of particle sizing instruments classify particles according to their mobility: one based on the balance of aerodynamic and inertial forces, the other based on a balance of aerodynamic and electrical forces.

Inertial impactors use the inertia of particles to separate them into classes. In an impactor, a particle laden flow of gas is required to follow a serpentine path. Particles too heavy to follow the flow impact a collector plate, thus the gas flow is rid of particles above a certain mass, or more accurately, of particles whose mobility is too low to follow the flow. Typically, sets of serpentine paths and collector plates are arranged in series to collect and classify entrained particles of progressively lower mass. Such an instrument is called a cascade impactor. Because the collector plate can be weighed, it is a direct measurement of PM mass and can be termed a gravimetric method. The technology is mature, and several varieties have been commercialized and are available on the market, including the electrical low-pressure impactor (ELPI) and micro-orifice uniform deposit impactor (MOUDI). These instruments can classify particles with aerodynamic diameters in the range of 30nm to 10$\mu$m, limiting their effectiveness for nucleation-mode particles. [1]

In an electrical mobility analyzer, particles in the stream to be analyzed are charged, typically in a corona discharge, and directed into a chamber with an electric field gradient. Particles of a certain electrical mobility are captured by a sampling tube and counted, usually with an optical method such as condensation nuclei counters discussed in the next section. By changing the electric field strength and altering the geometry of the sampling tube, a range of electrical mobilities can be scanned, and in this manner, a distribution of sizes can be inferred from the number densities at the different electrical mobilities sampled. Electrical mobility analyzers can be used to produce mono-disperse aerosol streams, which can be useful in the study of PM and aerosols in general. Instruments using this concept include the electrical aerosol analyzer (EAA), scanning mobility particle sizer (SMPS), differential mobility particle sizer (DMPS) and differential mobility analyzer (DMA). The size range of particles treated ranges from 7nm to 1$\mu$m, although few instruments manage that entire range, and often they must be used in tandem to gain complete coverage. [1]

**Optical Methods**

Several methods of characterizing PM take advantage of the optical properties of aerosols. In a condensation nuclei counter (CNC) or condensation particle counter (CPC), a fine alcohol mist is sprayed into diluted exhaust gas. The alcohol condenses on the particles and increases their apparent size until the particles achieve a more or less uniform diameter of roughly 10$\mu$m. The particles then pass in front of an illumination source and photo detector that makes use of Mie scattering to count the number of particles. CNC's cannot of themselves establish a size distribution but rather would be paired with another instrument providing a mono-disperse aerosol for that function. [1] Various other schemes exist for the classification of particles using Mie scattering, which in greatly oversimplified terms, infer the size of particles based on the polarization or angle of scattered laser light [33,34]. In practice, Mie scattering devices are most useful for characterizing mono-disperse aerosol streams of particles which are not highly agglomerated due to assumptions about the shapes of the particles.

Other Mie scattering methods add some information by controlling the polarization of the laser illumination [35], including current research on measuring soot whose mean particle size is at the nanometer scale. As exhaust PM decreases in mass, the particle size tends to decrease and the number densities tend to rise. Traditional gravimetric methods are not sensitive to nanoparticles, and traditional optical methods are subject to wavelength considerations. A polarization modulated scattering (PMS) system [36] uses variably polarized laser beams and intensive numerical algorithms to infer the PM characteristics, including fractal dimension, radius of gyration, and refractive index, from which size and mass distributions can be calculated. As of 2009, results of the experimental application of this method to engine-out emissions have not been published, so the sensitivity and accuracy of the method is not established.

### Predictive Modeling Methods

One important function of PM sensing is to estimate the soot-loading in a DPF, both for thermal management and to optimize and minimize fuel-consuming regeneration cycles. In 2009, this is primarily accomplished via computational models. One representative estimation method relies on empirical models of engine-out emissions and soot oxidation behavior. While characterization of engine-out emissions during steady-state is straightforward, accurately predicting the emissions during transient events is much more problematic. This leads to the necessity of running a very conservative (but fuel liberal) regeneration strategy. Another soot-loading estimation method uses a physical model combined with measurements of the pressure drop across the DPF and other parameters. While this type model has the advantage of closed-loop control, the sensitivity of the model to pressure drop varies with operating condition, and because the pressure drop across the DPF is an inherently noisy signal, it suffers from high uncertainty under certain operating conditions. There are challenges to using pressure drop as a feedback signal, however: pressure drop is a function of other operational parameters (exhaust gas temperature, for example) in addition to soot loading. This demonstrates the desirability of a method for the direct measurement of soot for DPF control and management [37].

## RESEARCH PROGRAM CONTEXT

In light of the advances of engine technology and the tightening restriction on PM from diesel engines and particularly in light of the requirement for on-board diagnostic of DPF operation, there was a need in the marketplace for a sensor that could operate in real-time on-board a vehicle that was light-weight, inexpensive, accurate and robust. In that context, the U.S. Department of Energy (DOE) funded a project at The University of Texas at Austin to develop such a sensor in cooperation with an engine-maker and a commercial partner capable bringing of the technology to market. This research, then, was carried out with funding provided by the U.S. DOE in cooperation with the Cummins Motor Company and Ceramatec, Inc., a subsidiary of Coorstek specializing in the

development and manufacture of ceramic-based sensors. Work for this doctoral dissertation was carried out as a part of that program with the purpose of both advancing the design of the sensor and increasing the understanding of the physical mechanisms underlying its operation. The most immediate market demand was for a sensor that could be used as an OBD tool for DPF failure, but the long-term view for sensor development was to enable monitoring and control of combustion in diesel and HCCI engines.

Chapter II of this dissertation begins with an overview of the function of the sensor and presents a history of the design of the sensor. In Chapter III, the experimental setup is described in detail, including the test engines the steady-state rig, and a gravimetric sampling system. Chapter IV consists of three sections. In the first, the behavior of the sensor is described in detail with respect to its operation in the test engines and test rig under various transient and steady-state operating conditions. Based on those observations, physical models for the sensor's two primary operating modes are proposed in the second section. In the third section of the chapter, quantitative relations are developed for the physical models, including a MATLAB-based numerical simulation of the discharge event. Chapter V discussion a summary of the findings and a discussion of the applications of the sensor, including on-board diagnosis of diesel particulate filters and potential future uses in engine control. Finally there are suggestions for future study of the sensor.

# Chapter II: Design and Function of the Sensor

## OVERVIEW

A schematic drawing of the electronic PM sensor is shown in Figure II-1. The sensor consists of a pair of electrically isolated metal electrodes separated by an air gap. The electrodes are contained within a housing and installed in the engine exhaust system with the electrodes protruding into the exhaust flow.

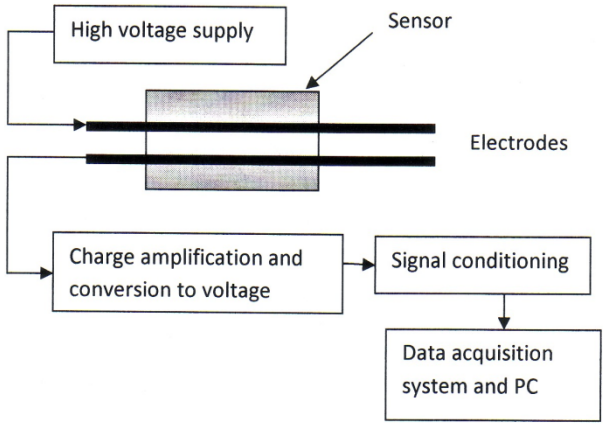


**Figure II-1 Operational schematic of the electronic particulate matter sensor**

One of the electrodes, termed the *field electrode*, is held at 1000 VDC. The other electrode, the *sensing electrode*, is connected to charge amplification circuitry. The high-voltage field electrode creates a strong electric field in the region between the two sensor electrodes. Using QuickField 5.6, a software program for calculating electric field intensity based on 2D geometry, an electric field intensity map, shown in Figure II-2, was created using typical sensor geometry: electrodes of 1mm diameter, a 1mm gap between the electrodes, and a 1000 VDC applied voltage. The field electrode is labeled "F" and the sensor electrode is labeled "S".

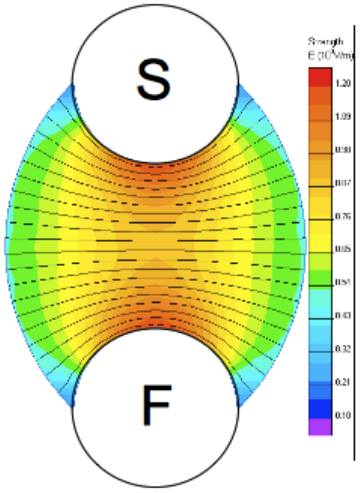


**Figure II-2 Electric field intensity in the sensor electrode gap**

A uniform field with 1000V potential and a 1mm gap would have an intensity of $1x10^6$ V/m. Due to the curvature of the electrodes, the actual maximum field intensity in the sensor gap is inhomogeneous, with an intensity about 1.2 times higher, at $1.2x10^6$ V/m, than would be present in a uniform field with the highest intensity concentrated near the inward-facing electrode surfaces. The intensity drops in the circumferential direction such that the mean field value over the inward facing half of the electrode is about 55% of the uniform field intensity. The sensor works by measuring the flux of charge carriers to the sensor electrode.

A schematic of the charge amplification circuitry is shown in Figure II-3. The circuit consisted of three operational amplifiers, designated U1, U2 and U3. The first, U1, was set up in a charge amplifying configuration, converting charge at the sensing electrode to a voltage. The second op-amp, U2, inverted and scaled the signal by means of an adjustable potentiometer. The third op-amp provided a means of adjusting the baseline trim, or offset voltage level. According to calculations with SPICE, the time constant of the overall amplifier package was 20ms, corresponding to about 240 crank angle degrees for an engine operating at 2000 RPM. In order to eliminate the signal variation due to cycle-to-cycle variation in combustion, however, passive low-pass

electronic RC-type filters were used, with cutoff frequencies of 23 Hz for higher-speed measurements or 0.2 Hz for steady-state measurements.

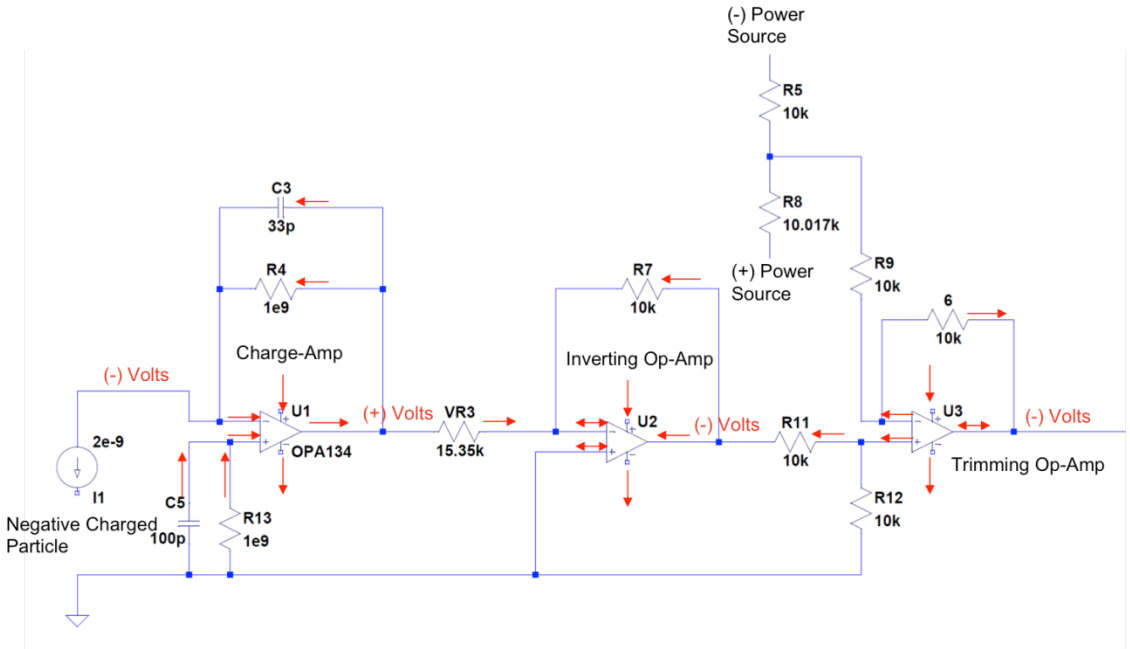


**Figure II-3 Charge amplification circuitry connected to the sensing electrode.**

The gain of the amplification circuitry was set after adjusting trim to zero by connecting the signal input to the +15VDC power supply through a 1000MΩ resistor, providing a $15 \times 10^{-9}$A current, corresponding to a flow of $9.4 \times 10^{10}$ fundamental charges per second. The potentiometer VR3 was adjusted until the output voltage from the circuitry was 8V. 8V was chosen as the maximum output voltage early in the research program due to a limitation of the voltage range of the data acquisition system on the DYNOmite dynamometer, and to avoid confusion the scale was not changed later in the program when a different, more capable data acquisition system was implemented.

## DESIGN HISTORY

Much of the design work on the sensor focused on two primary areas: increasing sensitivity and preventing fouling of the electrodes in soot laden exhaust. Much of the initial work on increasing sensitivity was completed by Warey [43,44,45]. Through this

work it was determined that the output voltage, $V_O$, of the sensor varied approximately linearly with the mass concentration, C ($g/m^3$), of the carbonaceous PM in the exhaust. The sensor response depended on the separation distance between the two electrodes, S (m), the applied bias voltage, $V_B$, the electrode length, L (m), and the flow velocity, U (m/s). The dry soot concentration in the exhaust for any engine operating condition and sensor geometry was found to follow the relationship:

$$C\left[\frac{g}{m^3}\right] = \frac{V_0 S^{1.28}}{5.75\times10^{-5} L V_B e^{0.62U}}$$

This relation was created through a correlation of sensor response with filter measurements of non-volatile PM mass concentration [43]. According to that correlation, the sensitivity of the sensor increased exponentially with exhaust velocity.

Electrode fouling presented a substantial challenge to sensor development, especially during early testing on engines with high soot emissions. Fouling of the electrodes resulted in two distinct kinds of failure of the sensor. First, because the soot was conductive, it could form a path of conduction between the two electrodes, causing the signal from the sensor to drift higher until it saturates amplifiers. Not only did this render the signal useless, but it could also eventually lead to damage of the signal conditioning circuitry. This kind of fouling usually manifested itself as a sharp increase in the sensor signal after a sooty event, such as a high-load tip-in.

Second, because the sensitivity of the sensor was proportional to the strength of the electric field between the electrodes, an accumulation of soot on the electrodes could modify the electric field and thus the sensitivity. This effect was particularly evident in flows with very dry soot, where the accumulated soot tended to form needle-like structures on the electrode surface. The electric field was concentrated at such needles, and the sensitivity of the sensor increased with time due to the increasing strength of the electric field. Figure II-4 shows such a change in sensitivity. A sensor was placed in the

exhaust pipe of a static test rig in which soot from a diesel fuel diffusion flame was mixed with dilution air. Because of the flame type, in which only evaporated fuel burned, the volatile content of the PM was near zero, and the particles had a long and branched structure which readily formed dendrite structures on the electrode surface. The spike in the signal in (a) at t=30 seconds was due to switching on the electric field. The noise in the signal was 60Hz noise due to using an unshielded PVC pipe. The long-term trend of this kind of fouling was either to come to a noisy steady-state asymptote, as seen in (b) when the dendrites alternately formed and then broke off due to aerodynamic drag from the free-stream flow or to concentrate the electric field enough to cause a saturation of the signal or arcing, resulting in destruction of the amplification circuitry. Although this behavior was most strikingly seen when a sensor was measuring the dry soot present in the static rig, it was also evident to some degree when a sensor was placed in a very sooty engine-exhaust stream.

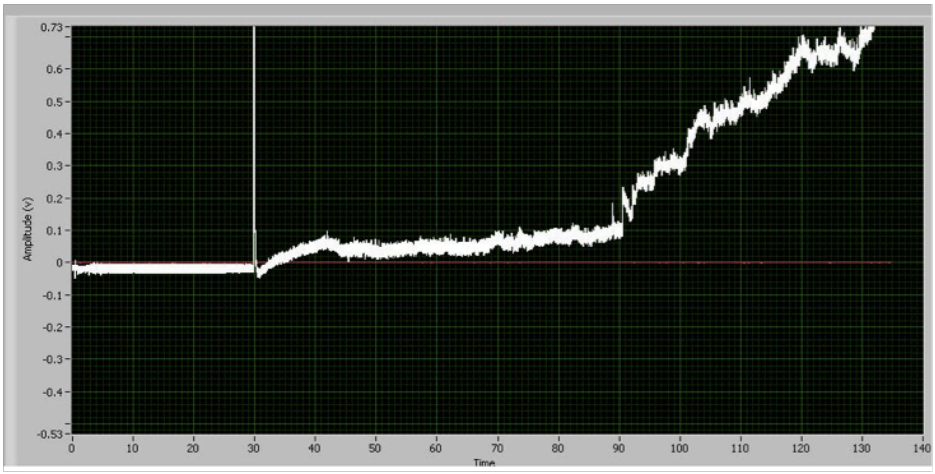


(a)

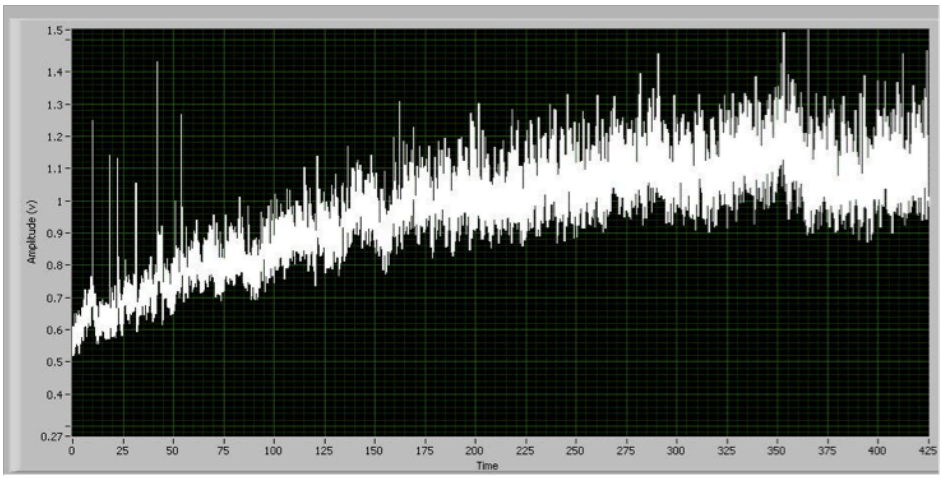


(b)

**Figure II-4 Examples of electrode fouling due to soot accumulation on the electrode surfaces in the dry soot of a diesel wick flame.**

In early designs, a fouling-prevention strategy was to insulate part of the electrode with a polymer shield in the form of heat shrink or Teflon tubing. This approach was ultimately abandoned because the PM adhered to the polymer and would form a conductive path between the electrodes over the outsides of the insulation. Additionally, the exhaust gas temperature at higher loads exceeded the melting point of the insulation, limiting the operational range of the sensor.

After that, various methods of lengthening or protecting the path between the electrodes were attempted. In one design (topmost in Figure II-5 below), the base of the electrodes was contained in a plenum that was supplied with pressurized air. The air flow through gaps around the electrode prevented penetration of soot to the electrode base and thus the formation of a conductive path between the electrodes. This method worked well for preventing the formation of the conductive path but had other shortcomings and introduced additional problems. The cap of the plenum was formed of a rubberized gasket material and was glued in place. It was subject to both high temperatures and high vibrations and thus had a limited useful life and required periodic replacement. In addition, retracting the base of the electrodes so far into the body of the sensor increased

the unsupported length of the electrodes and created a sensitivity to vibration. When the sensors were shaken, at least one of the vibration modes effectively changed the electrode gap distance on a periodic basis and thus affected the sensitivity. In addition, while the air-purge method was effective in preventing the formation of a conductive path between the electrodes, it did not prevent the accumulation of soot on the electrodes themselves and thus only protected against the first mode of electrode fouling.

**Figure II-5 Three early sensor designs: air-purge, ceramic labyrinth, and heated ceramic with foil electrodes**

A second example of this strategy is shown in the middle sensor of Figure II-5. In this design, the brass wire electrodes were housed inside ceramic tubes and glued in place at the back (leftmost in the photo) end of the sensor. Thus, for a conductive path to form, PM would have to penetrate the length of both ceramic tubes. In practice, this type of sensor was successful in avoiding the first type of fouling but still subject to the same kind of vibration problems as the air-purged type.

A more successful approach to managing the fouling of the electrodes was to mount a foil electrode on a ceramic tube substrate and use Ni-Cr wire heaters to keep the ceramic hot enough to vaporize soot particles which adhered to the surface. With careful arrangement of the heater windings and electrode geometry, it was possible to heat the ceramic tube to evaporate or oxidize accumulated soot.

Unfortunately, the electrical conductivity of ceramics is a function of temperature, and at around the temperature required to evaporate the soot, the conductivity of even the highest purity alumina ceramics was high enough to affect the sensor signal. The current levels measured by the sensor were on the order of $10^{-8}$A. Thus, to sufficiently (< 1% error) insulate the sensor electrode from a heater wire at 12V, a resistivity of at least $1.2x10^{11}$ Ω-cm was required, assuming the wall thickness of the alumina tube was 1mm. Kingery published a resistivity curve for several oxide ceramics [38], shown below in Figure II-6.

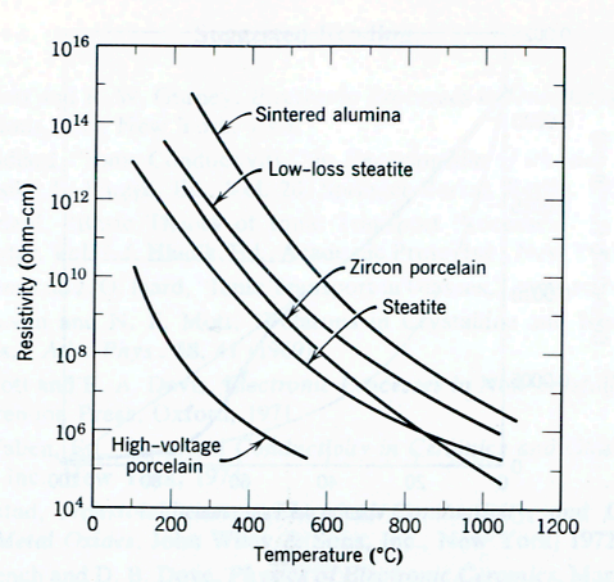


**Figure II-6 Reduction in resistivity with temperature in representative oxide ceramics [38]**

Alumina maintained the highest resistivity among the oxide ceramics and indeed among almost all materials, yet its resistivity dropped to the critical level at around 550°C. During a table-top measurement with an infra-red thermometer, the minimum temperature for evaporating or oxidizing soot from the ceramic was measured at about 550-600°C. When in this heated condition, the sensor output drifted considerably, and responded in the short term to variations in the heater voltage. Given time to cool down either with the heater off or with a flow of cool air, the ceramic lost conductivity and no

longer leaked current from the heater coil. Installed in an exhaust pipe, the behavior was a little less straightforward due to variation of the temperature and speed of the exhaust gas. With varying convective environments, the heaters would interfere with the signal under some circumstances and not under others.

Although much effort was spent to fine tune this system, it eventually proved not to be a big problem in cleaner exhaust flows: particulate concentrations from the Cummins exhaust were insufficient to foul sensors in tens of hours of testing without heaters energized, and downstream of the DPF, the concentrations were low enough that fouling was not expected to be a problem at all. It was thought that installed downstream of a DPF, no heater was necessary since regeneration of the DPF would produce gases hot enough to oxidize soot from a ceramic substrate. The heater would regenerate with the DPF. Confirmation of this through long-term testing and fine-tuning of sensor heaters for installation upstream of a DPF was left to a commercial development program.

In the final stage of testing, sensors manufactured by Ceramatec, Inc as prototypes were tested. An example of this type of sensor is shown in Figure II-7. The electrodes consisted of platinum-coated ceramic tubes with the leads brazed to the end and passing through the core of the tube. Ni-Cr wire heaters were wrapped around the base of the electrodes. After extended testing under certain operating conditions such a high EGR rates and low loads, a sensor could start to show a baseline drift indicative of the conductive-path type of fouling. The sensor could be regenerated by powering the heater at about 35W for five to tens minutes, after which the baseline would return to normal. During the regeneration event, the sensor signal was unusable due to the conductivity of the ceramic tubes.

**Figure II-7 Prototype sensor produced by Ceramatec for commercial testing.**

A shroud encased the electrodes to protect them from human contact and guard against debris in the exhaust pipe. Flakes of caked soot could break off from the exhaust pipe walls, and if one fell between the two electrodes, it would provide a conductive path that would lead to arcing and failure of the electronics.

# Chapter III: Experimental Setup

Testing of the sensor reported in this dissertation was carried out on three separate test rigs, and the results have been published in four publications [39-42]. The initial work was done on a single-cylinder industrial diesel engine made by the Yanmar America Corporation. The Yanmar engine was characterized by PM emissions that were substantially higher than those from modern, low-emission engines intended for the sensor, but important insights were gained from testing and developing sensors in its exhaust. Simultaneous to the single-cylinder engine measurements, the sensor was tested in a steady-state rig designed to eliminate the effects of flow pulsations and to examine the effects of flow velocity in detail. Some important qualitative insights were gained, but the data obtained in the rig had limited quantitative value. Ultimately the soot generated in the rig was substantially different from soot generated in diesel engine combustion, so only limited effort was put into obtaining results in this setup.

Testing in final part of the research program was conducted on a 6.7L displacement medium-heavy duty engine loaned by the Cummins Engine Company. The engine was from the ISB-350 family of Cummins engines and was of the type commonly found in medium-duty (Class 5 and 6) trucks such as urban delivery trucks or emergency vehicles. The engine was certified to meet the federal emissions standards in the model year 2008. Installation of a DPF allowed testing of the sensor in its intended application of on-board diagnostic measurement of DPF performance.

In each measurement setup, a gravimetric filter sampling system was used to directly measure the mass concentration of soot in the exhaust gas. The difference in filter mass before and after a known volume of gas was drawn through it yielded the mass of particulates. Mass concentration was given by dividing the particulate mass by the sample volume, and these measurement were the standard against which sensor calibrations were made.

**SINGLE CYLINDER YANMAR DIESEL**

Testing by Warey [43-45] and in the first part of this work was done on a single cylinder diesel engine, model L100AE-DE made by Yanmar. The engine, shown in Figure III-1 below, has a displacement of 0.407L and is rated 6.6kW (9.0bhp) continuous output at 3600 RPM or a peak output of 7.5kW (10.0bhp) at 3600 RPM. Its bore and stroke are 86mm and 70mm, respectively, and the fuel injection is direct, in-cylinder. The L100AE-DE was not EPA emissions compliant.

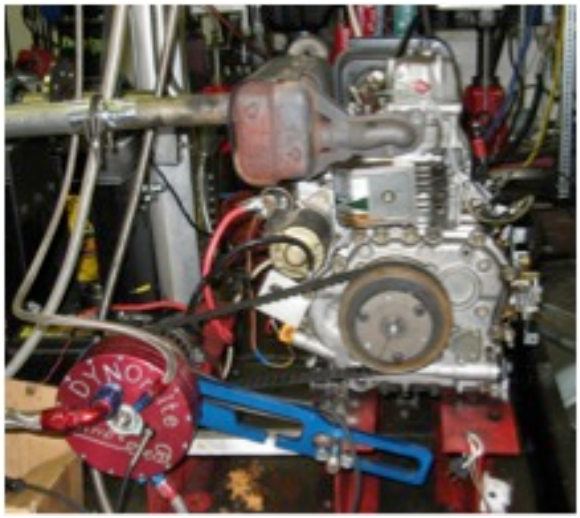

**Figure III-1 Yanmar L100AE-DE 0.407 L Single Cylinder Engine, shown with original muffler and torque arm.**

The load on the Yanmar engine was determined by its fueling rate, adjusted with a set-screw and spring mechanism and by controlling the resistive load on its output shaft with a small engine dynamometer. Torque control was accomplished via a DYNOmite water-brake absorption-type dynamometer made by Land & Sea, Inc. The DYNOmite dynamometer was equipped with a software-controlled water flow valve which varies the flow of water through the water brake. The water brake itself consisted of a fixed-gap rotor and stator system. Torque was produced on the input shaft based on the diameter of the outlet orifice, the rotor speed, and the ratio of water to air in the brake. Torque was measured using a strain gauge and lever arm attached to the body of the water brake.

Although the DYNOmite was equipped with DYNOmax control and DAQ software, the limited data acquisition rate and difficulty of adding new data channels with that software led us to custom build a control and DAQ system. The servo-operated water-flow control valve became difficult to use due to internal corrosion, so it was replaced with a manually operated globe valve. The DYNOmax DAQ system was limited to a time resolution of 20Hz sampling frequency, which was insufficient for capturing transient events, so an alternative was developed using a Measurement Computing USB-1608F DAQ board and control software developed in the National Instruments (NI) LabView environment. Sampling speed with the LabView system could be specified as high as 20kHz with 5 analog channels recorded. A sampling rate of 500Hz was sufficient for capturing most transient events, and for steady state measurements, 50Hz or 20Hz was used, to keep the data file size manageable for long-duration tests.

Because the strain gauge amplification circuitry for the original DYNOmite torque sensor was incorporated into the DYNOmite control hardware, the torque signal was not accessible to the LabView based DAQ system, so a separate strain gauge was used for torque measurements. The torque arm and strain gauge arrangements are shown in their original and modified configurations in Figure III-1 and Figure III-2, respectively. The original strain gauge was located in the blue anodized torque arm out of sight behind the body of the dynamometer. The replacement strain gauge was placed between the end of the torque arm and the engine mount.

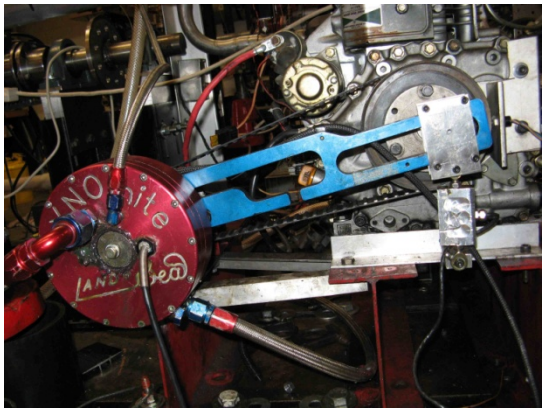

**Figure III-2 Torque arm arrangement on the Yanmar single-cylinder engine**

To measure engine speed, a Hall-effect sensor was mounted so that it measured the toothed drive gear on the engine output drive shaft. Conversion of the pulse train to engine speed calculation was typically done in post processing to improve time-resolution: due to a quirk of the DAQ system, engine speed could not be written to output at the same sampling frequency as the other data, but it was calculated real-time for on-screen display and engine control. Later grinding down of one tooth on the 36-tooth drive gear enabled determination of crank angle with a resolution of +/- 5° since top dead center (TDC) could be determined from the location of the missing tooth, and rising and falling edges from the Hall effect sensor gave the locations of the remaining teeth and gaps. A further increase in the resolution was possible through interpolation of data points across a tooth or gap, but the accuracy of this method was somewhat limited.

Sensor ports were installed at various distances downstream of the exhaust port, as shown schematically along with pipe diameters in Figure III-3. At 1.7m downstream, a pair of ports was installed opposite each other so that effective comparisons of pairs of sensors could be made in the exhaust at the same point.

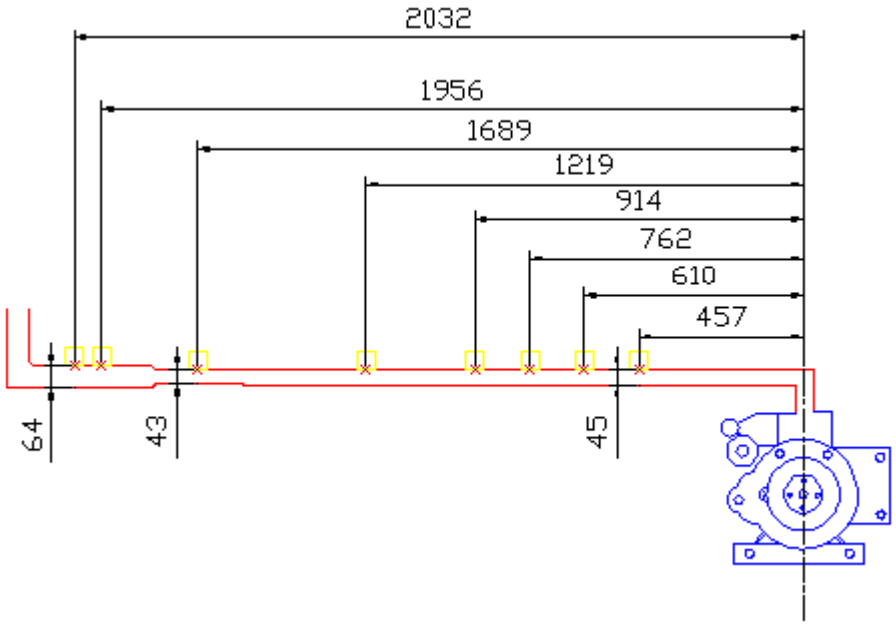


**Figure III-3 Exhaust pipe and sensor port configuration for the Yanmar single-cylinder engine showing pipe diameters and distance downstream to sensor ports in millimeters.**

In addition, a sample tube was installed approximately 1.8m downstream of the exhaust port to allow for exhaust gas sampling using the gravimetric method described later in this section.

### STEADY-STATE RIG

The steady-state rig, shown in Figure III-4, consisted of a flame section, seen below the table, a screen at the top of the combustion section, and a series of three PVC pipe section of decreasing diameter, each containing a sensor port. Each pipe section was surrounded with grounded conductive metal screens to eliminate radio interference with the sensor signal. A sampling tube could be placed in the top of the stack to measure the mass concentration of soot. The top of the stack vented to a fume hood.

To test the sensor in the soot of an acetylene flame, two tubes penetrated the wall of the combustion, one connected to a supply of acetylene and one connected to a supply

of compressed air. The acetylene flame was ignited by a push-button spark generator. Because the supply of acetylene was not premixed with air, the resulting diffusion flame produced soot in proportion with the acetylene flow rate, which was controlled by a rotameter. The overall soot concentration was varied by using a rotameter to control the flow rate of compressed air, which diluted and mixed the soot in the flame section. The screen at the top of the flame section both reduced the turbulence of the flow entering the pipe sections and removed large soot particles. Some of the soot particles produced in the acetylene flame were as much as 3 cm in their longest dimension.

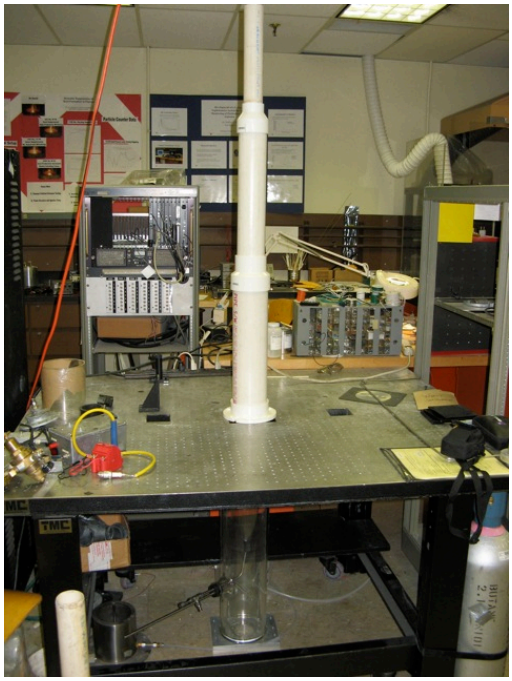

**Figure III-4 Steady-state rig with flame section at the bottom and three pipe sections of decreasing diameter.**

To produce diesel soot in the flame section of the steady-state rig, a wick-type lantern was filled with diesel fuel. After lighting the lantern, the wick height was adjusted to produce visible smoke. An aluminum-and-screen shroud protected the flame from the dilution air.

The PVC pipe sections had internal diameters of 4", 3", and 2", so at a given soot concentration, the flow in the smallest diameter was 4 time faster than the flow in the largest pipe section. The dilution air rotameter was calibrated over a range of 3-28 $ft^3$/min ($1x10^{-4}$ - $1x10^{-5}$ $m^3/s$). The flow of acetylene was at least two orders of magnitude lower by volume, so the gas velocity through the pipe sections was calculated based on the flow rate of dilution air. At the highest flow rate of dilution air (28 ft3/min), the gas velocity in the smallest pipe section was about 6.5 m/s. The lowest mean exhaust gas velocity in the Yanmar was around 4 m/s, so there was some overlap in the velocity range of the steady-state rig and the Yanmar, but the steady-state rig could not produce higher velocities.

### 6.7L CUMMINS DIESEL ENGINE

Much of the testing in the later part of the research program was conducted on a 6.7L displacement medium-heavy duty engine from the ISB-350 family of engines loaned by the Cummins Engine Company. The engine is shown in Figure III-5. Bore and stroke were 107mm and 124mm, respectively. The quantity and timing of fuel injection was precisely controlled through the use of a high-pressure common rail fuel injection system and electronically controlled piezo-electric fuel injectors.

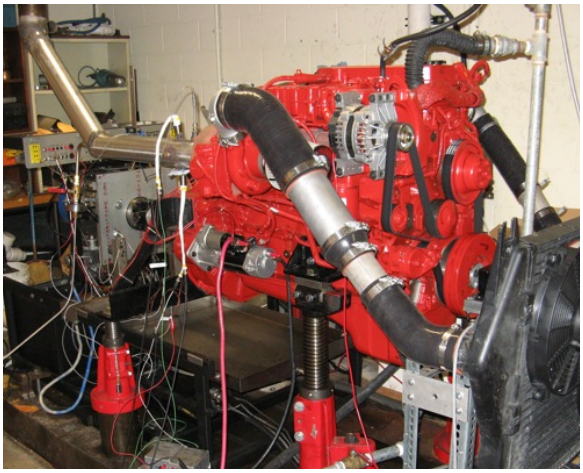

**Figure III-5 Cummins ISB-350 6.7L turbocharged diesel engine, prior to installation of DPF and bypass equipment.**

The engine was turbocharged by a variable geometry turbine (VGT) able to provide boost levels up to 1 atmosphere independent of engine speed and load. Charge air was cooled in an air-air heat exchanger, seen at the front of the engine, to increase the density of the intake charge. Emissions controls also included an exhaust gas recirculation (EGR) system with exhaust gas cooled by the engine coolant (at 90°C) and flow controlled by a valve (EGR valve). EGR fraction could vary from 0% to 40% depending on the operating conditions. Automatic control of the EGR rate could be over-ridden and set by the user, and this was typically done to ensure a fixed and repeatable EGR level. When the commanded EGR fraction was changed in user-override mode, the engine altered the position of the EGR valve and the boost pressure to provide the requested EGR fraction while holding the same overall charge mass flow (i.e. the mass of fresh air plus the mass of fuel plus the mass of recirculated exhaust gas remained constant.) Thus, when the EGR fraction was changed at constant power output, the combustion became more rich due to the lower $O_2$ content of the recirculated exhaust gas. The Cummins interface software allowed the logging at roughly ½ second intervals of various engine operational parameters, including load, speed, fueling rate, turbo speed and boost level, EGR fraction, and mass flow rate of charge air.

The engine had a maximum rated power output of 350 bhp at 2600 RPM. The maximum speed was 2800 RPM, and a maximum torque of 1020 Nm (750 ft-lbs) was ECU-limited. Brake mean effective pressure at peak torque was 1910 kPa. It was mated to a SuperFlow water-absorption dynamometer. The dynamometer had a maximum nominal power absorption of 1000 bhp, but the maximum torque was limited to 500 ft-lbs and was speed dependent, not developing full torque until 2200 RPM. Thus the maximum engine load in this study was limited by the dynamometer. At 700 RPM, the nominal idle speed, the maximum torque produced by the dynamometer was 48 ft-lbs, about 20% of maximum load, and at 2200 RPM, 500 ft-lbs represented just over 65% of the maximum load.

The engine was fitted with a combined DOC/DPF unit to enable full testing of the OBD function of the sensor. Plumbing was installed to allow part or all of the exhaust gas to flow around the DOC/DPF. In this way, a DPF failure could be simulated by allowing unfiltered exhaust to reach a sensor installed downstream of the DPF. Valves were installed at the DPF inlet and in the bypass to provide no-, partial-, or full-diversion of exhaust gas through the bypass. A photograph and schematic diagram of the DPF-bypass arrangement are shown in Figure III-6.

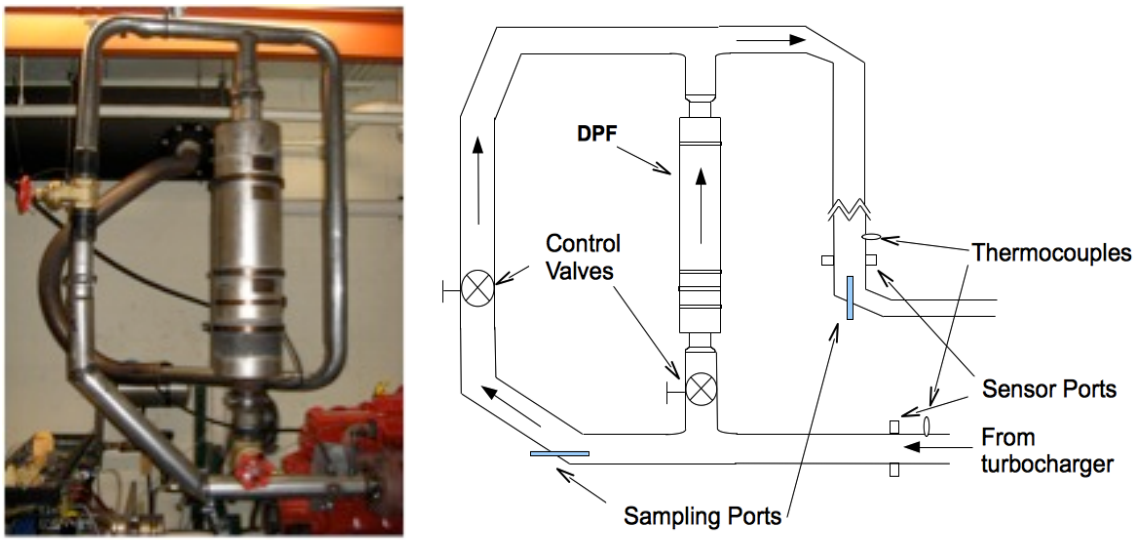


**Figure III-6 Arrangement of the diesel particulate filter and bypass loop.**

Pairs of threaded ports were installed in the exhaust pipe at positions upstream and downstream of the DOC/DPF so that sensors could be installed at either location. The upstream ports were located 0.15m downstream of the turbo outlet. The downstream ports were located 4.7m downstream of the turbo outlet, as measured along the exhaust pipe centerline through the bypass loop. Immediately upstream of each pair of sensor ports, a thermocouple was installed to measure the exhaust gas temperature. Combined with the mass-air flow rate provided by the ECU, this allowed calculation of exhaust gas velocity. The arrangement of the sensor and thermocouple ports with two sensors

installed at the upstream location is shown relative to the turbocharger outlet in Figure III-7.

**Figure III-7 Position of the sensors and thermocouple relative to the turbocharger exhaust outlet.**

Recording of sensor data on the Cummins engine was carried out by a separate DAQ system controlled by a National Instruments LabView™ interface. For most of the steady state work, a sampling rate of 20 samples/s was used. A software algorithm was used after testing was completed, to line up the data for correlation of the sensor data with ECU-logged data.

### GRAVIMETRIC FILTER SAMPLING

To develop a calibration curve for the sensors, it was necessary to make a direct measurement of the soot mass concentration of the exhaust. Our method for doing this was to sample the exhaust flow by drawing it through a sample tube and a glass fiber filter by means of a vacuum pump. The volumetric throughput was measured using a bellows-type meter of the kind typically used for metering natural gas.

Exhaust gases were sampled at three places for gravimetric analysis: in the exhaust pipe of the Yanmar engine, and upstream and downstream of the DPF in the

exhaust pipe of the Cummins engine. For each of these sampling locations, a ½"OD (0.42" ID) stainless steel or copper sample tube was arranged so that the tube opening was parallel to the direction of exhaust gas flow and facing upstream. The sampling tube passed through an airtight fitting in the exhaust pipe wall and led to a ball valve by which sampling flow could be started or stopped. Immediately downstream of the ball valve was a holder for a 2-inch borosilicate glass-fiber paper filter (Specialty Products, Inc, Model No. 200B70). The filtered exhaust gas then passed through a 1.5m length of stainless steel 3/8"OD tubing to a bellows-type gas flow meter and then through a 0.5 m length of 3/8" OD Tygon tubing to a vacuum pump. The vacuum pump used with the Yanmar test rig was a KNF Neuberger Model UN026 ANP diaphragm vacuum pump with a free-flow capacity of 1.6 $ft^3$/min. The vacuum pump used with the Cummins test rig was an Emerson Model C55JxJFY-4450 diaphragm vacuum pump with a free-flow velocity of 2 $ft^3$/min. The gas flow meter was a Rockwell International Model R-275 with a maximum capacity of 4.6 $ft^3$/min. The order of the vacuum pump and flow meter was not important and varied based on the convenience of the setup.

In the earlier testing on the Yanmar engine, an effort was made to ensure that the entrance velocity at the opening of the sampling tube matched the free-stream velocity in the exhaust pipe. However, later calculations determined that the aerodynamic forces on the soot particles dominated the inertial forces and that sampling error due to kinetic sorting was not expected to be significant. In practice, too, the sampling rate was limited by the pressure drop across the filter, which would increase throughout a sampling run due to the accumulation of particles in the filter pores. Actual control of the flow velocity at the sample tube inlet was impractical, both in light of the range of the mean exhaust gas velocities (from 2 m/s to 50 m/s) and the pulsating nature of the flow velocity.

Prior to making a gravimetric filter measurement, the filters were marked with water-proof ink and heated for at least 15min on a hot plate set at 100°C to desorb water from the ambient air and then immediately weighed on a fine force balance. As soon as 15s after removal from the hot plate, the mass of the filter could be observed to increase,

due to water adsorption from the ambient air so care was taken to measure the filters while still hot. At least three measurements of the dry, hot mass of the filter were recorded and averaged. The mean value for the clean, empty filters was 0.73g, and the measurement uncertainty for the dry empty measurements was 0.004g or about 0.55% of the measured value. Between the initial weighing and installation in the filter holder, the filter was kept in a covered box and handled only with tweezers to prevent accumulation of dust from the air and addition or deletion of material from handling.

After sampling, the filter was removed from the filter holder and placed on the hot plate held at 100°C to drive off water and the volatile fraction from the collected soot. The filter was kept on the hot plate for at least an hour but more commonly overnight (12 or more hours) to allow thorough evaporation of the volatiles. In one qualitative experiment, a petri-dish lid was kept covering the filter while on the hot plate. In the morning, a substantial oily residue was found on the inside of the cover. By weighing the filter before and after heating, it was found that for filter samples taken from exhaust from the Yanmar, the volatile fraction accounted for 25-85% of the total captured mass, depending on the operating conditions of the engine during the sample. For filter samples taken from Cummins engine exhaust, 25-35% of the total captured mass evaporated during heating.

The difference in the mass of the filter before and after the measurement and subsequent heating was taken as the mass of the non-volatile PM, which was further assumed to be the carbonaceous fraction. Whereas the typical laboratory filter measurement involved a dilution of the exhaust gas before sampling, our method did not. Because the sensor worked with undiluted exhaust, it was deemed more appropriate to sample the exhaust gas directly without dilution. The primary effect of air dilution is to encourage agglomeration of particles and to precipitate gases which form the non-carbonaceous and soluble fractions of the PM. Hence, the absence of dilution in our measurements was not considered to impact the correlation of sensor output to carbonaceous soot content.

Typically, between 15 and 30 cubic feet (0.4-0.85 $m^3$) of exhaust gas were sampled, as measured at the bellows meter, where the gas had cooled close to room temperature. The total sampled, dry mass was divided by the volume of gas sampled to determine the mass concentration of the exhaust gas. The relevant volume of exhaust gas is the volume at ambient air temperature since it is the ambient air concentration of PM that is of concern. Mass concentrations calculated for the conditions inside the exhaust pipe for a typical exhaust gas temperature of 300°C would yield a lower concentration due to the lower density of the hot exhaust gas.

During a filter sampling run, one or more sensors were typically installed in the sensor ports and their signals recorded for the duration of the run. Thus, a mean value could be calculated and correlated to a known mass concentration of PM in the exhaust. For a measurement like this, the record of the data began after the engine was warmed up and at steady state (as determined by the stability of the sensor signal and exhaust gas temperature). Data acquisition was begun immediately prior to opening the sampling valve to start the flow of exhaust sampling through the filter. After the sampling valve was closed, the engine speed and load were reduced, and then the engine was shut down. After the sensor signal came to steady state, data acquisition continued for about 10 seconds and then was stopped. The steady-state mean value of the signal from the sensor after shutdown was then calculated and subtracted from the rest of the signal to properly account for any offset in the electronics hardware. A mean and standard deviation were then calculated for the portion of the signal associated with the filter sampling. An example of such a sensor signal during a sample measurement is given in Figure III-8.

In this example measurement, the output from the sensors was filtered through electronic-low pass filters with a critical frequency of 23 Hz. The mean values and standard deviations were calculated from the signal from t=0s to t=375s. The reduction in engine speed and load occurred at t=390s, and engine shutdown occurred at t=405s. The steady state offset value was calculated over the interval [415s,425s]. The calculated PM dry mass concentration was about 4 $mg/m^3$. The two sensors had different electrode

spacing and shroud hole size and therefore had different sensitivity. They were located in ports 15 cm downstream of the turbocharger exit in the Cummins engine.

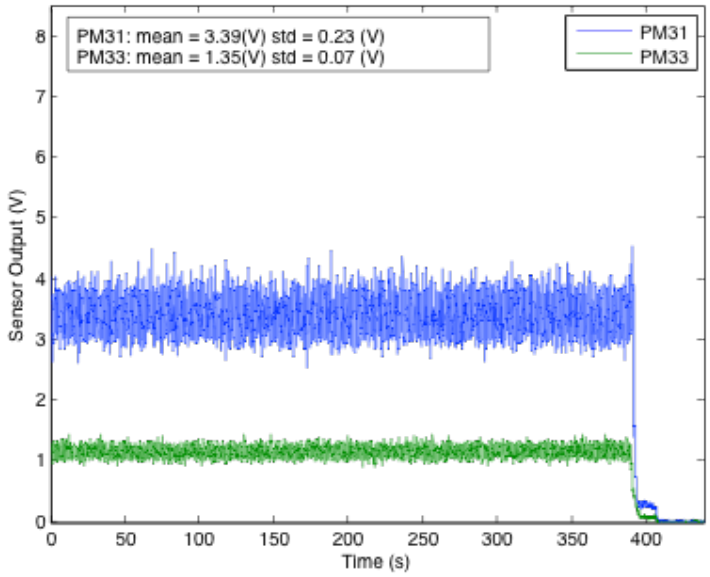


**Figure III-8 Sensor signals during a gravimetric filter measurement on the Cummins engine**

The efficiency of the filters varied with particle size. Measurements at the same engine condition taken at the upstream sampling port were consistently lower than those taken at the downstream port. Because the dilution level in the exhaust pipe was low, I did not expect there to be significant formation of new nucleation mode particles until the exhaust plume reached the ambient air. Accumulation-mode particles, however, can agglomerate during passage down the exhaust pipe, thus shifting the particle size distribution to a larger mean value at the downstream sampling location. Higher filter efficiency explains the greater mass captured on the downstream filters and, as will be seen, the lower sensor sensitivity for sensors installed at the downstream location was also a result of particle agglomeration. A similar effect was seen by the shift in particle size distribution due to changes in EGR fraction.

Using the gravimetric method, an emissions map was made for the Yanmar engine. The mass concentration of PM in the exhaust was found to be a strong function of torque and not very sensitive to engine speed. The measurements presented in Figure III-9 Soot emissions map for the Yanmar single-cylinder engine. were made over the full range of torque of the engine and at speeds ranging from 1200 to 2000 RPM. The mass concentration of soot was in the range 3-2500 mg/m$^3$, and the power-normalized soot concentration fell into the range 9-400 mg/bhp-hr. Recall that the maximum allowable output according to federal regulations was 15 mg/bhp-hr.

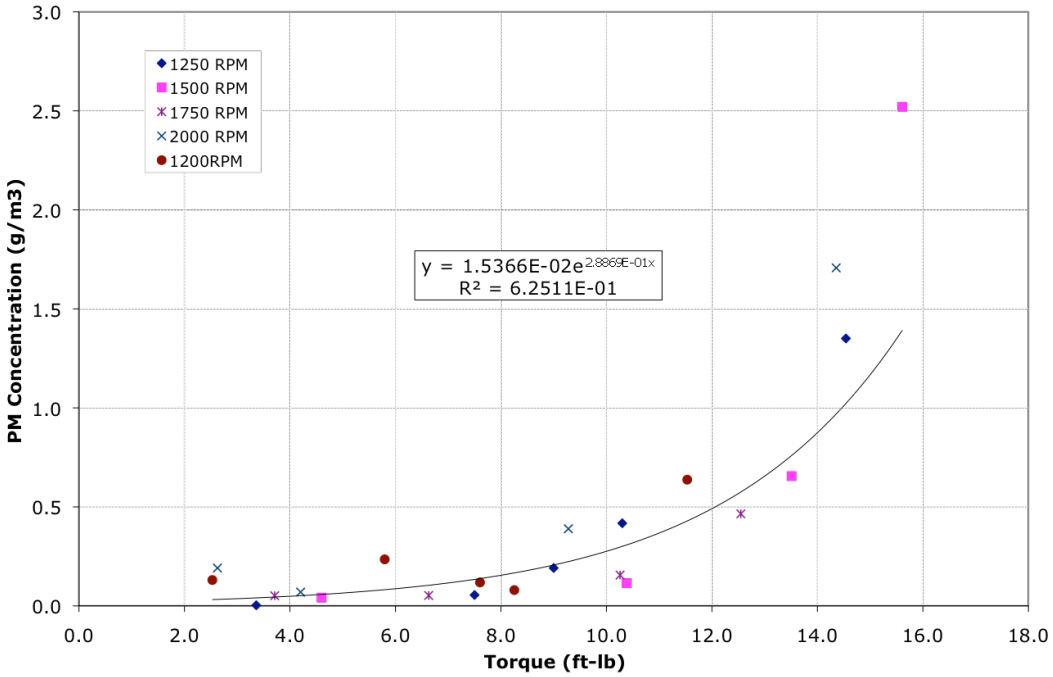


**Figure III-9 Soot emissions map for the Yanmar single-cylinder engine.**

# Chapter IV: Body of Work

## SENSOR BEHAVIOR

Testing of the sensor under different operating conditions revealed the physical mechanisms responsible for the sensor's operation. In the following sections, several modes of operation of the sensor will be presented along with a discussion of what each mode revealed about the sensor mechanism. The discussion proceeds from the general to the specific, in an order that sheds increasing light on the mechanisms.

### Resting State

The first, most basic response of the sensor observed was its resting state. In the absence of any particles in the electrode gap, the steady state current on the sensing electrode was very close to zero. Careful measurements were made of the steady-state voltage output of the sensor and electronics. The difference in output from the sensor with the field electrode energized at 1.9 kVDC and not energized was about 1.1mV, which corresponded to a current on the sensor electrode of $2.1 \times 10^{-12}$ A. This resting state current went to within a picoamp of zero when the electrically isolated electrodes were used for the same measurement, so any steady-state current was due to the finite conductivity of contaminants on the surfaces of the electrode ceramics. Typical signals during operation ranged from 0-8V, corresponding to electrode currents of up to $15 \times 10^{-9}$ A, thus the steady-state gap current was fully 4 orders of magnitude smaller than the maximum current. This was strong evidence that there was not a steady-state plasma discharge in the electrode gap.

### Conductive Powders

When conductive but electrically neutral particles were blown into the gap with the field electrode energized, the sensor produced a signal. In the figure below, the response of an energized sensor was plotted for two cases. For the response plotted on the upper axis, a bulb syringe full of activated carbon powder was puffed over the sensor

electrode three times. For the data on the lower set of axes a similar series of puffs was performed from a plastic bottle of graphite powder of the type used for lubricating locks. The electronics for these measurements were set to amplify the signal such that the full scale output corresponded to a current of 15 nA at the sensing electrode. Neither the concentration nor the duration of the puffs were controlled in these measurements, so no specific information is available about the mass or number density of the puffs. Yet some conclusions may be drawn: the current was unipolar with the same sense as the field electrode, and the signal was similar in magnitude to that seen for diesel exhaust. By integrating the signals, I found that in each puff, a total charge transfer on the order of $1.5 \times 10^{-9}$C occurred, equivalent to the transfer of about $1 \times 10^{10}$ elementary charges.

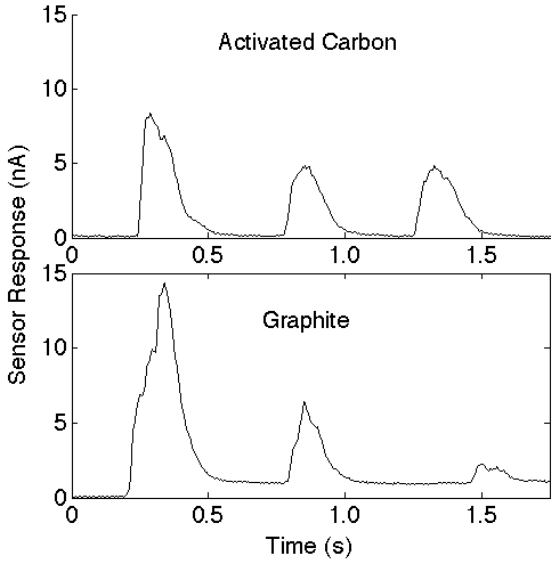


**Figure IV-1 Response of the sensor to electrically neutral conductive powders**

When the polarity of the field electrode voltage was reversed, the polarity of the signal also reversed. That is, with -1000VDC, the signals produced by activated carbon powder were qualitatively similar, yet with the opposite sign.

**Tip-In (Transient) Events**

The sensor was placed in the exhaust of the single-cylinder engine during transient events known as tip-ins, where the fueling rate was rapidly increased and then returned to the initial state. This caused the engine to speed up temporarily and typically resulted in a substantial increase in PM emissions.

During the course of the measurements, it was thought that the muffler attached to the exhaust port of the engine was interfering with high time-resolution measurements of the response of the engine to transient events. In particular, the effect of the muffler on measurements of the natural charge was unknown. Thus, a new exhaust pipe header was fabricated that did not include the original muffler. Analysis of transient events reported in this thesis was done with the muffler-less exhaust system in place.

During a tip-in on the single-cylinder engine, the sensor produced a signal even when the field electrode was not energized. In this mode, it behaved as an ion probe and responded to the naturally charged particles which came into contact with the sensor electrode. An example of this function is given in the Figure IV-2, where the output is shown from two sensors measuring the same tip-in event at the same downstream location in the exhaust pipe, one with the field electrode energized, the other with the field electrode off. In this figure, sensor output was shown in the more usual units of signal voltage. Recall that the conversion factor was 1.875 nA/V, so the full scale reading of 8V corresponded to a sensing electrode current of $15 \times 10^{-9}$ A.

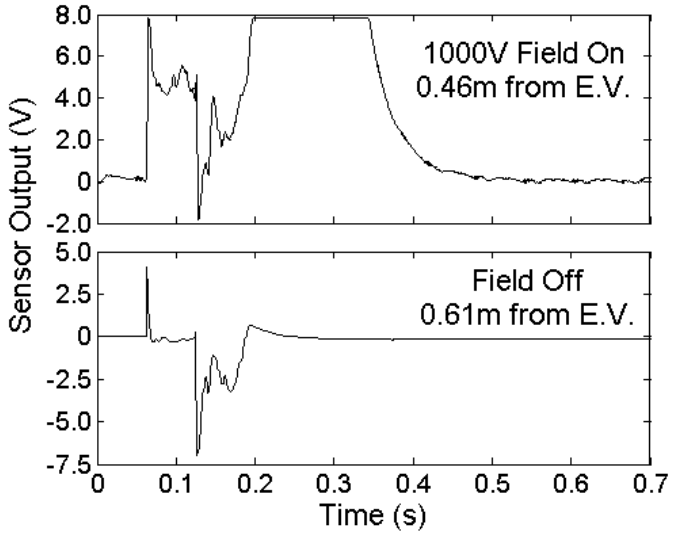


**Figure IV-2 Operation of two sensors in the exhaust of the single-cylinder engine, one with the field electrode energized, and the other with no electric field**

These plots show a very rapid tip-in, where the fueling portion lasted for a few revolutions only. Two distinct phases are evident. In the initial part ($0.06s < t < 0.18s$), called the "puff" the fueling rate is high, and the high in-cylinder pressures cause a vigorous blow-down each time the exhaust valve opens. This is the part of the tip-in which is detected by the sensor whose electric field is off. The second part of the sensor response is called the "hump" and is clearly seen in the upper plot ($t > 0.18s$). The current received by the sensor electrode is so high that the signal from the sensor saturates the amplification circuitry. This part of the tip-in is not shown by the sensor whose electric field is not energized. Thus, some of the soot is detected due to the charge that it carries from the combustion process and some of the soot is detected only in the presence of the sensor's electric field. Two modes of operation of the sensor have been demonstrated: detection of soot particles charged in the combustion process (i.e. *naturally charged* particles), and detection of neutral particles charged at the sensor (i.e. *locally charged* particles).

In addition, I set up a system to measure the time-resolved exhaust gas opacity while simultaneously measuring the PM sensor signal. A PM sensor was installed 0.5m

downstream of the exhaust valve. 0.76 (m) downstream of the PM sensor two mating sections of the exhaust pipe were separated and a short section of quartz tubing was inserted between them. A red diode laser was oriented to shine across a diameter of the quartz tube onto a photodiode detector (ThorLabs Model DET 110). The sensor and opacity signals from two sequential tip-in events are shown in Figure IV-3. The initial operating condition was 1500 RPM and idle-torque.

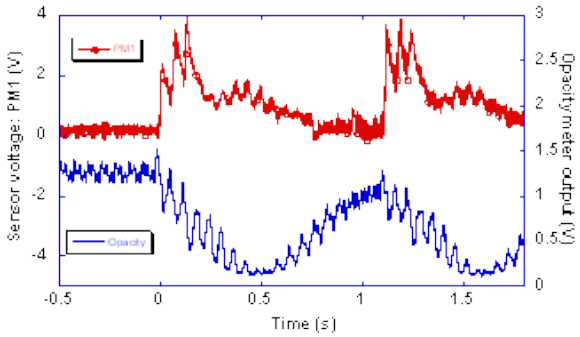


**Figure IV-3 Response of a PM sensor and an opacity meter to a series of two tip-in events in the Yanmar engine. Opacity meter was 0.76m downstream of the PM sensor.**

The opacity signal decreases as the light intensity reaching the detector drops due to attenuation by soot particles in the optical path, thus a lower signal level indicates greater lighter absorption and thus great soot concentration. It is important to note that the opacity signal begins to fall at the same moment the PM sensor signal begins its rise at the beginning of the tip-in. This demonstrates that the puff in the PM sensor signal was indeed a reaction to the presence of particulate matter.

Note that the pulsations in the opacity signal in the first part of the tip-ins had a larger amplitude than during the rest of the event, similar to the PM sensor response in the puff phase. However, the opacity does not show the same mean-value increase in attenuation that is visible in the PM sensor signal. The hump phase of the tip-ins is similar for both the opacity measurement. Because the opacity signal is insensitive to

both velocity and electrical charge effects, it is a good indicator of the overall soot concentration. Thus I concluded that the sensor is more sensitive during the puff phase than during the puff phase. This is due to the presence of naturally charged PM and the increased velocity of the exhaust gas, which supplies a greater time rate of charge to the sensor electrode.

In the puff phase of the tip-in, the high PM concentration flow reached the sensor and the opacity meter with very little time lag, on the order of 10 (ms). This is approximately the duration of the exhaust blow-down event: at an engine speed of 1500 (RPM) the duration of the exhaust stroke from BDC to TDC is 20 (ms). Based on the distance between the two locations, this corresponds to a mean velocity of around 10 m/s. Time-lag measurements made of corresponding amplitude peaks during the hump phase were about 70-80 ms, and thus the mean velocity was about 3.4 m/s, which closely matched the expected bulk flow velocity for the exhaust gas based on engine speed, displacement, and volumetric efficiency.

I explored this effect further by comparing the signals from two similar PM sensors installed at different locations in the exhaust pipe and recording their response to tip-in events. The data in Figure IV-4 is for two sensors installed 90 cm and 195 cm downstream of the exhaust valve in the Yanmar engine.

The dashed blue curve shows the response from the sensor closer to the exhaust valve, and the solid line represents the downstream sensor. In both response curves, the initial puff and later hump phases are visible. In the downstream sensor curve, the puff and hump are more spread out than in the upstream sensor. For this tip-in, the initial responses to the puff for each sensor are separated by 6.8 ms, indicating a speed of travel of 154 m/s. The hump travels much more slowly, with 323 ms separating arrival of the mass centroid of the hump at the two sensors, indicating a speed of travel of about 3.3 m/s, which is close to the bulk flow velocity of the exhaust gas.

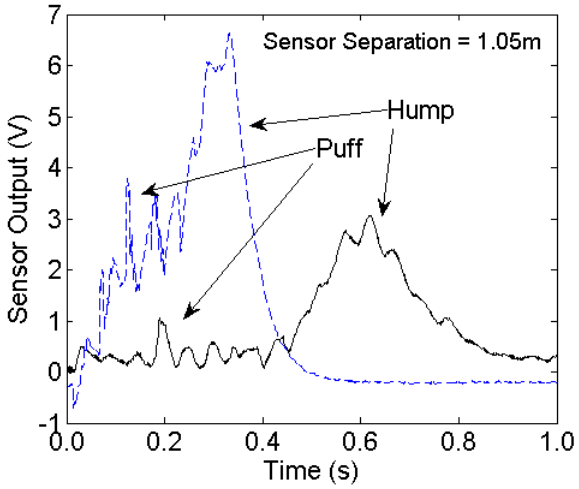


**Figure IV-4 Tip-in response from two sensors placed showing time lags for puff and hump phases. Dashed blue curve represents the upstream sensor, 0.9m from the exhaust valve. Solid black curve shows sensor 1.05m further downstream.**

I made a series of such measurements with the engine running at a range of speeds from 1500-2900RPM. In Figure IV-5 below, I plot the travel speed of the puffs (a) and the humps (b) over the engine speeds tested.

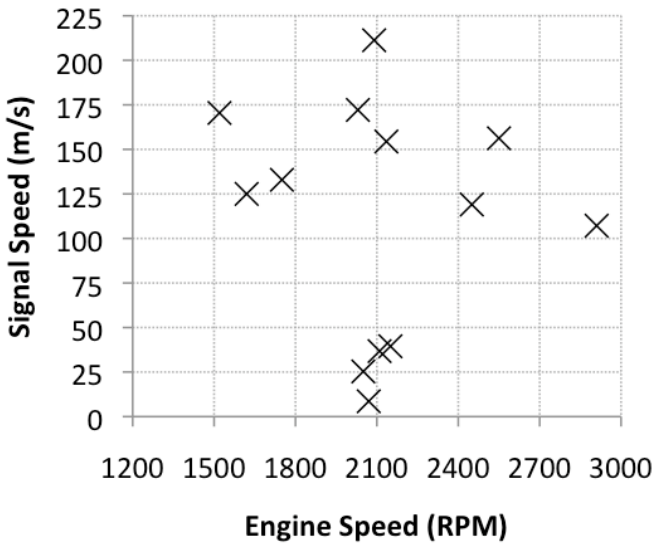


(a)

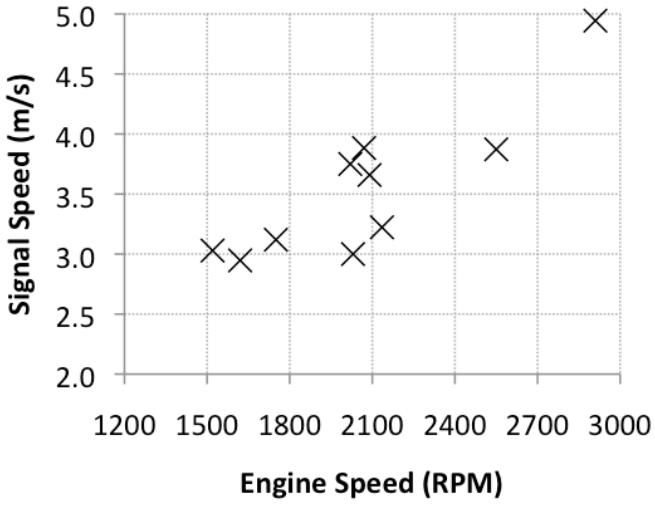


(b)

**Figure IV-5 Speeds of puff (a) and hump (b) portions of tip-ins in the Yanmar exhaust pipe, based on arrival time lag between two spatially separated sensors.**

The speeds of the puffs were largely independent of the speed of the engine, being driven by the blow-down event of the exhaust stroke. Variation in the speed of the puff was due to the intensity and duration of the tip-in event. This is illustrated by the range of calculated speeds at 2100 RPM, where the maximum fueling rate was varied by means of a limit-set-screw on the Yanmar fueling level. Lower speeds correspond to lower maximum fueling rates. The speeds of the humps increased with engine speed and matched the expected bulk flow velocity of the exhaust gas.

Response to a tip-in in the Cummins showed no presence of naturally charged particles. That is, there were no distinct puff and hump phases, and no signal was produced when a sensor was installed without the field electrode energized. In order to produce a signal in the exhaust of the Cummins engine, it was necessary for the field electrode to be energized. It was not clear why this was the case. Possible explanations include the loss of natural charge due to the mixing of gases from multiple cylinders in

the exhaust header of the Cummins or the close contact with the grounded conductive turbine blades in the turbocharger.

### Steady State Operation in Diesel Exhaust

The sensor produced a signal when the field electrode was energized and the sensor was placed in the flow of exhaust from a diesel engine. [39,43,44,45]. An example of this operation is shown in the figure below where two sensor recorded the steady-state operation of the Cummins engine during a gravimetric filter measurement. The sensors, PM25 and PM21 were of slightly different design and placed in the pair of ports closest to the turbocharger exit. The engine was run at 1800 RPM and 100ft-lbs until t=800s, when the speed was reduced to 700RPM and then the engine was switched off. The outputs from the two sensors were filtered to reduce noise with the 23Hz low-pass filters.

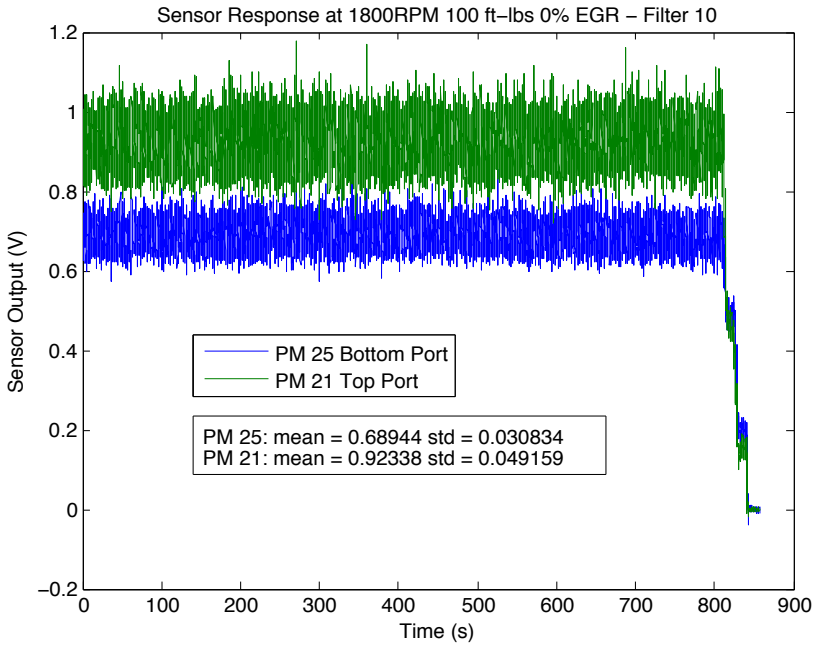


**Figure IV-6 Sensor response during a steady-state gravimetric filter measurement.**

The signals were observed under nominally steady-state operating conditions. The presence of two sensors co-located in the flow was useful for determining whether the variation was due to noise in the sensor signal or to real changes in PM emissions due to unsteadiness in the output of the engine. This was particularly the case in the Yanmar engine where sometimes large changes were observed. In Figure IV-7, the output of two sensors recording the same exhaust events is plotted. Four measurement runs are plotted on each axis, with the output of one sensor on the left axis and the output from the other on the right. Speed was constant at 2000 RPM for each run. Torque levels are noted on the plots. Under the 12 Nm condition, considerable noise was evident, but the close correlation of the output of the two sensors shows that this was due to an instability in the engine output rather than noise inherent to the sensors. Note for example that the spikes in output near t= 10s and t=50s had the same features. In the Yanmar, much of this variation was due to the simplicity and instability of the torque control system, which was affected by small changes in water pressure.

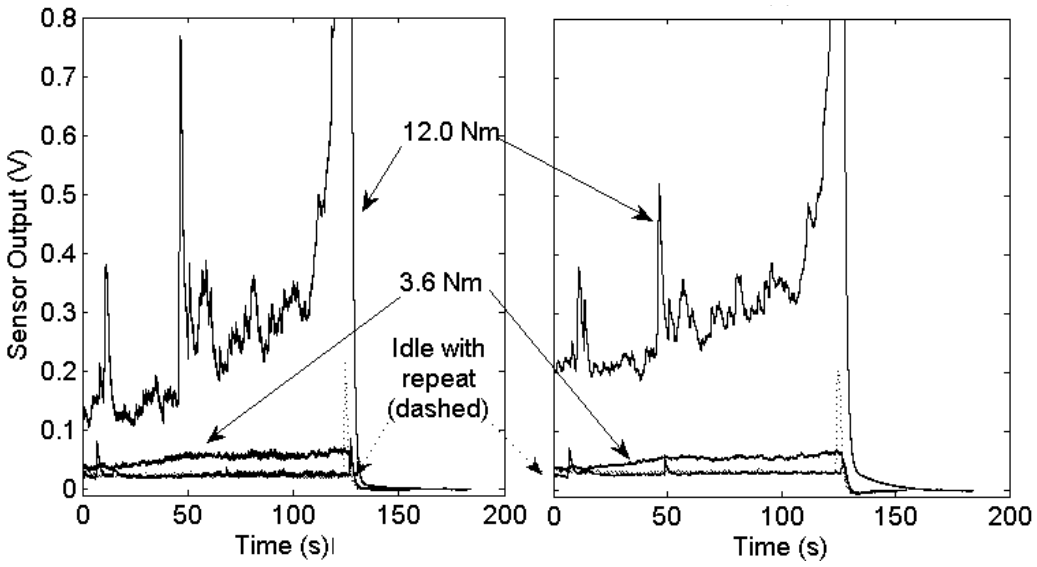


**Figure IV-7 Correlation of signals from two sensors in the same flow showing variability of engine soot output at nominal steady-state.**

Steady-state measurements of the sensors' outputs while recording the PM mass concentration with the gravimetric sampling system, allowed us to develop a calibration

curve for the sensor in the exhaust of the Yanmar engine running at two different engine speeds, shown in Figure IV-8. The calibrations were noisy due to the difficulty of holding the Yanmar engine at constant operating conditions for the time required to sample sufficient exhaust gas. Because of the nearly exponential increase of soot output with increasing torque, it was more difficult to sample at higher soot output conditions, so the measurements are more sparse at higher soot concentrations. Nevertheless, sensor sensitivities were calculated in the range of 0.2-0.6 (mV-$m^3$/mg), depending on the engine speed, with higher sensitivity at higher exhaust gas velocity.

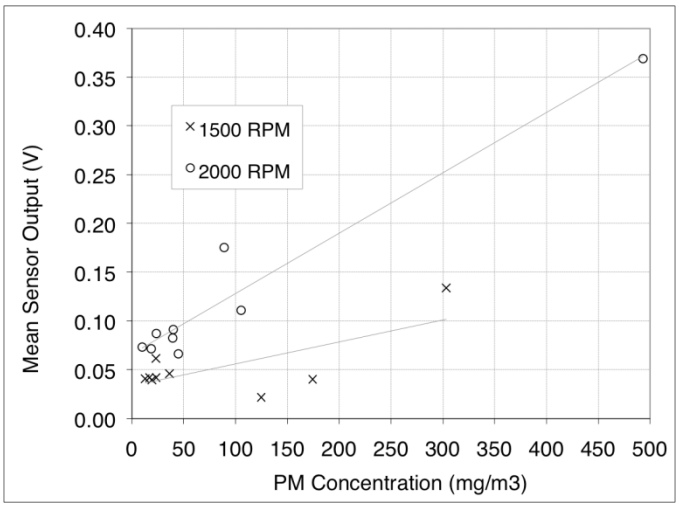


**Figure IV-8 Steady-state calibration of a sensor in Yanmar exhaust at two engine speeds.**

In the exhaust of the Cummins engine the sensors were found to be much more sensitive to the mass concentration of soot, but sensor sensitivity varied a surprisingly large amount for different operating conditions. The mass-based sensitivity varied, from 20 mV-m3/mg to as high as 1000 mV-m3/mg, or from 2 to 4 orders of magnitude higher than those seen in the single-cylinder engine. At low loads and speeds, the PM mass concentrations were the highest, from 20-30 mg/m3, but the sensitivity was at its lowest. At higher loads and speeds, the measured PM mass emissions were much lower, but the sensitivity of the sensor on a mass basis increased markedly. A series of measurements

from the Cummins running at 1800RPM and loads from idle to 50% is shown in Figure IV-9. The lowest mass concentrations were observed at the highest torque levels, where the highest sensitivity was also observed. The exhaust gas velocity for these measurements varied from 30 m/s at the low torque, high concentration, low-RPM condition to 50 m/s at the high torque, high-RPM condition. As will be shown later, the velocity of the exhaust gas in the Cummins did not have a strong effect on sensor sensitivity. Therefore, while the previously published correlation was valid in the exhaust of the Yanmar, in the exhaust of the Cummins engine, it did not follow the former trend.

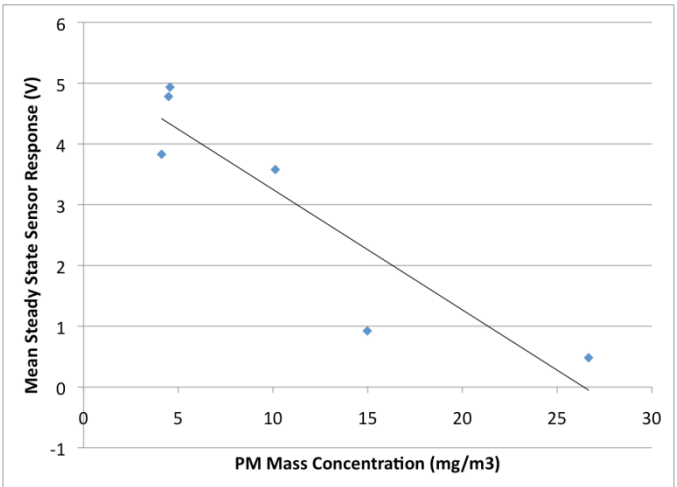


**Figure IV-9 Sensor calibration in exhaust from the Cummins engine at 1800 RPM.**

The reversal of the PM mass-sensitivity relative to the Yanmar calibration was believed to be an effect of the particle size and number densities. As will be shown later, the Cummins operating conditions significantly affected the shape and number distribution of the particles, with larger, more agglomeration particles being prevalent at lower speeds and torques, and smaller, less agglomerated particles at higher speeds and torques. This is believed to be a result of the higher fuel injection pressure, the turbocharger, and the advanced electronic engine controller on the Cummins engine. The sensor, therefore, was responding to the number and size of the particles rather than the total mass.

Several sensors were tested at steady state with corresponding filter measurements to assess the effect of various design parameters. Two types of sensor shrouds were used, a large-hole type, with holes of 4mm diameter and overall 38% coverage, and a small-hole type, with holes of 2mm diameter and overall 85% coverage. Two electrode gap sizes were used, one of 2mm and the other of 1mm. Two electrode configurations were tested: in one, the electrodes were similar, each of 3.2mm diameter; the other had an asymmetric design, with a sensing electrode diameter of 4.88mm and a field electrode diameter of 3.2mm. Two each of four sensor types were made, and tested in the Cummins engine at 1800 RPM and 300 ft-lbs torque. Because the sensors were all measured at identical operating conditions a mean soot concentration of 3 mg/m$^3$ calculated from all the runs was used for determining the sensitivities. The mean signal value for both sensors of the same type was averaged and divided by the soot concentration to produce the sensitivities listed in the table below.

**Table 1 Design parameters used to study sensor geometry.**

| Sensor Type | Shroud Type | Electrode Spacing | Electrode Type | Measured Sensitivity (V/m$^3$/mg) |
|---|---|---|---|---|
| 1 | 2 mm hole | 2 mm | Asymmetric | 0.66 |
| 2 | 4 mm hole | 1 mm | Asymmetric | 1.80 |
| 3 | 4 mm hole | 2 mm | Symmetric | 2.24 |
| 4 | 2 mm hole | 1 mm | Symmetric | 0.56 |

The sensor signal levels varied about +/-20% from sensor to sensor, most likely due to inadequate control of orientation, which was set by eye with the intent that the electrodes were perpendicular to the flow ($\theta$=90°, defined later in this chapter). The standard deviation of the soot concentration measurements was about 1 mg/m$^3$ due to the low soot mass being measured.

The parameter having the largest effect on sensitivity was the size of the shroud holes. The sensors with more open shrouds (types 2 & 3) had about 225% greater

sensitivity than those with the smaller-hole shrouds (types 1 & 4). The size of the sensing electrode did not have a large effect: the symmetric electrode sensors (types 3 & 4) were on average 10% more sensitive than the asymmetric ones (types 1 & 2), which was not a statistically significant difference. Finally, the sensors with the larger 2 mm gap (types 1 & 3) had a sensitivity about 25% greater than the sensors with a 1 mm gap (types 2 & 4). This increased sensitivity with a larger gap did not agree with the correlation previously published by Warey[43].

The effect of field voltage strength on sensitivity was studied with the Cummins engine, at 1800 RPM and 100 ft-lbs (135 Nm) of torque. The voltage on the field electrode was varied in 100V increments from 500V to 1900V. The steady-state mean sensor electrode current was calculated and plotted in Figure IV-10 below.

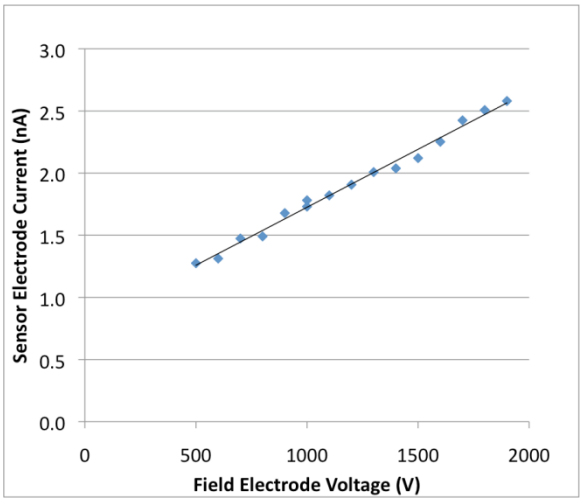


**Figure IV-10 Sensor electrode current as a function of voltage applied to the field electrode.**

The sensor output was linear with the applied voltage, but the intercept was non-zero. When the field electrode was grounded, the sensor signal was zero, thus the response was non-linear in the range of 0-500V. This voltage sensitivity was different from relationship reported by Warey, who found no offset, with the correlation curve passing through zero.

**Engine Thermal History Effects**

The sensor response to otherwise identical engine operating conditions was affected by the thermal history of the engine. That is, the signal in a warmed-up engine would typically be different than when the engine was still warming up. This effect was observed in both the Yanmar and the Cummins engines.

An example is shown in Figure IV-11, where a sensor was tested in the exhaust of the Yanmar on two different days with the same test protocol. First, a 120s 2000 RPM idle (no torque) period was recorded and then the engine was shut down. Then the engine was run at 2000 RPM and a moderate torque output of 3.4 Nm (about 10% load). The first day's data is shown in solid black and the second day repeat is shown in dotted lines. On both days, the change in signal with time had the same shape. Thus, the behavior was repeatable from day to day, and warm-up was critical for reproducible results in the Yanmar.

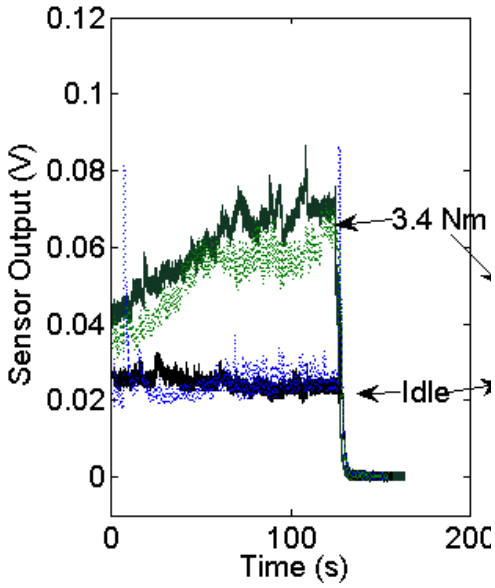


**Figure IV-11 Effect of engine thermal history on sensor output. First day run is in solid black; second day repeat in dotted lines.**

Similar results were seen in the Cummins engine during steady-state measurements, and thus it was evident that for repeatable measurements on either engine, the thermal state of the engine must be controlled. This effect was believed to be due to a change in the soot output of the engine as well as a thermal effect in the sensor. Higher in-cylinder temperatures favored the production of smaller soot particles of a higher overall number density. Thus, as the engine temperature rose during warm-up, the shift in size distribution of the particles caused an increase in sensor sensitivity, causing a rise in the sensor signal corresponding with a decrease in soot mass and an increase in number density. In addition, later modeling provided a physical basis for an increase in sensitivity with higher exhaust gas temperature.

**Effect of Sensor Orientation**

The orientation of a sensor installed in the exhaust pipe of the single-cylinder engine had little or no effect on the sensitivity of the sensor to exhaust PM. However, in the exhaust of the Cummins engine, sensor orientation had a substantial impact. The orientation of the sensor in the flow affected its sensitivity by altering the incoming flux of particles to the active region of the field electrode.

A two-dimensional end-on diagram of the sensor electrodes with respect to the exhaust gas flow is shown in Figure IV-12. The field electrode is labeled “F” and the sensor electrode is labeled “S.” The shroud is not shown. $\theta$ was defined as zero when the electrodes were aligned in the direction of the exhaust gas velocity and the field electrode was downstream.

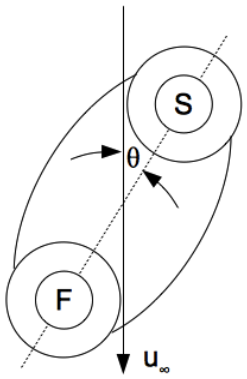


**Figure IV-12 Sensor orientation convention.**

The response of a sensor placed in an exhaust flow and slowly rotated is shown in Figure IV-13. The time series data is for a sensor slowly rotated through 540°. In this measurement, the sensor was in the upstream port, and the engine was operating at light (10%) load at 1800 RPM. The exhaust gas velocity was 30.9 m/s and the mass concentration of particles was 25 mg/m$^3$. The relevant orientation angles are noted.

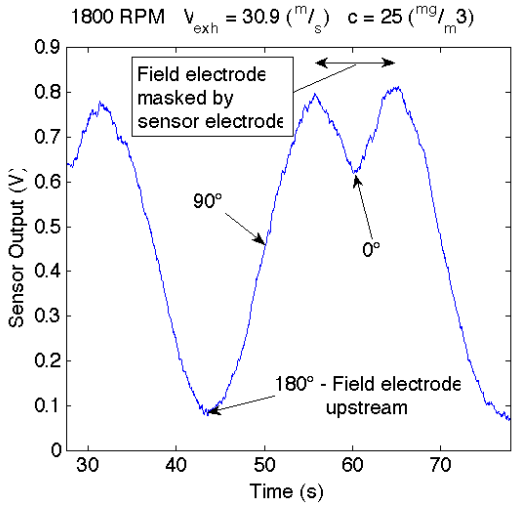


**Figure IV-13 Effect of orientation on sensor output.**

Note that at 0°, when the sensing electrode is upstream of the field electrode, the signal was lower than when the sensing electrode was offset to either side. The lowest signal was obtained with the sensor in the 180° orientation, that is, with the field

electrode upstream and the sensing electrode immediately downstream of it. When the voltage on the field electrode was inverted, that is, when -1000VDC is applied, the sensor gives the same response with the opposite polarity. It was the blocking of the field electrode that caused the dip in response at 0°. This showed that sensor signal depended on the relative positions of the field and sensing electrodes, regardless of the polarity.

The effect of orientation on a sensor with asymmetric electrodes is shown in Figure IV-14.

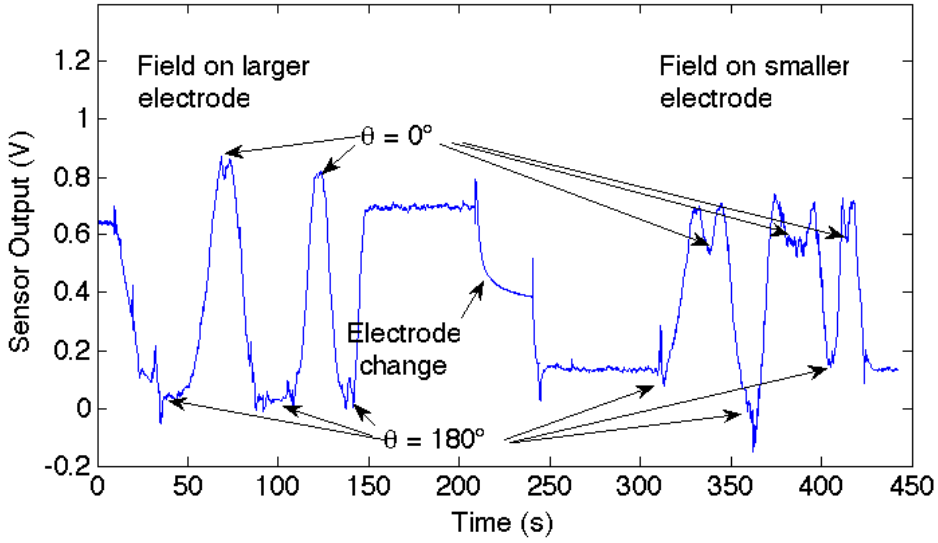


**Figure IV-14 Rotation of a sensor with asymmetric electrodes with electric field applied to first the larger and then the smaller electrode**

The sensor tested had an electrode gap of 1mm and electrodes of 3.2mm (1/8 in) and 4.8mm (3/16 in) diameter. The engine was operating at 1000RPM and producing 100ft-lbs of torque with a gas velocity of 13 m/s and a soot concentration of 23 mg/m$^3$. In the first part of the measurement, from t=0 to t=210s, 1000V was applied to the larger electrode, and the charge amp circuitry was connected to the smaller electrode. At t=0, the sensor was oriented at θ=15°. From t=10 to t=90s, the sensor was rotated through approximately 540°. From t=110 to t= 160, the sensor was rotated back to its original

orientation. The electrode leads were swapped in the interval from t=210 to t=250s, changing its orientation (defined by the positions of the sensor and field electrodes) by 180° to θ=-165°. The sensor was again rotated through approximately 540° in the period from t=310 to t=380s. After about a 10s pause, the sensor was rotated back to its original orientation.

In the first configuration, the effects of electrode masking were not evident as the sensor passed through θ=0° around t=70s and t=125s. In the second configuration, electrode masking was pronounced at θ=0°, at t=340s, during the pause at t=380s and at t=410s. In addition, the peak sensitivity was lower in the second configuration.

**Effect of Exhaust Gas Velocity**

Warey [43] made a series of sensor measurements with the Yanmar by installing a sensor in a series of three exhaust pipe sections with increasing diameter. Thus, he was able measure soot of the same mass concentration at different velocities without introducing complicating effects of changing engine conditions. He tested several sensors to develop velocity correlations. His measurements were made with the engine running at idle torque at three different speeds, 1250, 1500, and 2000RPM. Although no mass concentration measurements were made at the operating conditions, the mass concentration can reasonably be assumed to be constant. The data from one of his sensors is shown below in Figure IV-15. Using this method, he found the relationship of sensor output to exhaust gas velocity to be exponential with a mean exponential power of 0.62.

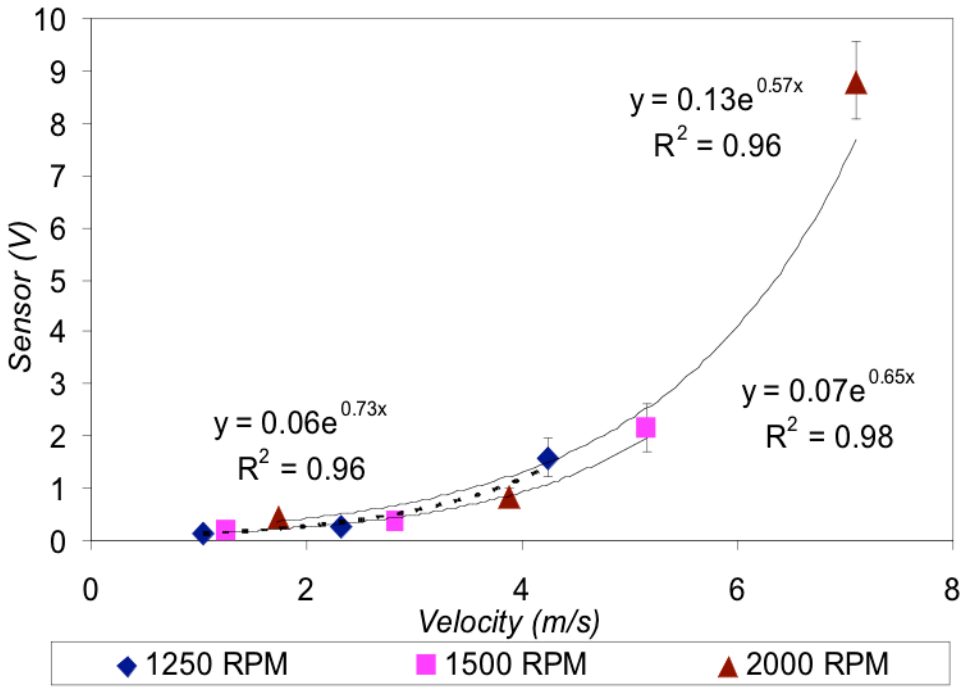


**Figure IV-15 Sensor response to exhaust gas velocity [43]**

In Figure IV-8, I showed the difference in sensitivity of the sensor in the Yanmar exhaust at two different velocities based on sensor output and measured soot concentrations in the exhaust. I also showed that the natural charge mechanism is significant in the Yanmar when the fueling rate is elevated, as during a tip-in event or when operating at higher speeds or torques. The increase in sensitivity with exhaust gas velocity in the Yanmar exhaust can be explained by considering that the exhaust gas carries a charge density (from naturally charged particles) and that the rate of impact at constant concentration would go up with increasing exhaust gas velocity. This is in line with the observed trend of sensitivity in the Yanmar exhaust.

In the Cummins exhaust, however, the natural charge density was not significant, so the charge flux to the sensing electrode must be locally generated, and it was not expected that the velocity sensitivity should behave in the same manner. The attempt at calibrating a sensor in the Cummins exhaust showed that different soot quality could lead

to different sensitivity. Therefore, to determine a sensitivity to exhaust gas velocity, it was necessary to try to ensure the same soot morphology but vary the exhaust gas velocity.

Through an exhaustive series of measurements of sensor output and mass concentration of exhaust in the Cummins engine, I determined that at least over a limited range of loads, the output of a sensor correlates well to the engine fueling rate expressed as injected mass per cylinder per cycle at constant EGR rate. In Figure IV-16, the steady state mean sensor output is plotted against fueling rate for a broad range of operating conditions and at various EGR rates at both the upstream and downstream locations. By carefully controlling the operating conditions to keep the fueling rate constant on a per cylinder per cycle basis, I tried to avoid any confounding effects due to major changes in soot morphology.

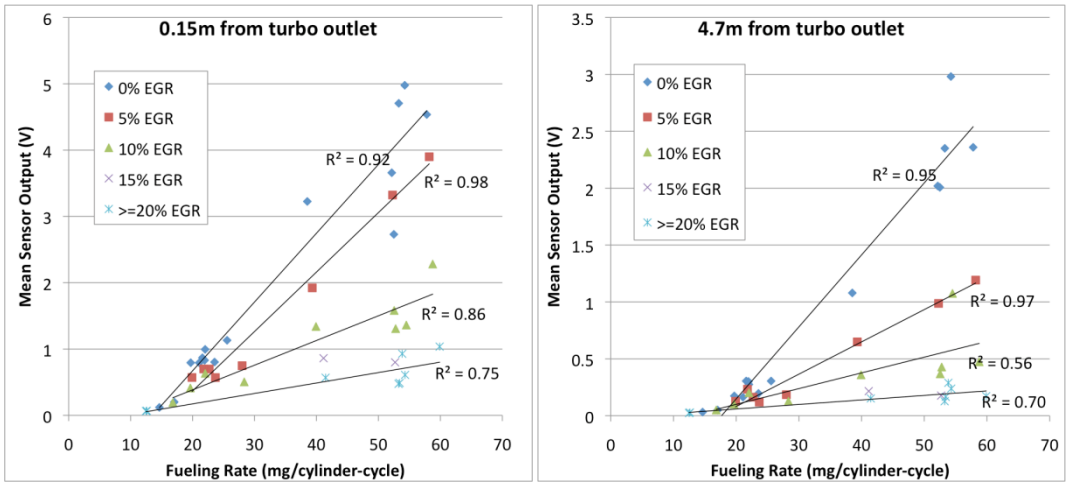


**Figure IV-16 Sensor response to fueling rate at various EGR levels, at upstream and downstream positions**

A series of operating conditions was designed that spanned a range of engine speeds from 1200 to 2200 RPM but kept the fueling rate constant at 19.8 mg/cylinder/cycle. The operating conditions are listed in Table 2 below along with some of the key characteristics of engine control and exhaust gas condition, including the mass of the inducted air charge as reported by the engine controller, the temperature of the

exhaust, the measured soot mass concentration and the mean values of the two sensors placed in the flow. The exhaust gas velocity was calculated by converting the charge mass flow rate into a volumetric flow by the ideal gas relation and dividing by the area of the exhaust pipe ($5.65 \times 10^{-3}$ $m^3$). The sensor whose output is labeled V1 was installed with orientation angle $\theta=45°$, and the sensor whose output is labeled V2 was installed at $\theta=90°$. For all cases, the EGR rate was set to 0% recirculation.

**Table 2 Operating conditions used in study of exhaust gas velocity effects.**

| Speed | Charge Flow | Vexh | Torque | Texh | Power | $C_{PM}$ | $V1_{mean}$ | $V2_{mean}$ |
|---|---|---|---|---|---|---|---|---|
| (RPM) | (kg/min) | (m/s) | Nm | (K) | (kW) | ($mg/m^3$) | (mV) | (mV) |
| 2200 | 10.60 | 41.5 | 81 | 469 | 19.9 | 31.5 | 963 | 668 |
| 1800 | 7.93 | 30.9 | 112 | 466 | 21.1 | 25.2 | 768 | 482 |
| 1500 | 6.21 | 23.6 | 134 | 455 | 21.1 | 22.6 | 675 | 455 |
| 1200 | 4.64 | 17.4 | 143 | 450 | 18.0 | 25.2 | 795 | 234 |

The sensitivities were calculated by dividing the mean sensor output by the measured mass concentration and are plotted in Figure IV-17. The optimally oriented sensor showed a higher sensitivity as expected and no significant change with velocity. The sensitivity of the sensor oriented perpendicular to the flow initially increased with velocity and then became constant at higher velocities. The reduced sensitivity of the perpendicular sensor at the engine condition for the lowest speed is thought to reflect a possible difference in the particle morphology, although the exact mechanism is not clear.

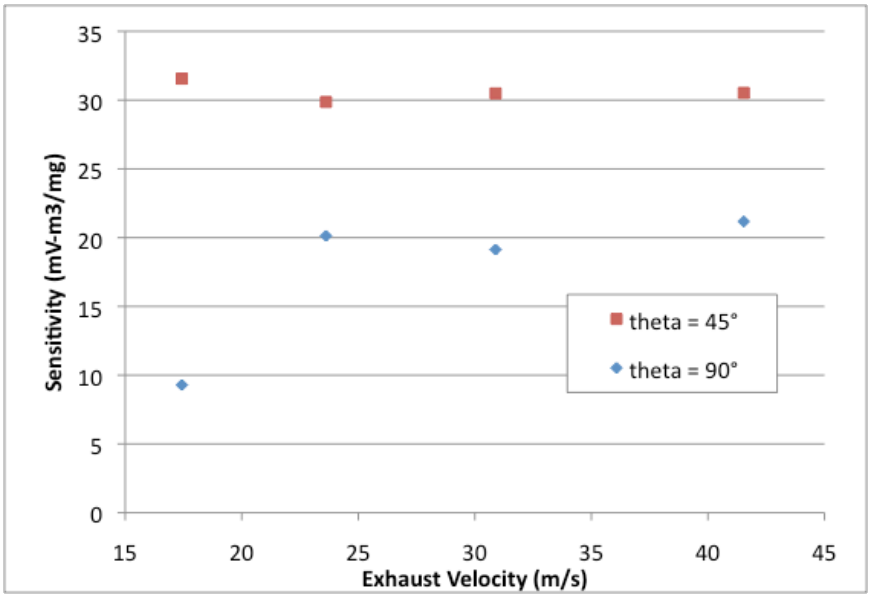


**Figure IV-17 Sensor sensitivity to exhaust gas velocity at two orientation angles θ.**

Thus in summary, in the natural-charge rich exhaust of the Yanmar engine, the sensor showed an increased sensitivity in faster-moving exhaust. In the Cummins engine, the particles did not carry a substantial natural charge. The sensitivity of the sensor in that exhaust did not show a significant sensitivity to the velocity of the exhaust gas.

### Effect of EGR Fraction

Varying the EGR fraction alters the concentration and quality of the soot in the exhaust. This effect was notably demonstrated by varying the rate of EGR at otherwise constant operating conditions.

PM measurements were made at constant speed and load with EGR fractions of 0%, 10%, and 20%. At each EGR level, the sensor was rotated in the flow, with the result shown in Figure IV-18 below.

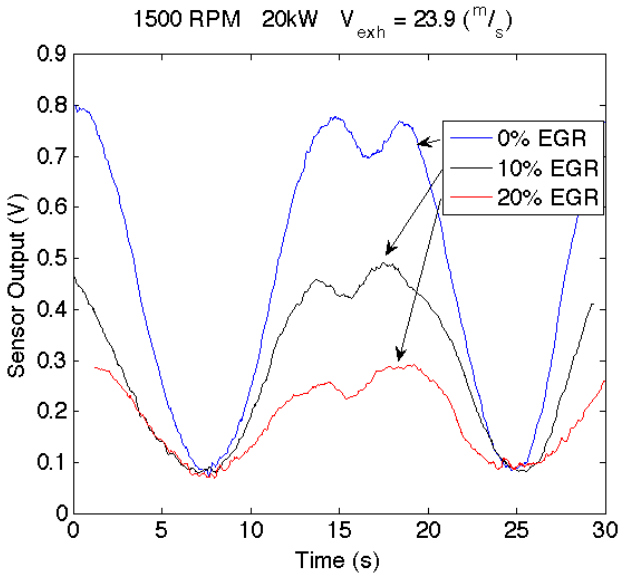


**Figure IV-18 Effect of EGR fraction on sensor signal.**

At each condition, the ECU adjusted the boost pressure to keep the total charge flow, fueling rate, and the power output at 20kW. The mass concentration of PM in the 0% EGR case was measured at 23 mg/m$^3$, and doubled to 45 mg/m$^3$ at 20% EGR. The amplitude of the signal, however, decreased by 60%. This was suspected to be a result of a change in the morphology of the soot particles, but no equipment was available in this study to establish size distributions and number density.

However, I was able to qualitatively assess the change in particle morphology by using a transmission electron microscope (TEM.) In a method similar to that used by Zhu and Lee [24,27] TEM sample grids were exposed to exhaust flow at the downstream sensor ports in the Cummins operating at 1800 RPM and 300 ft-lbs with 0% EGR and at 20% EGR. In the TEM images shown in Figure IV-19, wide angle (a) and (c) views show a collection of many particles to give a qualitative sense of the size distributions. Image (a) shows the soot particles gathered at 0% EGR, and (c) shows the soot particles gathered from the 20% EGR flow. Images (b) and (d) show individual particles from the wide field views at the maximum TEM magnification.

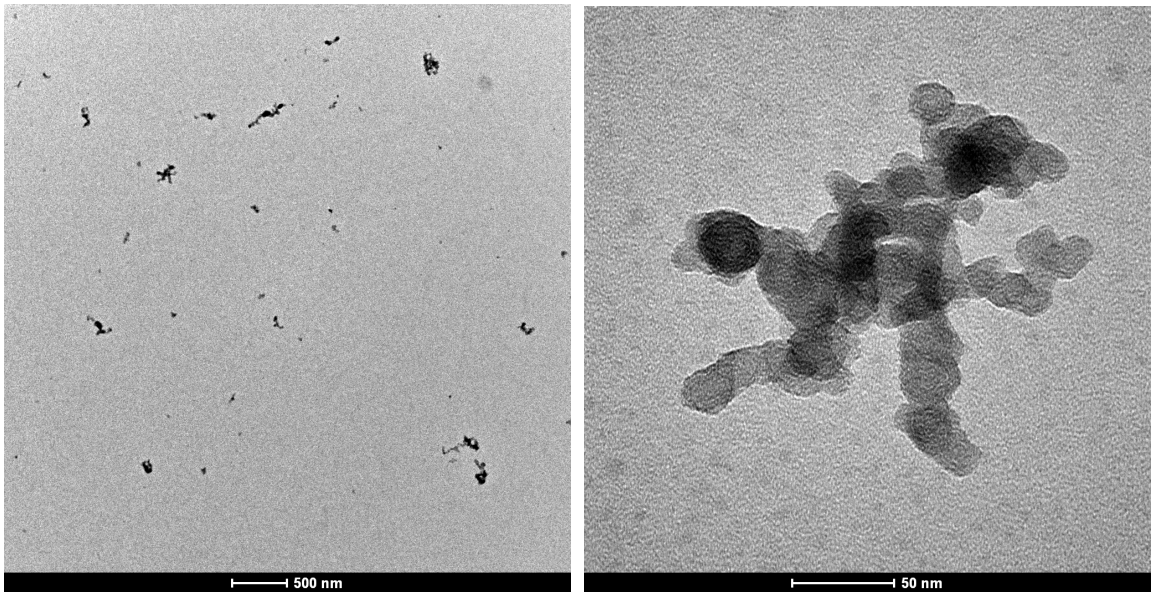


(a) (b)

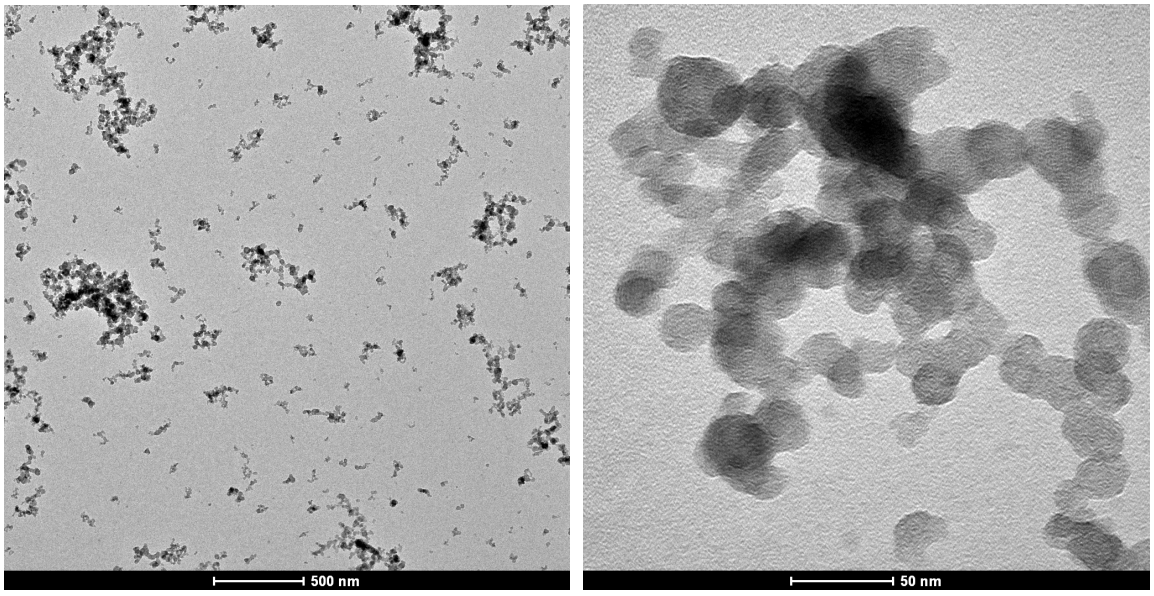


(c) (d)

**Figure IV-19 TEM images of soot particles obtained in exhaust from downstream sensor port of the Cummins engine at 1800 RPM and 300 ft-lbs torque with EGR levels of 0% in (a) and (b) and 20% in (c) and (d).**

While the duration and method of exposure of the TEM sample grids was similar for both EGR levels, one cannot draw conclusions about the overall number densities of the exhaust flows because the capture efficiency of our sampling method is not known. In addition, I did not use the thermophoretic method of Zhu and Lee at Argonne, but even in their work, they did not claim to provide number density information. I suspect that the smallest particles, including individual primary particles, were not captured as efficiently as were the largest particles.

However, it is evident from these images that the mean size of the agglomerated particles is substantially larger in the 20% EGR flow. Agglomerated particle size in the 0% EGR flow seems to be around 100 nm on average and be less branched than in the 20% EGR sample, where the particles show much more branching and tend to have larger dimensions, ranging as high as 1 $\mu$m across the longest point. Without a comprehensive image analysis, it is not clear whether the size of the primary particles is different on average between the two EGR levels, although the work of Zhu and Lee suggests that the particles in the 20% EGR case should have been 30-50% larger on average than in the 0% case.

The higher sensitivity of the sensor at lower EGR levels suggests that smaller particles are more effective in causing charge flux to the sensor electrode. This could probably be closely correlated to the electrical mobility of the particles.

**Effect of Position in Exhaust Pipe**

Particle morphology also evolves along the length of the exhaust pipe before dilution with ambient air [1]. A change in the particle morphology such as agglomeration during residence time in the exhaust pipe would be reflected in a corresponding change in the sensor signal. In addition, the exhaust gas cools as it travels down the pipe. Temperature differences between the upstream and downstream measurement ports were typically between 30K and 90K, depending on the upstream temperature and the exhaust

gas velocity. Thus, sensor position in the exhaust pipe impacted the sensitivity of the sensor.

The mean signal was measured at the upstream and downstream locations at various steady-state engine conditions covering a range of PM concentrations and exhaust gas velocities. In Figure IV-20 below, I plot the ratio of the steady-state signals of the upstream sensor to the downstream sensor against the residence time in the exhaust pipe, calculated from the exhaust gas velocity and the known distance (4.55 m) between the upstream and downstream sensor ports.

This decrease in the sensor signal was not believed to be a result of any change in the soot mass due to loss to the walls, but rather due to a change in the particle morphology. Measurements of soot mass concentration made by sampling at the upstream and downstream locations actually showed an increase in the captured soot mass, and this was believed to be the result of greater filter efficiency for larger particles.

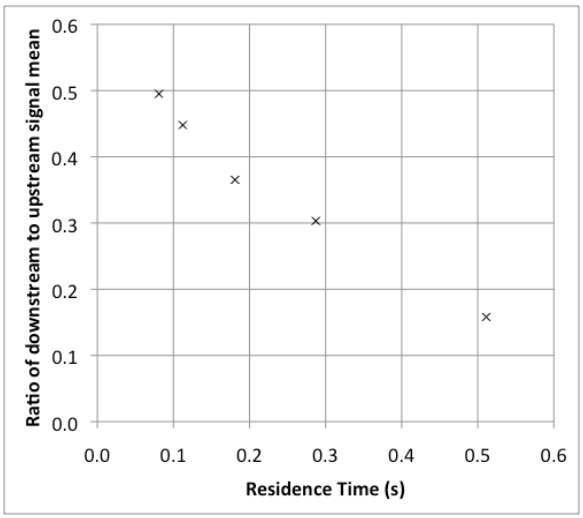


**Figure IV-20 Loss of signal strength downstream as a function of residence time in the exhaust pipe [42]**

As with the EGR effects, TEM images were made of particles at the upstream and downstream locations in the Cummins exhaust pipe to see whether any qualitative

changes in the soot morphology could be seen. Figure IV-21 shows TEM images of soot particles taken from the upstream sensor ports at the same operating conditions.

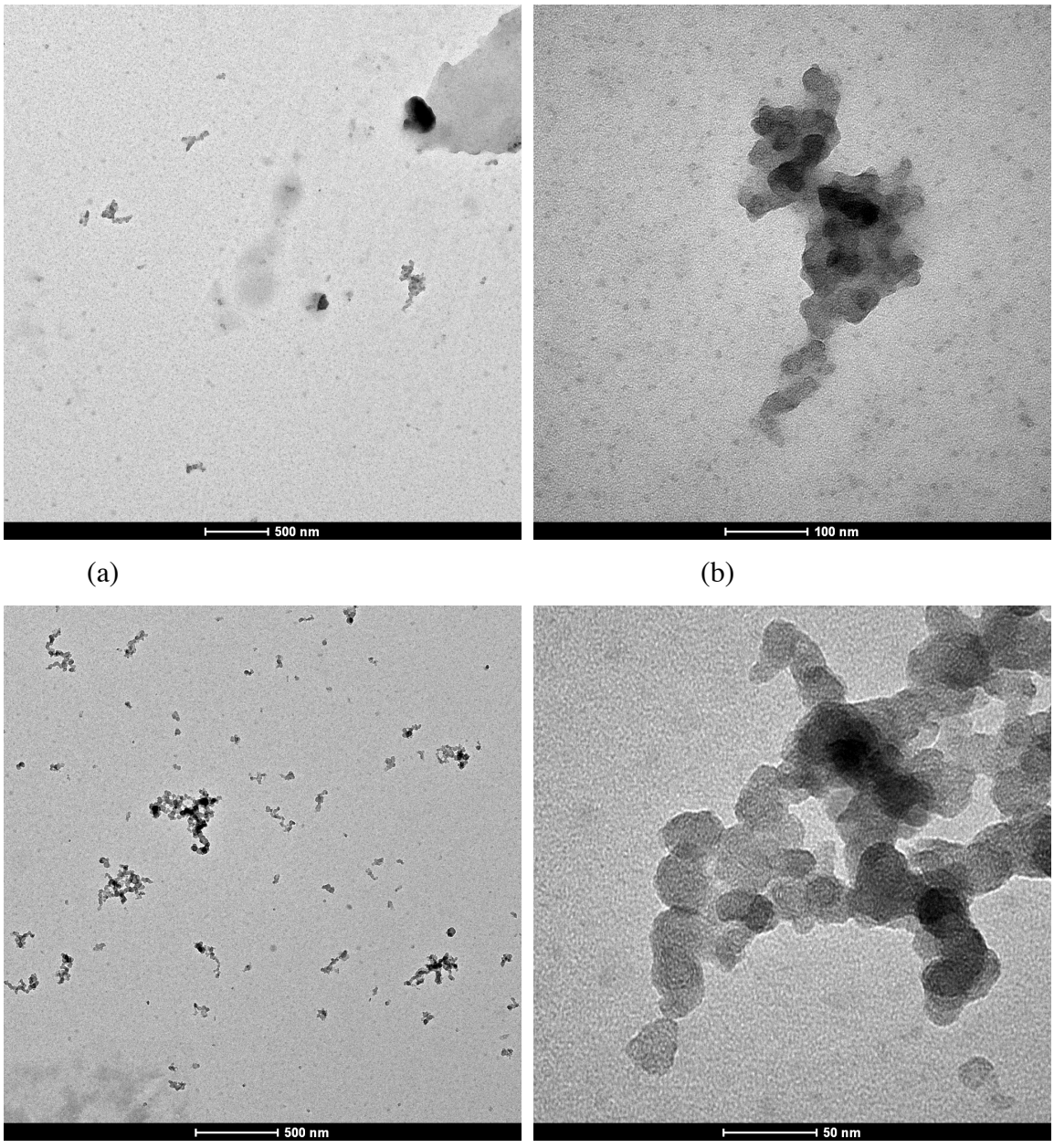


(a) (b)

(c) (d)

**Figure IV-21 TEM images of soot particles obtained in exhaust from the upstream sensor port of the Cummins engine at 1800 RPM and 300 ft-lbs torque with EGR levels of 0% in (a) and (b) and 20% in (c) and (d).**

As before, (a) and (b) show the 0% EGR case, and (c) and (d) show the 20%EGR case. By comparison with the images from Figure IV-19, it appears that at the upstream position, the sampled particles were smaller overall due to less agglomeration. Although again without a comprehensive image analysis-based survey of the particles it is not possible to say for certain whether there is a change in the size of the primary particles.

Again, the sensor showed decreased sensitivity to larger particles in the Cummins exhaust. A similar effect was seen in the studies of the sensor in the Yanmar exhaust. Recall that in the Yanmar, two distinct phases of response to a tip-in event were observed, the so-called puff and hump. The natural charge observed in the puff portion of a tip-in tends to start out with strong, short peaks, which decrease in magnitude and spread out spatially further downstream. To characterize the strength of the natural charge as the PM flowed downstream in the exhaust, I made a series of two- sensor measurements. For each measurement, a pair of sensors were installed, one, the *reference sensor*, in a downstream reference location, the other, the *test sensor*, in various upstream locations. Tip-ins were recorded with no voltage applied to the field electrodes. To account for the difference in sensitivity between the two sensors, a tip-in was recorded with both sensors at the same downstream location. The ratio of the magnitudes of the signals could then be used to normalize the test sensor against the reference sensor. Two calculations were made, a peak-to-peak measurement of the signal amplitude to capture the amplitude of the signal spikes, and a root-mean-square (RMS) measurement of the signal. The test sensor signal was normalized to account for the sensitivity difference, and then a ratio was formed from each pair of amplitudes. The results are plotted in Figure IV-22

The amplitude of the natural charge signal declined approximately exponentially with downstream distance. Both measures of amplitude showed the same trend, with the peak-to-peak amplitude declining most sharply. In the most extreme case, the spikes in the upstream signal had more than 16 times greater peak- to-peak amplitude than those in the downstream reference position.

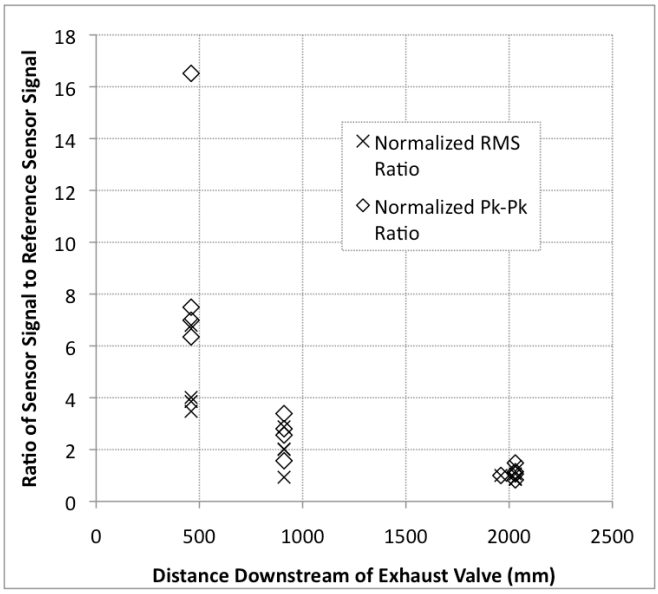


**Figure IV-22 Natural charge signal attenuation with downstream distance.**

The variability in the ratios, which was especially large for the upstream location, came from at least two factors. First was the variation in the strength of the tip-in. A tip-in with a high-pressure sooty blow-down process produced strong spikes in the signal, which decayed more rapidly along the length of the exhaust pipe. Thus, tip-in strength variation was more pronounced upstream than downstream. Second, heterogeneities in the exhaust stream meant that two sensors measuring only natural charge at the same location could produce different signals based on the local distribution of charge within the exhaust puff. As the mass of charged particles moved downstream, flow and electrical diffusion processes increased the homogeneity, and thus the variation decreased with downstream distance.

Thus, sensor sensitivity to soot decreased with downstream distance, due to two factors. Where natural charge is significant, diffusion and mixing processes decrease the amplitude of peaks in the local charge concentration, and lead to neutralization of the charge. For locally induced charge, the agglomeration of particles in the exhaust pipe makes them less effective at triggering discharge from the field electrode and reduces particle mobility between the two electrodes.

**Detection of Simulated DPF Failure**

To test the ability of the sensor to detect simulated failure of a DPF by leakage of unfiltered exhaust gas, sensors were installed in ports upstream and downstream of the DOC/DPF. The engine and DPF were warmed up and brought to thermal equilibrium by running 10 minutes or more at the conditions of the test until the exhaust gas and DPF internal temperature measurements were at steady state. Initially, all of the exhaust flow was directed through the DPF. At a specified time, the valve to the bypass loop was slowly opened. After 20 seconds, the valve to the DPF was closed, thus diverting all of the flow through the bypass. Then after 20 seconds, the process was reversed, first by opening the valve to the DPF, and then by closing the valve to the bypass. Steady-state averages were calculated for the initial state, the intermediate state, and the full bypass state. Figure IV-23 shows the time-series data from two such tests, one at a 700 RPM and low load, and the other at a high-speed, low load condition. In both tests, the EGR fraction was 0. In the 2200 RPM case, the signal from the upstream sensor is shown for comparison.

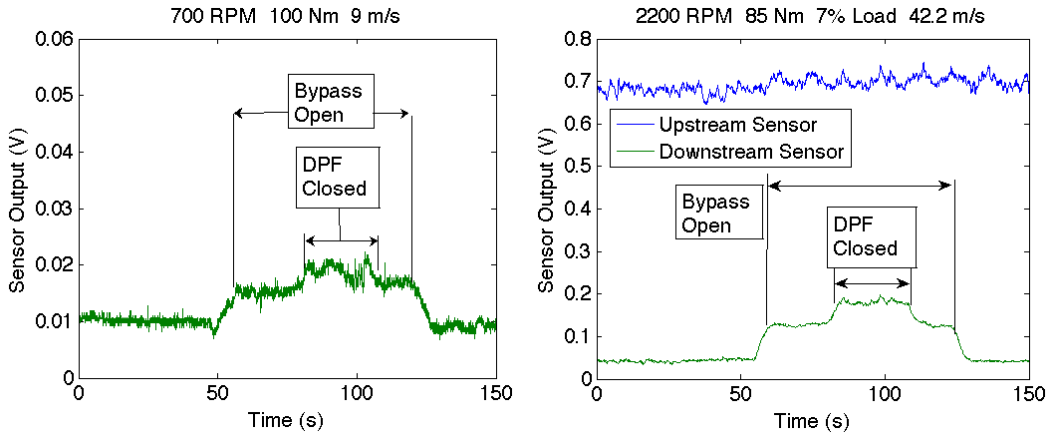


**Figure IV-23 Simulation of DPF leak at 700 and 2200 RPM at light load**

Several such tests were conducted ranging from idle condition (where the sensor had the least sensitivity) to partial load (50%, 1800 RPM). At each condition, the mean value of the sensor signal was calculated for the initial DPF-filtered state, and for the partial and full bypass states. A percent increase in the signal over the initial DPF-filtered

baseline signal ($V_{mean,DPF}$) could then be calculated for the partial and full bypass conditions as follows

$$\%\text{increase} = \frac{V_{mean} - V_{mean,DPF}}{V_{mean,DPF}}$$

These percentage increases are shown plotted against fueling rate in injection mass per second in Figure IV-24. Note that the increase for the partial bypass condition is about half the increase for the full bypass. In the case with the greatest sensitivity, the full-bypass produces a signal increase of 620% over the baseline condition. In the least sensitive case, at 700RPM idle, the increase was 88% for full bypass.

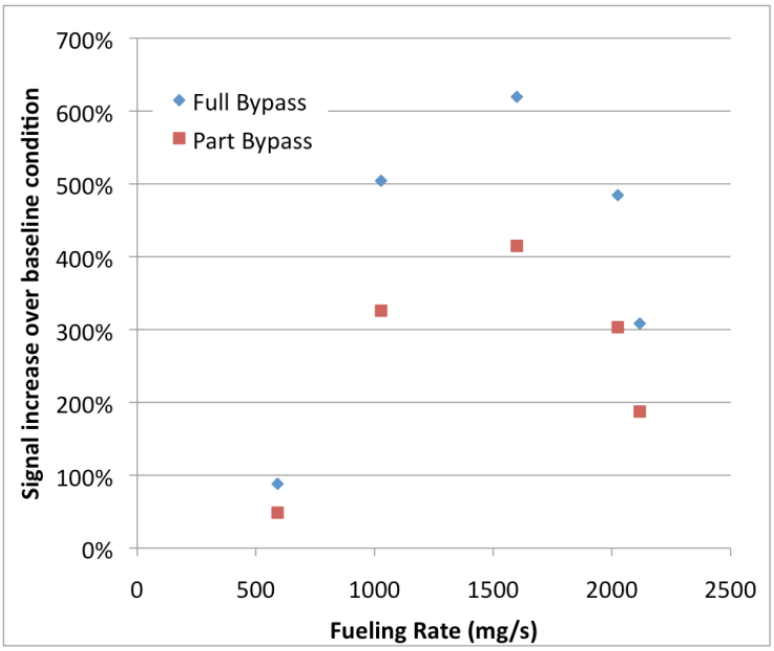


**Figure IV-24 - Increase in PM sensor output during DPF leak event at various fueling rates**

The root-mean-squared noise in the signal in the post-DPF baseline condition was 7 mV for a mean signal value of 280 mV. The signal for the failed DPF (full bypass) is an increase of 250 mV over the baseline signal. We can define a signal-to-noise ratio based on the noise in the baseline condition and the full-bypass signal increase. For the idle

condition, the signal-to-noise ratio is 36:1. The resolution of the sensor for leak detection with 95% confidence (1.65 standard deviations) is 12 mV over the baseline condition. Based on gravimetric filter measurements of the soot concentration at 700 RPM idle (20 $mg/m^3$, or 285 mg/bhp-hr) and the known sensitivity of the sensor in this condition, this represents a leakage of about 0.7 $mg/m^3$, or 10 mg/bhp-hr.

Thus, even at the operating condition with the lowest sensitivity (700 RPM idle), detection of leakage at the federal limit of 15 mg/bhp-hr is possible. Sensitivities at other conditions are even more favorable for identification of DPF failure. At 1800 RPM and 40% load (800 kPa BMEP), the measured soot concentration was 6 $mg/m^3$ (4 mg/bhp-hr), the root-mean-squared noise in the baseline signal was 8 mV, and the full-bypass increase in the sensor signal was 1.8V. Thus, the resolution for DPF failure detection at that condition was 0.005 $mg/m^3$ (0.003 mg/bhp-hr), and the signal to noise ratio was 220:1.

## DESCRIPTION OF THE SENSOR MECHANISM

In this section, a comprehensive qualitative picture of the physical mechanism at work in the electronic particulate matter sensor is developed based on the observations presented above. The behavior of the sensor was substantially different in exhaust from the Yanmar and the Cummins. Many of the correlations developed by Warey did not hold in the exhaust of the Cummins engine. Therefore, a new understanding of the sensor's mechanism is necessary.

### Detection of natural charge

The sensor responded to the presence of charged particles in the exhaust gas in the same manner that an ion probe would. The signal was proportional to the charge density of the incoming exhaust gas stream; particles carried charge originating in the combustion process to the sensor. At constant particle density and charge density, the sensitivity of the sensor increased with the exhaust gas velocity due to the increased charge flux. The electric field had the effect of attracting naturally charged particles from a larger volume of the surrounding gas than in a non-energized sensor. While the sensor functioned as an ion-probe with the electric field turned off, the electric field increased its sensitivity by increasing its effective capture area.

In the Yanmar engine, the natural charge was found to dominate in the puff phase of a tip-in. The natural charge in a tip-in puff had a bipolar and heterogeneous density distribution. The distribution of charge became less heterogeneous downstream due to diffusion and mixing, thus resulting in the observed exponential decrease in amplitude of the natural charge signal with downstream position.

### Active Region

The PM sensor also generated a current in the presence of neutral carbon particles when a bias voltage was applied to the field electrode. Thus, the sensor was not

dependent on incoming charge to produce a signal but rather had some mechanism for generating currents across the electrode gap.

The physical process resulting in a current at the sensing electrode was initiated in the inhomogeneous electric field in an "active region" near the electrode surfaces where the electric field was a maximum. The behavior of the sensor with respect to its orientation in the flow revealed that particles not already carrying charge had to come into contact with the active region of the field electrode in order to produce a signal in the sensor. Simple contact with the field electrode was insufficient to initiate a sensor response; otherwise particles would have been charged equally well with the sensor in any orientation where flow was not blocked to the field electrode. Instead, it was seen that inner face of the electrode was the active region and that in order to generate a signal, it was necessary for there to be a flux of particles to the active region. The observed pattern of changes in sensitivity when the field electrode was masked by the sensing electrode showed that an active region existed on the field electrode only.

Figure IV-12 has been updated below in Figure IV-25 to show both the passive region, where the electric field was concentrated but insufficient in strength to initiate ionization, and the active region, where particles interacted with the electric field to release charge carriers, are labeled in the diagram. The active region was shown here for the sake of discussion as a semicircle.

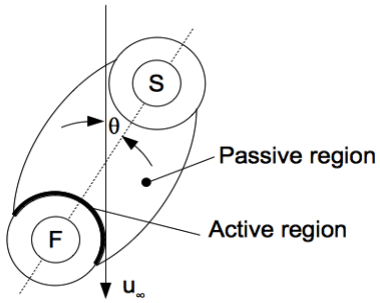


**Figure IV-25 Location of active and passive regions in the sensor electrode gap.**

Geometrically, the flux of soot particles, $\Gamma$, to the active region is given by

$$\Gamma = \Gamma_0 \left( \frac{1+\cos(\theta)}{2} \right),$$

where $\Gamma_0$ is the incoming flux of particles, not counting the effect of flow masking by the upstream electrode. Thus, not counting the effect of the upstream electrode, the particle flux would be at a maximum when $\theta$=0°. At $\theta$=180°, the active region of the field electrode is shielded from the oncoming flow and $\Gamma$ is 0. In reality, flow effects are significant. At $\theta$=180° flow recirculation brings a flux of particles to the active region. At $\theta$=0°, the sensor electrode is upstream, and the flow in the gap would be characterized by a turbulent wake. (See the Reynolds Number calculation in Appendix A). In the curves plotted in Figure IV-26, $\Gamma/\Gamma_0$ is plotted for three cases: no consideration of blocking by the upstream sensor (solid line), complete blocking of flow to the active region by the upstream sensor using a geometry typical of the sensors tested (dotted line), and an intermediate solution using a weighted average of the two previous solutions to simulate the effects of flow recirculation or the flux provided by a turbulent wake in the electrode gap (dashed line).

This theory closely matches the results plotted in Figure IV-13 and Figure IV-14. When the field electrode was blocked by a smaller sensing electrode upstream, the reduction in signal was smaller than in the symmetric electrode case because there was still a particle flux to the field electrode when it was optimally oriented, with $\theta$=0°. However, when the field electrode was blocked by a much larger upstream sensing electrode, the reduction in signal was greater than the symmetric electrode case because the particle laden flow was more effectively blocked from reaching the active region of the field electrode. These results confirm the presence of an active region on the inner face of the field electrode and that the sensitivity of the sensor is strongly influenced by the level of exposure of the active region of the field electrode to the exhaust flow when there is not a high density of naturally charged particles.

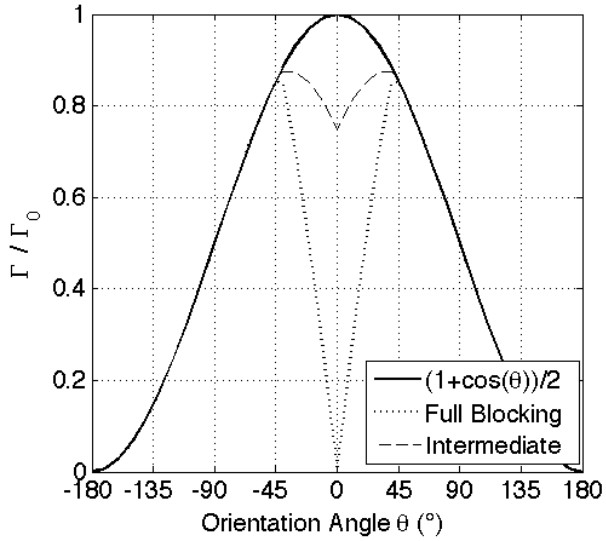


**Figure IV-26 Geometric/flux effect of sensor orientation**

In the absence of PM, the electric field of the sensor was too weak to cause ionization of gas in the electrode gap, that is, to form a steady-state plasma discharge. However, the presence of a conductive particle enhanced the local electric field in the active region to the point that spontaneous electron emission occurred as the particle's floating potential came into equilibrium with the surrounding electric field. Modi et al [46] found that electrodes coated with carbon nanotubes reduced breakdown voltages in the air between electrodes having small gaps of between 25-140 μm by approximately 40-70%. An accumulation-mode diesel soot particle has a structure built up of primary particles of about 20nm in diameter. The length of an agglomerated particle could be 100nm or more, with a rod-like or branched structure. Because the core structure of the particle was made of conductive carbon, the particle could act as an electric field intensifier in the same way as the nanotubes of Modi's study. Thus, the electric field concentration around small particles and at the ends of the longer, agglomerated particles was strong enough to support spontaneous emission of electrons. This initial ionization, known as a Townsend discharge, released an ionization cascade where electrons were stripped from neutral molecules in the exhaust gas which then migrated across the gap

and delivered the charge flux to the sensing electrode.; this occurs more readily to electropositive species such as molecular nitrogen which tended to donate electrons [48].

The presence of an active charging region but no steady-state current in the absence of particles indicated that no steady-state discharge was present in the electrode gap. However, the charge creation process is thought to be similar to that found in electrostatic precipitators (ESP's), which charge small particles in an electric field using a corona discharge. Ionization in the sensor took place in the strongest regions of the inhomogeneous electric field at the electrode surface. The regions where the field was too weak to maintain ionization served to prevent arcing between the cathode and anode. The PM sensors operated at a voltage level below the minimum onset voltage for a current to be created in the absence of particles.

**Charge Carrier Mobility**

The symmetry of the sensor response to the polarity of the voltage bias applied to the field electrode suggested that the particles themselves did not carry the charge, or at least played a limited role. If the field electrode was given a negative voltage bias, the sensor response to particulate matter was the same magnitude, but of opposite sign relative to a positive voltage bias on the field electrode. Therefore, there was symmetry in the creation and transport of charge carriers, particles, ions, and electrons for either positive or negative voltage bias. On the PM sensor, the field electrode functioned as an anode if it had a positive bias and a cathode if it had a negative bias; the sensing electrode played the opposite role in either case.

Analysis of sensor orientation effects showed that exposure of the active region to the flow was more significant than the direction of charge migration relative to the bulk exhaust flow direction. Therefore, the migration velocity of the charge carriers had to be much greater than the velocity of the exhaust gas near the electrodes. Insight into the behavior of charged particles was provided by the literature of electrostatic precipitators [47-49]. The magnitudes of the exhaust gas velocities suggested that the particles

themselves were too slow to move from the field electrode to the sensor electrode in the residence time available. Particle mobility data expressed as drift velocity vs. particle size for several electric field strengths is available in the literature on electrostatic precipitation [47]. The migration (drift-diffusion) velocity achieved by a particle is a function of the balance of electrical and drag forces on the particle. Since the motions of individual particles are governed by Stokes flow (see calculations of Knudsen and Reynolds numbers in Appendix A), the drag force is directly proportional to the particle diameter. The saturation charge obtained by an individual particle is a function of the square of the particle diameter, thus the overall migration velocity is a function of the particle diameter and of the field strength. Parker presents theoretical migration velocities for particles in an electric field (see Figure IV-27) of a strength comparable to that present in the sensor. The electric field in the sensor had a mean strength of $5x10^5$ V/m, or 5 kV/cm, corresponding to the uppermost curve in the figure. In an ESP, a 100 nm particle has a drift velocity of about 0.5 m/s, and a particle of 10 nm has a drift velocity about 8 m/s in air at standard conditions. These migration velocities would be far too slow to move upstream against exhaust gas flow at 10-50 m/s. In addition, the curves presented are valid for an ESP, where particles have sufficient residence time (at least 0.1s, according to Parker [47]) to achieve a full saturation charge. A particle moving with the exhaust gas at 10 m/s would spend at most $2x10^{-4}$ s in a 2mm electrode gap, so these migration velocities represent an upper limit for particles in the sensor.

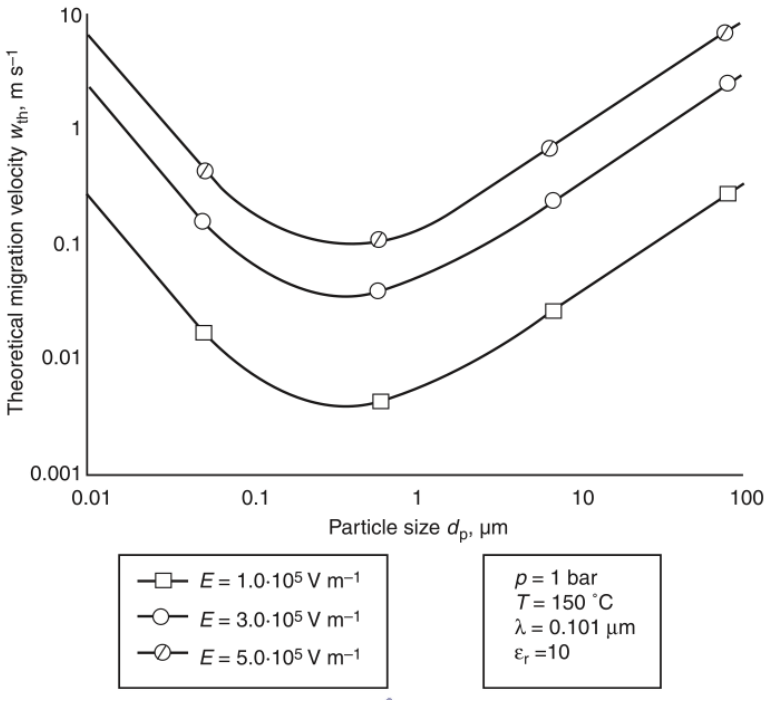


**Figure IV-27 Particle migration velocity as a function of diameter [47]**

However, as I have shown, the sensitivity of the sensor was highest when the electrodes were oriented so that migration would be against the free-stream direction and the effective drift-diffusion velocity of a particle would be negative.

Based on a tabulation of ion mobility for various gases by Bohm [48], molecular ion drift velocities are estimated in the range of approximately 50-100 m/s, and electron mobility is about two orders of magnitude greater than that. [50] This velocity is enough to provide a signal relatively unaffected by the free stream exhaust velocities present in this study. This suggests that electrons and molecular ions rather than particles are the most active charge carriers for the sensor.

Thus the different effects of exhaust gas velocity between the naturally charged (Yanmar) exhaust and the electrically neutral (Cummins) exhaust are explained by the different mechanisms at work. In the natural-charge rich exhaust of the Yanmar engine, the sensitivity to velocity is well explained by a simple model of charge flux directly to

the sensing electrode in which an increased exhaust gas velocity at constant mass concentration delivers a greater rate of charge per unit time, thus increasing the sensitivity of the sensor. In the Cummins engine, the particles do not carry a substantial natural charge. Rather, they become charged in the active region of the field electrode, releasing an electron cascade and stimulating a Townsend discharge in which electrons or molecular ions carry charge across the electrode gap. The mobilities of electrons and ions are high enough to migrate against the flow around the electrodes.

**Charge Induction**

Charge creation in the active region is thought to be the result of the same mechanisms active in ESP's and described in the ESP literature. If the field electrode is positive, I postulate that electrons stripped from the molecules are accelerated to the field electrode, and positive molecular ions are created and accelerated toward the sensor electrode into what is known as the "passive region" (which is much bigger than the active region) where the electric field is too weak to cause further ionization. These positive ions are accelerated by the electric field to the negative sensor electrode where they give up their positive charge, creating the measured signal. It is likely that some positive ions collide with some of the particles in the gap, exchanging charge and leaving some particles with a positive charge. Due to particle mobilities, however, only the smallest particles could likely contribute to the observed sensor signal.

If the field electrode is negative, the electrons stripped from the neutral molecules in the active region are accelerated toward the positive sensor electrode. On the way, they may combine with oxygen and other electronegative species in the exhaust gases. While molecular nitrogen is electropositive [47], oxygen is electro-negative [49]; that is, it will accept electrons. The electronegative molecules become negative molecular ions that are accelerated toward the positive sensing electrode. Like positive ions, on the way they may collide with neutral particles, transferring charge and, overall, giving a negative charge to the particles which are accelerated toward the positive sensor electrode, again

limited by mobility. So for either polarity, the net effect is the same, the charge carriers are driven to one or the other electrode; at the sensor electrode they give up charge (positive or negative depending on the sense of the bias voltage) to become neutral.

The motions of the ions in the electric field have two components which affect the nature of the particle charging: a motion induced by the electric field and a diffusive motion governed by Fick's law [49]. These govern the two mechanisms considered responsible for the charging of particles by molecular ions. The first is *ion bombardment* in which the local electric field drives the impacts between ions and particles. Ion-bombardment is the main mode of charge acquisition of a particle in a corona discharge [51]. A complete description of the ion-bombardment mode given by Liu and Yeh in 1968 [52] is applicable over a wide range of particle sizes, from many tens of microns to sub-micron diameters. The particles distort the local electric field in the vicinity of the particle due to the difference in the dielectric properties of the particle and that of the surrounding gas [48]. Ion bombardment is considered the dominant mechanism for larger particles, on the order of 1 μm or larger. The second particle charging mechanism is *ion diffusion*. This is a less directional mechanism where the impacts between ions and particles are thermodynamic, governed by the random molecular motion of the molecular ions with particles and acting in the general direction of the gradient in ion concentration. This mechanism is considered dominant for small particles, usually considered to be of diameter 100 nm and smaller. Neither mechanism dominates over the intermediate particle size range.

The experimental data collected in this study suggested that the PM sensor had a greater sensitivity to smaller particles. This is consistent with the ESP literature. After a particle has initially picked up a charge, this charge tends to deflect ions away from the particle. The greater the particle charge, the slower it accumulates additional charge. Thus, smaller particles will have a greater charge to mass ratio than larger particles [48].

## DEVELOPMENT OF A PHYSICAL MODEL

A physical model of the sensor operation must treat two modes of charge flux to the sensor electrode: natural charge, and uncharged PM that triggers Townsend discharges. When detecting natural charge the sensor electrode is operating as an ion probe and relies on the impaction of charged soot particles on the sensing electrode. In this mode (observed with the Yanmar single-cylinder engine), the electrode charge flux (sensor signal) is proportional to the incoming flux of charged particles and has a positive correlation with exhaust gas velocity of the same particulate concentration, and the effect of increasing electric field strength is to increase the number of naturally charged particles attracted to sensor electrode.

In the Townsend discharge mode, particles entrained in the exhaust gas stream enter the active region having high electric field intensity near the surface of the field electrode and initiate electron cascades, which lead to the transport of positive or negative molecular ions across the electrode gap, providing a flux of charge to the sensor electrode.

### Natural Charge

It is important first to understand the level of charge carried by PM. The PM in diesel exhaust carries a natural charge that is created during the combustion process. [7,15,16,53,54] PM ionized this way carries charges of both polarity, with temporal and spatial variability. According to Jung and Kittelson [7], it is the accumulation mode particles formed in combustion that carry the majority of the natural charge, and depending on the operating conditions, the charge fraction can be from 0.2 to 0.85 of the particles. For this research, there was no access to equipment that would allow the characterization of the distribution of charges on the particles due to the combustion process, but distributions available in the literature suggest that charge per particles would be one or two fundamental charge units, for the sizes observed in this research. This is confirmed by the data reported in 1986 by Kittelson and Pui [15] in Figure IV-28

of charge per particle measured for a VW Rabbit diesel engine.

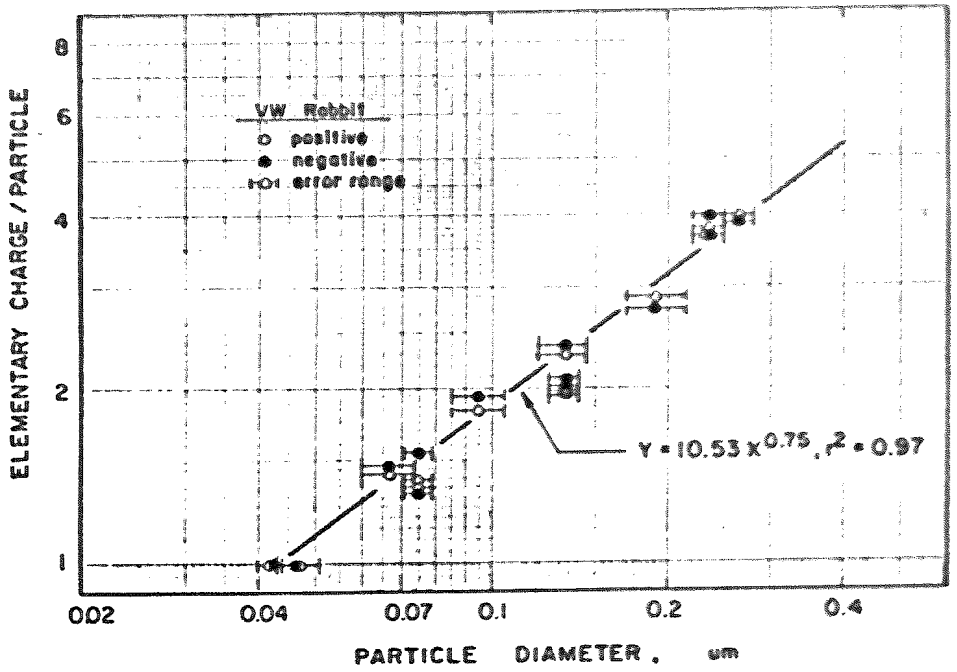


**Figure IV-28 Measured charge per particle for a VW Rabbit diesel engine [15]**

If we assume the characteristics of soot from the VW Rabbit diesel engine to be similar to that found in the exhaust of the Yanmar engine, we can assume that most of the soot particles in the Yanmar exhaust had a natural charge of one or two fundamental units.

### Advected Particles

Depending on the engine operating conditions, from 20% to 85% of accumulation mode particles leave the combustion chamber carrying a charge [7,15,16]. Soot particles acquire charge in the combustion process through a number of processes. A certain proportion of these charged particles come close enough to the sensing electrode to transfer charge to the electrode. The rate of charge transfer to the sensing electrode in this way is the *advected electrode current*, $\Lambda_a$.

$$\Lambda_a = \Gamma_a A_c$$

Here $\Gamma_a$ is the charge flux (C/m$^2$s) carried by particles in the exhaust stream, and $A_c$ is the effective capture area of the sensing electrode. It is useful to further break down the charge flux in the exhaust stream:

$$\Lambda_a = u_\infty n_{PM} \chi \bar{q}_{PM} A_c$$

where $u_\infty$ is the exhaust gas velocity, $n_{\mathrm{PM}}$ is the number density of soot particles, $\chi$ is the fraction of soot particles carrying an electric charge, and $\bar{q}_{PM}$ is the average charge carried by a soot particle. We can rearrange the expression to solve for electrode current as a function of PM number density.

$$\Lambda_a = u_\infty n_{PM} \chi \bar{q}_{PM} A_c$$

Measurements of sensor sensitivity were made in terms of the mass concentration of soot, so the distribution of particle sizes is important. Let us consider a number density function of particle diameter, $N_{PM}(D)dD$ such that

$$n_{PM} = \int N_{PM}(D)dD .$$

The usual form for diesel soot particle size distributions, as seen in Figure I-1 is a lognormal distribution with one or more modes in terms of a mobility diameter *D*. For the purposes of this discussion, the exact definition *D* is not critical, although the electrical mobility diameter is frequently reported, defined as the diameter of a spherical particle that has the same electrical mobility as the particle in question. We can make a rough estimate of particle mass by assuming a bulk density $\rho_{PM}$ (in reality a function of D due to the branched nature of agglomerated particles) and a mass to volume relationship depending on the "fractal dimension" of the particle. A fractal dimension of 1 indicates a linear morphology, and a fractal dimension of 3 indicates a spherical morphology. Agglomerated soot particles have fractal dimensions of between 1.5-2.5 [24,27,36,55,56]

thus the particle mass bears a roughly 1.5-2 power relationship with diameter. Thus, individual particle mass $\hat{m}_{PM}$ goes approximately as

$$\hat{m}_{PM} \propto D^2 .$$

For naturally charged particles, the individual charge on a particle $\hat{q}_{PM}$ is a weak function of diameter. Kittelson et al [15], report a ¾ power relationship between particle diameter and number of natural charge units for engines similar to the Yanmar.

$$\hat{q}_{PM} \propto D^{3/4} .$$

It is evident, then, that natural charge per mass is dependent on the size of the individual particles:

$$\frac{\hat{q}_{PM}}{\hat{m}_{PM}} \propto \frac{D^{3/4}}{D^2} = D^{-5/4},$$

Thus, changes to the size distribution of the particles have an impact on the mean natural charge carried per mass of PM, $\overline{q}_{PM,mass}$, even if the overall mass concentration is constant.

We define a sensor sensitivity to naturally charged PM $\sigma_a$ as the electrode current divided by the mass concentration, $m_{PM}$:

$$\sigma_a = \frac{\Lambda_a}{m_{PM}} .$$

Substituting for $\Lambda_a$, the sensitivity is given in terms of the exhaust gas velocity, the charge fraction, the charge per particle and the capture area.

$$\sigma_a = u_\infty \chi \overline{q}_{PM,mass} A_c$$

The sensitivity of $\sigma_a$ to exhaust gas velocity is given by

$$\frac{\partial \sigma_a}{\partial u_\infty} = \chi \bar{q}_{PM,mass} A_c \,.$$

The sensitivity depends on the size distribution because $\bar{q}_{PM,mass}$ is a function of the particle size distribution.

The effect of increasing field voltage is to increase the effective capture area of the sensing electrode by increasing the field strength. For the purposes of considering effective capture area of the sensor, we can approximate the field electrode to be a line source and the shape of the electric field to be roughly cylindrical around the field electrode. According to Coulombs Law, the intensity of an electric field is inversely proportional to the square of the distance, $r$, from the field source.

$$E \propto \frac{1}{r^2}$$

The effective capture area of the sensor can be approximated by a cylindrical shell of a critical radius $r_{crit}$ around the electrode inside which the force on a charged particle will cause it to migrate to the sensing electrode. Thus the critical radius is proportional to the square root of the electric field intensity.

$$r_{crit} \propto \sqrt{E}$$

The effective capture area of the electrode is given by the surface area of the sides of the cylinder

$$A_c = 2\pi r_{crit} l$$

where $l$ is the electrode length. We can now show the effect of a change in electric field strength on the sensor sensitivity:

$$\frac{\partial \sigma_a}{\partial E} \propto \frac{u_\infty \chi \bar{q}_{PM,mass}}{\sqrt{E}}$$

The mean electric field intensity is given by $E/L$, where $L$ is the electrode gap width. Thus, for a doubling of the field voltage or a halving of the electrode gap width, we would expect a factor of $\sqrt{2}$ increase in sensitivity of the sensor.

This measurement of the natural charge of the exhaust is in essence the ion-probing function of the sensor and matches the modeling and description in previous works, including those of Warey [43] and Schweimer [16].

Thus, for a theoretical exhaust environment in which the natural charge is dominant and charge fraction and size distribution are invariant, the sensor response for any engine speed should collapse to a single linear curve proportional to charge fraction, number density, and sensor electrode area if plotted against PM mass flux. A constant offset would be explained by the local-charging function of the sensor. The exhaust of the Yanmar engine, which was higher in natural charge density, roughly approximates this condition, at least by comparison with the Cummins engine. Variations in the charge fraction and size distribution (with its consequent changes in mean charge per particle mass and particle number density) show up as deviations from the straight-line correlation shown in Figure IV-29 below, where the data from Figure IV-8 is combined with gravimetric soot concentration calibration data across a range of engine speeds from 1200 to 2600 RPM and idle to moderate (%50) torque loads.

The data point at 1000 mg/m$^2$-s and 450 mV mean sensor output was taken at the highest load-speed combination (6 Nm, 2600RPM) of the series. Our experience with the Cummins engine leads us to expect a smaller mean particle diameter and higher number density at higher load conditions. Here, a difference in particle morphology would lead to a higher signal component from the locally-induced charging mechanism. The low-signal data points near 500 mg/m$^2$-s and 30 mV mean signal were from low-speed, low-load runs, where the charging fraction was likely lower due to the very low fueling rate. Thus their negative deviation from the linear correlation could be explained by an anomalously low charge fraction.

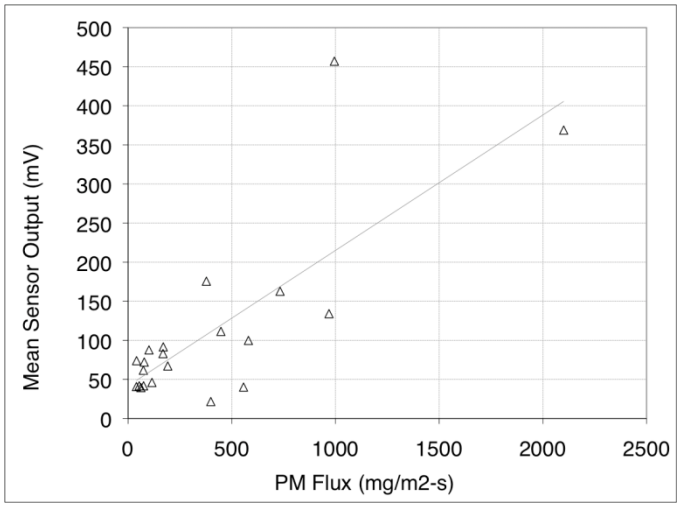


**Figure IV-29 Calibration of sensor in natural charge-rich Yanmar exhaust with mass flux of PM**

**Relationship of Particle Size to Induced Charge**

Now we examine the charge per particle in more detail. There are two regimes of particle charging in an electric field: diffusion charging and field charging. In either case, the charge acquired by a particle depends on its size, its dielectric constant, the electric field intensity, the concentration of ions in the discharge, and the time of exposure of the particles to the ions. For particles under 1 $\mu$m in diameter, diffusion charging (ion to particle) becomes significant, and the particles become charged at a rate given by Liu and Yeh [52] [1]

$$\frac{d\hat{q}_{PM}}{dt} = \frac{e}{4\varepsilon_0}\mu_i n_i q_s \left(1 - \frac{\hat{q}_{PM}}{q_s}\right)^2$$

where $\hat{q}_{PM}$ is the number of elementary charges per particle, $e$ is the elementary charge, $\varepsilon_0$ is the vacuum permittivity, $n_i$ is the ion number density, and $\mu_i$ is the ion mobility. $q_s$, the saturation charge number on a particle, is given [52,57] by

[1] Care must be taken to apply the appropriate conversion to relations given in older literature, which is typically written with the cgs-Gaussian unit system and uses statCoulombs and statVolts, introducing factors of $\frac{1}{\sqrt{4\pi\varepsilon_0}}$ to the units of fundamental charge, electric field strength, and electric mobility.

$$q_s = \left(1 + 2\left(\frac{\varepsilon_{PM} - 1}{\varepsilon_{PM} + 2}\right)\right)\frac{\varepsilon_0}{e} ED^2$$

where $\varepsilon_{PM}$ is the relative permittivity of the PM (taken to be about 10). The saturation charge curves for diffusion and field emission charging mechanisms are shown in Figure IV-30 from Liu & Yeh.

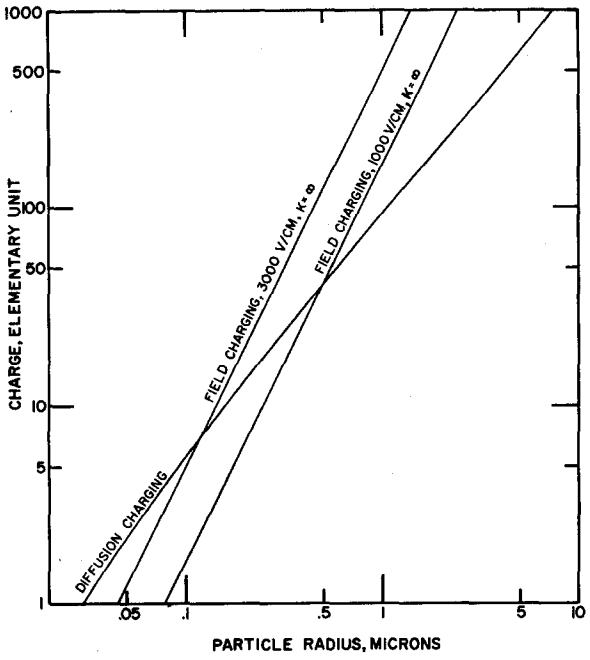


**Figure IV-30 Charge number versus particle size [52]**

It is useful to normalize the charge level on a particle by the saturation charge:

$$q^* = \frac{q_{PM}}{q_s}$$

By integrating the expression for charging rate above, we get

$$q^* = \frac{Ct}{Ct + 1} \text{ with}$$

$$C = \frac{en_i\mu_i}{4\varepsilon_0}.$$

Thus, $t=1/C$ represents the 50% charging time. Using $e$=1.9x10$^{-19}$ C, $n_i$ = 1x10$^{14}$ (#/m$^3$) (based on numerical modeling performed later), $\mu_i$ = 1.5x10$^{-3}$ (m$^2$/Vs) [58], and $\varepsilon_0$ =8.9x10$^{-12}$ (C/Vm), C = 675(1/s), and the 50% charging time is about 1.50 ms. The residence time $t_r$ for the particle to charge in the field can be found by considering a critical interaction distance $\delta z$ and the particle velocity to be that of the free-stream $u_\infty$, thus

$$t_r = \frac{\delta z}{u_\infty},$$

If we take the electrode gap width as the interaction distance, $\delta z$ = 002 (m). Observed exhaust gas velocities in the Cummins were in the range 10-60 (m/s), thus the residence times fell in the range 3-20x10$^{-5}$ s. Based on these values, q* fell in the range 0.02-0.1 According to the relation above for saturation charge, a 40 nm particle will accept 0.11 fundamental charges. Because the charge levels are discrete, we can view this as a statistical average, where, for example in the 10 m/s case, the charging level is 1 and the charge fraction is 0.11. For 100nm particles, the saturation charge is 0.7 fundamental units.

By substituting the term for residence time into the q* expression, we get

$$q^* = \frac{1}{1+\frac{u_\infty}{C\delta z}}.$$

$C\delta z$ has units of (m/s) and represents a "50% charging velocity," meaning that particles moving at that velocity would achieve half of their saturation charge. With our geometry, the value of $C\delta z$ is about 1.35 (ms). Because $u_\infty$ is large with respect to $C\delta z$, for the purposes of velocity sensitivity, $q^* \cong \frac{C\delta z}{u_\infty}$, At the same time, however, the flux of particles coming to the electrode is proportional to $u_\infty$, so that the overall sensitivity to

velocity is zero, or small if $u_\infty$ is close to $C\delta z$. We can therefore assume that the particles generally have a unit charge, and the fraction charged stays generally constant with velocity due to a tradeoff between the saturation charge level and the number of particles entering the active ionization region at the electrode surface.

**Discharge Model**

In the second mode of sensor operation, particles are charged as they enter into the active region of the field electrode. Warey proposed a mechanism of charging by particle impact with the field electrode and transport of charge by the particles themselves [43]. This does not fit well with a picture based on the kinetic theory of gases, since in the absence of strong electric field gradients, sufficiently energetic collisions for ionization typically only occur in high speed or high temperature flows. In addition, our study of the orientation effect of the sensor showed that collision of particles with a part of the field electrode that is not in the active ionization region is insufficient to charge the particles. Because the electrodes are conductive around the entire circumference of the ceramic substrate, the number of particle collisions with the field electrode was constant except when the sensing electrode was upstream blocking the flow. According to Warey's proposed mechanism, the highest sensitivity should have been when the field electrode was oriented upstream and particle migration was in the same direction as the free stream velocity because particle migration velocities were generally less than the free stream velocity. However, it was in fact the orientation with the lowest sensitivity. Also, based on the migration velocities of the particles relative to the velocity of the exhaust free stream, it is evident that soot particles do not carry the charges across the electrode gap. Rather, a mechanism with lighter, more mobile charge carriers must be at work.

The presence of an active ionization region, a weak plasma near the field electrode surface, however, appears to explain the observed phenomena based on well-studied ionization theory. In particular, in a Townsend discharge, a gas is ionized, yet many of the other plasma features, such as formation of sheaths near electrode surfaces

and the self-consistent electric fields, are absent due to the relative weakness of the field. The active region at the field electrode surface is an ionizing environment; while there can be a steady-state flow of ions or electrons across the gap, the field is not strong enough to cause further ionization across the entire gap, allowing breakdown. However, a soot particle entering the active region would become ionized and trigger an electron avalanche, releasing electron-ion pairs to migrate across the gap.

This mechanism where the ionization of a particle or molecule releases an electron avalanche is known as the Townsend mechanism. It is characterized by a Townsend coefficient, $\alpha$, which is a measure of the number of electron-ion pairs released per unit distance. The momentary release of electrons by a particle being charged in the active region, however, should be sufficient to trigger a non-self-sustaining discharge. Shin and Raja [58] present a model for a Townsend discharge that occurs between two dielectric barriers, in an atmospheric pressure electrode gap, also known as an atmospheric-pressure glow (APG) discharge. APG discharges are notable for operating at relatively high (atmospheric) pressures and at low stimulation frequencies (as low as 0 Hz, DC). The presence of a non-self-sustaining APG explains the charge transfer mechanism of the sensor.

For the purposes of modeling the sensor, the dielectric barrier aspect included by Shin and Raja [58] has been removed from the model. It consists of an upper and a lower electrode, separated by a gap, $L$ and supporting a potential difference $V_{source}$, as shown in Figure IV-31. The upper electrode has the source voltage applied and is analogous to the field electrode in the sensor. The lower electrode is grounded and is analogous to the sensing electrode in the sensor.

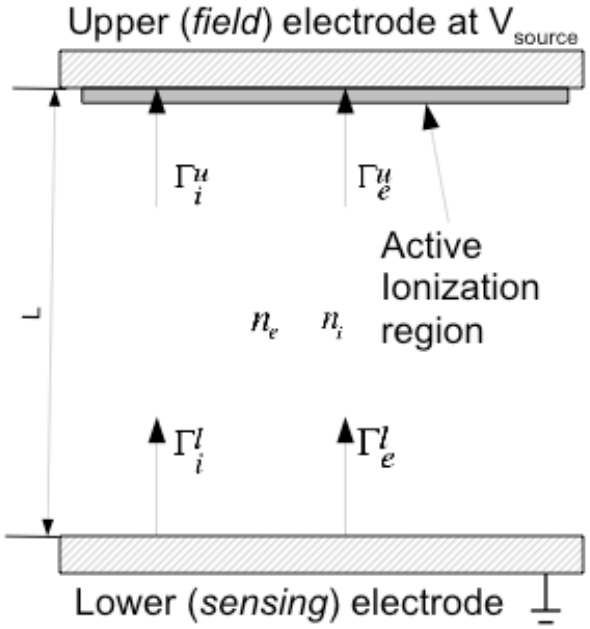


**Figure IV-31 Diagram of the electrode gap and sign conventions used by the APG model.**

The rates of change of the densities of the electrons and ions in the gap are given by

$$\frac{\partial n_e}{\partial t} = \frac{1}{L}\left(\Gamma_e^l - \Gamma_e^u\right) + \alpha\left|\mu_e E\right| n_e + \alpha_{AR}\left|\mu_e E_{AR}\right| \bar{q}_{PM} n_{PM}$$

$$\frac{\partial n_i}{\partial t} = \frac{1}{L}\left(\Gamma_i^l - \Gamma_i^u\right) + \alpha\left|\mu_e E\right| n_e + \alpha_{AR}\left|\mu_e E_{AR}\right| \bar{q}_{PM} n_{PM}$$

with $n_e$ and $n_i$ being the number densities of electrons and ions, $\Gamma_e^l$, $\Gamma_e^u$, $\Gamma_i^l$, and $\Gamma_i^u$ being the charge carrier fluxes at the upper and lower electrode surfaces of electrons and ions, respectively. The first term on the right-hand side of each equation is the drift-driven flux of electrons or ions to the electrode surfaces. The second term, $\alpha\left|\mu_e E\right| n_e$, is the drift-driven Townsend discharge term across the entire gap, where the Townsend coefficient, $\alpha$, is the number of electron-ion pairs produced per unit distance in a Townsend discharge. $\mu_e$ is the electron mobility. $E$ is the electric field defined by

$$E = a\frac{-V_{source}}{L},$$

and $a$ is a factor that accounts for the reduced mean intensity of the electric field over the inward facing surface of the electrode. The mean electric field intensity can be calculated using a line integral in QuickField. An integration through 180° around the inward facing half-circumference of the electrode for a typical sensor geometry yields $a$~0.55.

The same term appears in both equations because an ion is created with each electron. Townsend coefficients for electrons in air at atmospheric pressure are given by Parker [47] in Figure IV-32. A linear regression in T (K), TE (KV/m), and E (V/M) yields the following relation for Townsend coefficient $\alpha$, in (#/m), valid over 3.0-7.5x$10^5$ (V/m). Regression fit points are plotted over Parker's published curves in the figure.

$$\alpha = \left(2.85\times10^{-4}T + 2.2\times10^{-2}\right)E - \left(3.48\times10^{1} + 2.33\times10^{4}\right)$$

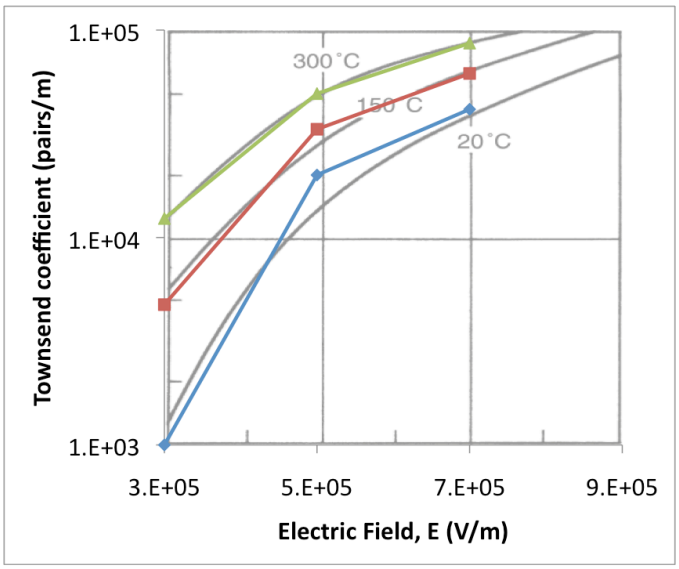


**Figure IV-32 Townsend coefficient for air versus electric field strength for different temperatures. [47]**

The third term on the right-hand side of each equation is the PM-driven Townsend discharge term due to charging of soot particles in the active region:

$$\alpha_{AR}\left|\mu_e E_{AR}\right|\bar{q}_{PM} n_{PM}$$

where the field intensity in the active region is $E_{AR}$ and the Townsend coefficient $\alpha_{AR}$ is based on that local field intensity. Due to the curvature of the electrode surfaces, the electric field intensity is concentrated at the surface by a factor $a_{AR}$, such that $E_{AR} = a_{AR}E$. Based on the QuickField modeling of the electric field in the sensor gap, the electric field in the active region is 1.05-1.2 times higher than the nominal electric field in the gap, depending on the geometry. $q_{PM}$ is the number of fundamental charges per soot particle. Based on the analysis of the previous section, I assume $q_{PM}$ =1.

The flux conditions set the lower electrode as the grounded, or sensing, electrode and the upper electrode as the source, or field, electrode. The flux boundary conditions are assigned as follows:

$$\Gamma_e^l = -\gamma_e \mu_i n_i E$$
$$\Gamma_i^l = \mu_i n_i E$$
$$\Gamma_e^u = \mu_e n_e E$$
$$\Gamma_i^u = 0$$

with electron mobility, $\mu_e = -1.13\times10^{-1}\left(\frac{m^2}{Vs}\right)$, ion mobility, $\mu_i = 1.5\times10^{-3}\left(\frac{m^2}{Vs}\right)$, and secondary electron emission coefficient, $\gamma_e$. [58]

It is useful to rewrite the system of equations after applying the boundary conditions:

$$\frac{\partial n_e}{\partial t} = n_e\left(\frac{V}{L^2}\right)\left(\alpha a L\left|\mu_e\right|\frac{|V|}{V} - \mu_e\right) - n_i\mu_i a\left(\frac{V}{L^2}\right)\gamma_e + n_{\mathrm{PM}} q_{\mathrm{PM}}\left|\mu_e\right|\left(\frac{V}{L^2}\right)\frac{|V|}{V} L a_{AR}\alpha_{AR}$$
$$\frac{\partial n_e}{\partial t} = \left(\frac{V}{L^2}\right)\left(n_e\left(\alpha a L\left|\mu_e\right|\frac{|V|}{V} - \mu_e\right) - n_i\mu_i a\gamma_e + n_{\mathrm{PM}} q_{\mathrm{PM}}\left|\mu_e\right|\frac{|V|}{V} L a_{AR}\alpha_{AR}\right)$$

and

$$\frac{\partial n_i}{\partial t} = n_e\left(\frac{V}{L^2}\right)\alpha a L|\mu_e|\frac{|V|}{V} + n_i\mu_i a\left(\frac{V}{L^2}\right) + n_{\mathrm{PM}}q_{\mathrm{PM}}|\mu_e|\left(\frac{V}{L^2}\right)\frac{|V|}{V}La_{AR}\alpha_{AR}$$

$$\frac{\partial n_i}{\partial t} = \left(\frac{V}{L^2}\right)\left(n_e\alpha a L|\mu_e|\frac{|V|}{V} + n_i\mu_i a + n_{\mathrm{PM}}q_{\mathrm{PM}}|\mu_e|\frac{|V|}{V}La_{AR}\alpha_{AR}\right)$$

At equilibrium, $\frac{\partial n_e}{\partial t} = \frac{\partial n_i}{\partial t} = 0$, thus the above relations reduce to

$$n_e\left(\alpha L|\mu_e|\frac{|V|}{V} - \mu_e\right) - n_i\mu_i\gamma_e = -n_{\mathrm{PM}}q_{\mathrm{PM}}|\mu_e|\frac{|V|}{V}L\frac{a_{AR}}{a}\alpha_{AR}$$

$$n_e\alpha L|\mu_e|\frac{|V|}{V} + n_i\mu_i = -n_{\mathrm{PM}}q_{\mathrm{PM}}|\mu_e|\frac{|V|}{V}L\frac{a_{AR}}{a}\alpha_{AR}$$

This steady-state system of equations is not well suited to a closed-form analytical solution, but it is useful to see how the electron and ion densities balance in terms of the PM-driven Townsend source term.

The original set of time-domain ordinary differential equations can be solved for the steady-state values of $n_e$ and $n_i$ in MATLAB's ode15s solver using an electrode gap of $L$=2 mm and a voltage of $V$=1000 V to simulate the conditions in the sensor. MATLAB returns the values of $n_e$ and $n_i$ over the time span calculated. Current at the sensing electrode $i_s$ can be calculated as

$$i_s = e\left(\Gamma_i^l - \Gamma_e^l\right)A_e$$

where $e$ is the fundamental charge unit of -1.6x10$^{-19}$ C, and $A_e$ is the area of the sensing electrode exposed to the discharge. For the following calculations, $A_e$ was assumed to be 2x10$^{-7}$ m$^2$, based on an electrode with a diameter of 2mm and a length of 10mm and approximately a third of the circumference exposed to the discharge.

In the first, trivial condition, I confirmed that the steady state response of the sensor with no trigger was zero current. Initial conditions were $n_i = n_e = 0$. Ion and electron density in the gap remained at zero. The densities also returned to zero after an

initial perturbation where $n_i = n_e = 10^9$. The time response to this initial perturbation is shown in Figure IV-33 below. The less-mobile ions responded with a time constant of about $10^{-5}$ s, whereas the more mobile electrons responded with a time constant on the order of $10^{-7}$ s. This response is important because it determines the fundamental minimum time response of the sensor, which, for these conditions is about 0.01 ms, limited by the ion response. The minimum response time would be longer if the small ionized particles also participate as charge carriers.

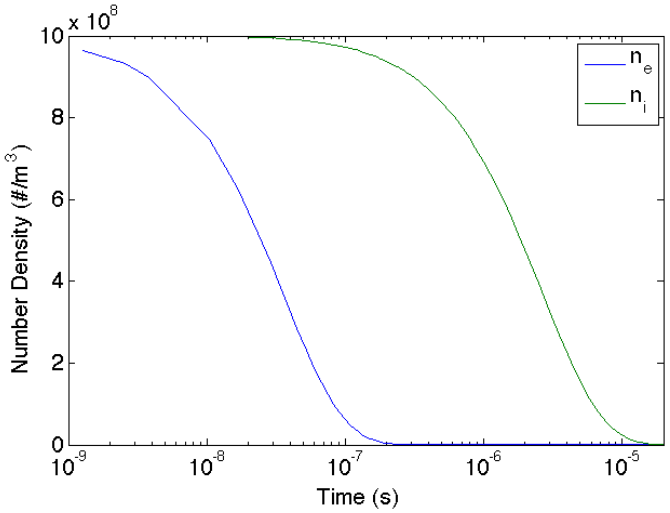


**Figure IV-33 Model prediction of ion and electron number density evolution in time in the sensor electrode gap with no particle flux to the field electrode.**

Desantes et al [25] reported soot particle number densities ranging from $2.5x10^{12}$ to $1.5x10^{13}$ (#/m$^3$) in a moderately (50%) to heavily (100%) loaded engine similar to the Cummins. For the model input, the soot particle number density, $n_{PM}$ was varied from $10^{11}$ to $1.5x10^{13}$ (#/m$^3$) to simulate number densities that might have been present during testing with PM sensors in the Cummins. The sensing electrode currents predicted by the model over that range are shown in Figure IV-34.

The operating range of the sensor was 0-15 nA, so if number densities in the Cummins were similar to those reported by Desantes [25], then the model somewhat

over-predicts the sensitivity of the sensor, by about a factor of 5. The order of magnitude, however, is correct.

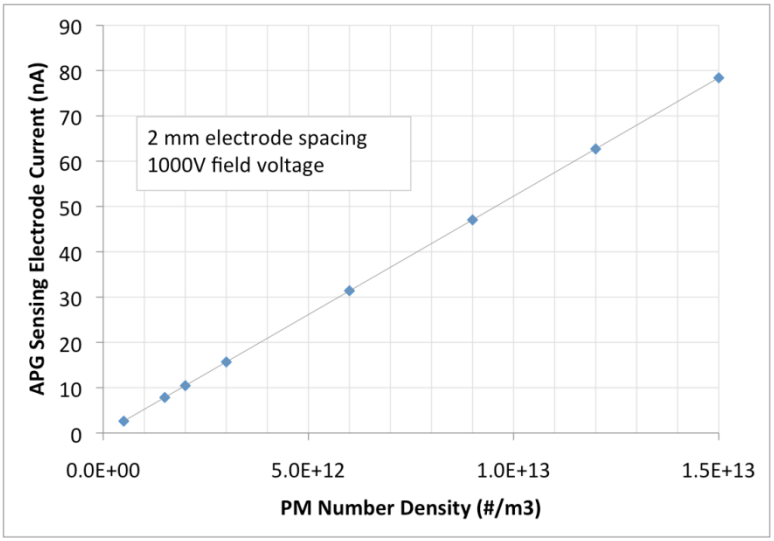


**Figure IV-34 Model prediction of sensor electrode current over a range of soot particle densities.**

Reducing the gap from 2 mm to 1 mm, reduced the rise time due to a step increase in the PM density by a factor of about 4 and increased the electrode current by 250%, as seen in Figure IV-35. In the experimental sensor design parameter study, decreasing the electrode gap had the effect of reducing the electrode current by 25%. The change in sensor current with the decrease in electrode gap represents a tradeoff between the decreased drift distance over which Townsend avalanches can propagate electron-ion pairs and the increased electric field intensity, which in turn increases the Townsend coefficient and increases the number of ion-electron pairs. The model did not take into account the effect of any modification of the flow field around the electrodes that a reduction in the gap width might have brought about. In the real sensor, a reduction in the gap width likely caused a decrease in particle flux to the active region by restricting the flow between the electrodes, resulting in a lower sensitivity.

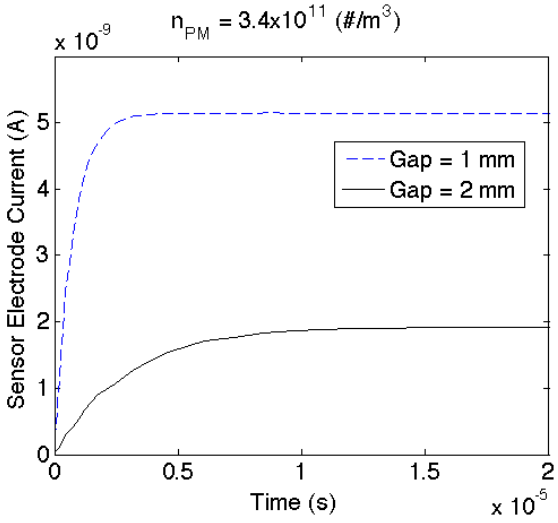


**Figure IV-35 Model prediction of the effect of decreasing the electrode gap on electrode current.**

The field electrode voltage in the model was varied to match the conditions of the test shown in Figure IV-10. The electrode gap was set to 1mm to match the geometry of the sensor in that test. Based on the electric field intensities predicted by a QuickField model of the electrodes in the sensor tested, $a_{AR}$=1.05 and $a$=*0.55* were used for the field intensity coefficients. The model was run to calculate the electrode current with values of the field electrode voltage from 600V to 1800V with soot particle number densities $6x10^{11}$, $1.2x10^{12}$, and $2.4x10^{12}$ #/m$^3$. While the actual soot particle number density for the sensor measurement was not known, it is reasonable to expect that they fell into the simulated range, based on the measurements of similar engines by Desantes [25]. The results for both model runs are shown in Figure IV-36. The results of the sensor measurements from Figure IV-10 are included in the plot for comparison. For the sensor measurements, the electrode current sensitivity to field voltage was about 0.93 nA/kV. The sensitivity of the APG model prediction of electrode current to field electrode voltage increased with soot particle number density. For each soot particle number density, the model over-predicted the sensitivity to field voltage: by a factor of about 3.7 for the lowest concentration and by a factor of 15 for the highest concentration.

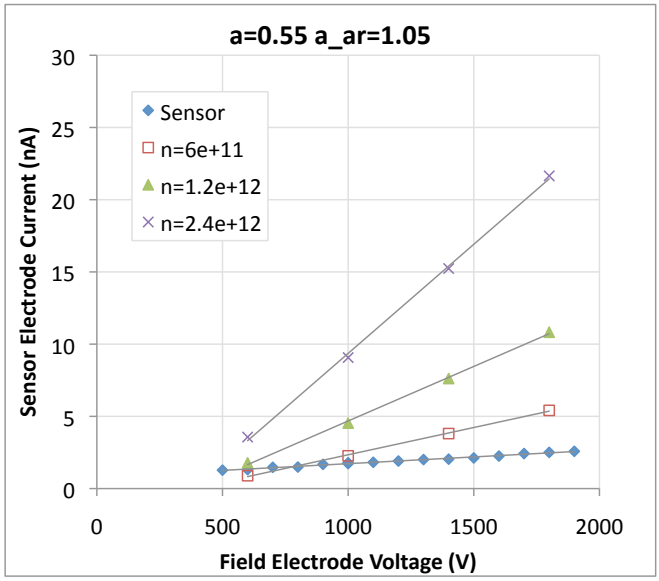


**Figure IV-36 Model prediction of electrode current as a function of source voltage compared to physical results from a sensor with electric field concentration factors based on QuickField results.**

The model was run with the same conditions except that $a_{AR}$ and $a$ were both set to 1.0 to remove the effect of different field strengths for the different Townsend mechanisms. The results are shown in Figure IV-37. The over-prediction of voltage sensitivity of the model field electrode voltage was reduced. For the lowest soot particle density, the predicted sensitivity to field voltage was too high by a factor of 2.2, and for the highest number density by a factor of 8.7.

This suggests that the field concentration factors $a$ and $a_{AR}$ account for more than just the variations in the electric field strength at the electrode surface. Rather, they serve as empirical coefficients which weight the relative effects of the drift-driven and PM-driven Townsend sources terms in the governing equations due to differences in diffusion distance for the two process and the field concentration around the individual particles as well as the variations in electric field strength due to electrode geometry.

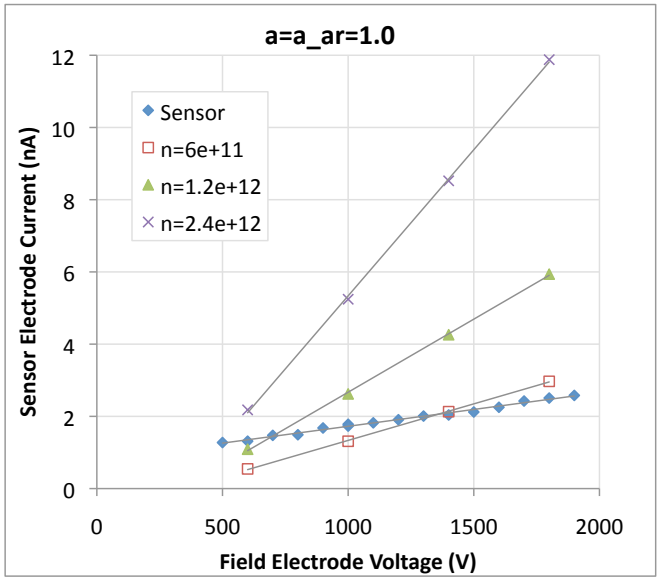


**Figure IV-37 Model prediction of electrode current versus field voltage with no consideration of field concentration.**

To see the effect of the reversing the relative weights of the two terms, the model was run with $a_{AR}$=0.55 and *a=1.05* at the same soot particle number densities. The results are shown in Figure IV-38.

The electrode currents predicted in this case are all about an order of magnitude lower than those predicted in the original case with $a$ and $a_{AR}$ based on the QuickField results. In the lowest soot number density case, the sensitivity of the model to field voltage is actually lower than observed in the sensor, by a factor of about 0.6. For the middle and high number density cases, the factors are 1.2 and 2.4, respectively. Now, however, the electrode currents are lower than observed in the sensor. This is an indication that perhaps an additional physical process is required to explain the sensor operation with respect to the field voltage level. Some suggestions for improving the model to reflect this are made in the "Future Work" section of Chapter V.

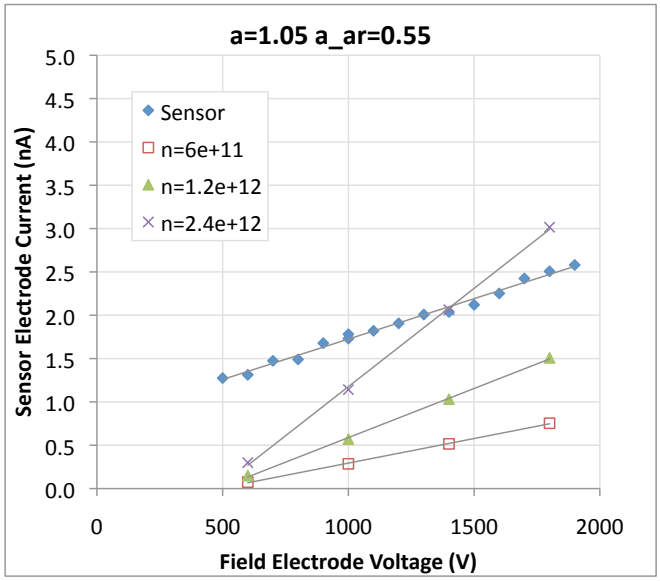


**Figure IV-38 Model prediction of electrode current versus field voltage with $a > a_{AR}$.**

Finally, we can use the model to predict the impact of exhaust gas temperature on the sensor sensitivity. Recall that temperature differences in the exhaust pipe were generally less than 100K between the upstream and downstream sensor locations, but that sensitivity decreased by 50-85% between the upstream and downstream locations. Also recall that during warm-up, the sensor signal increased by about 20% from the cold-start to the steady-state condition.

In Figure IV-39, the model-predicted sensor current is plotted against gas temperature over the range of 300-1000K. PM number densities of $8 \times 10^{11}$ and $10 \times 10^{11}$ particles per $m^3$ were used. The effect of temperature is highest at the lowest temperatures, where a 100K increase corresponds to an increase in electrode current of about 0.3 nA. In the $n_{PM}=10 \times 10^{11}$ (#/$m^3$) case, this corresponds to an increase in electrode current of about 6%. Assuming Parker's relation for the Townsend coefficient in air is appropriate for exhaust gas, the change in Townsend coefficient is insufficient to explain all of the thermal effect seen in the temperature. Since warm-up increases the sensor signal by 20% or more, most of the increase in sensor signal must be due to changes in

the engine emissions. Engine warm-up is not well suited to gravimetric measurement of soot concentration which requires 15 minutes or more of steady-state operation. Therefore it is difficult to know what changes in the soot concentration accompany engine warm-up.

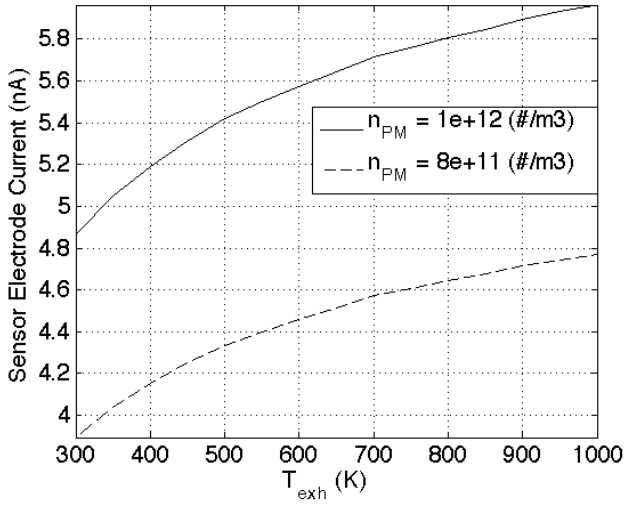


**Figure IV-39 Effect of exhaust gas temperature on model-predicted electrode current.**

The thermal effect can only explain part of the decrease in sensor sensitivity between the upstream and downstream locations. As seen above, the thermal effect can only account for less than 6% of the decrease in signal, whereas the actual decrease in sensor signal was from 50% to 85%. This suggests that the signal decrease downstream is due primarily to reduction in particle number through agglomeration.

The predictions were remarkable in their correspondence with observed data. The model accurately reproduced the behavior of the sensor in terms of observed electrode currents with respect to particle number flux, and field voltage. The observed trend with sensor gap was not reproduced in the model, probably due to the decreased particle flux to the active region because of restricted flow in the electrode gap.

# Chapter V: Summary and Conclusions

This chapter contains a summary of the major findings and a conclusions section discussing applications for the sensor, relevance and accuracy of the sensor model, and suggestions for future work.

## SUMMARY OF FINDINGS

In this work, I characterized the behavior of an electronic particulate matter sensor in more detail and over a broader range of operating environments than had been done previously. The operating characteristics of the sensor were almost entirely different in the exhaust of the Cummins engine compared to the Yanmar, with which most of the previous development and experimentation was done. Based on the newly observed behavior, a new understanding of the physical mechanism was developed, and a predictive mathematical model was developed and compared against actual sensor performance.

In the Yanmar exhaust, the sensor signal was linear with the mass concentration of soot. This relationship broke down in the Cummins due to the substantial differences in soot morphology for different operating conditions. The sensor was found to be much more sensitive to soot in the Cummins (by two to three orders of magnitude) than in the Yanmar; this is thought to be an effect of particle morphology and number density.

Previously, the natural charge content of Yanmar exhaust had not been well documented, and its impact on sensor performance was distinguished from the mechanism based on particle charging by the sensor. In this work, I showed the dominance in the sensor signal of naturally charged soot during the first part of a tip-in and how the natural-charge contribution decreases downstream. Natural charge was not found to contribute significantly to sensor operation in the Cummins.

The sensor was successfully used to detect a simulated leak in the DPF installed on the Cummins. The sensor had sufficient signal-to-noise ratio over a wide range of

operating conditions and still performed adequately even in the worst-case condition of idling at low speed. Failure detection confidence increased with increasing engine load. At idle, the signal to noise ratio was 36:1, and the sensor was able to detect a leak of 0.7 $mg/m^3$, or 10 mg/bhp-hr. At 1800 RPM and 40% load, the signal to noise ratio was 220:1, and the sensor was sensitive to leaks of 0.005 $mg/m^3$, or 0.003 mg/bhp-hr.

In the Yanmar, sensor orientation did not have a major impact on the sensor output, but exhaust gas velocity was shown to have a strong impact on sensitivity. In the Cummins, the sensor orientation had a major impact on sensitivity, and exhaust gas velocity could not be conclusively shown to have an impact. This relative insensitivity to of the sensor signal to flow velocity is consistent with the model that was developed where an increase in particle flux with increasing velocity is offset by decreased level of charge achieved due to the lower residence time in the sensor at higher velocity.

Based on the response to sensor orientation and on theoretical particle migration velocities, a new understanding of the mechanism of operation on electrically neutral soot particles was developed. It was shown that the portion of the field electrode surface facing the sensing electrode was the critical area for exposure to exhaust gas. Based on the migration velocities of the particles, molecular ions, and electrons, it was shown that the particles themselves must not be the dominant charge carriers in the sensor. Rather, the particles trigger a non-self-sustaining Townsend discharge in which electron-ion pairs are responsible for the transport of charge across the electrode gap. Because particles likely only become singly charged, the sensor is therefore sensitive primarily to the number density of particles and the ability of those particles to initiate a Townsend discharge.

Experimental evidence based on sensor response, gravimetric measurements, and TEM imaging of particle samples suggest that, for the Cummins engine, when operated at various conditions, higher PM mass emissions were associated with increased PM size. This is also consistent with the literature [1,25]. Consequently, the number density of soot

tends to vary inversely with the overall mass of soot present, thus, the sensor showed an inverse correlation to soot mass concentration. For example, the observed decrease in sensitivity of the sensor at higher EGR levels, the increase in total mass emissions, and the increase in soot particle size observed with a TEM support this physical understanding of the sensor.

A mathematical model was developed to explain and quantify the performance of the sensor. The model was implemented in MATLAB and used to replicate the steady-state performance of the sensor. The model correctly matched the order of magnitude of but over-predicted the electrode currents observed in the sensor by a factor of about 5. It matched the order of magnitude of the signal current, but over-predicted the sensitivity to field electrode voltage by factors as high as 15 depending on the relative weighting of the drift-driven and PM-driven Townsend terms in the governing equations. The model predicted a 250% increase in the sensor sensitivity with a change in electrode gap from 2mm to 1mm, but in a real sensor, the sensitivity decreased by 25%. According to the thermal sensitivity of the Townsend coefficient used in the model, the maximum thermal sensitivity was 0.3 nA/100K at 300K and decreased with increasing temperature: the effect of a 100K increase exhaust gas temperature from 300K corresponded to a 6% increase in sensor electrode current.

## CONCLUSIONS

Work on the sensor has led to a number of insights into its applications and physical mechanisms. In this section I discuss the potential applications of the sensor as well as the strengths and weaknesses of the model used to describe its operation. Finally, I make some recommendations for future work.

### Applications

In its current state of development and calibration, the PM sensor is suitable for use in the OBD function for particulate filters in real engines. This was demonstrated

under steady-state conditions by simulating the failure of a DPF by allowing part or all of the exhaust to bypass the DPF and measuring changes in the sensor signal downstream. Because the sensitivity of the sensor is dependent on particle morphology, which changes with engine operating conditions, operation of the sensor in an OBD function would be dependent on knowing what the expected signals would be at the DPF inlet and outlet at a given operating condition. Then, a sensor installed downstream of the DPF would detect DPF failure based on the signal exceeding a level determined by the instantaneous engine operating conditions. If development of a lookup table for OBD was not possible or not desirable, a second sensor installed upstream of the DPF would provide a reliable reference against which to gauge the effectiveness of the DPF. In addition, for commercial use, long-term testing for signal stability is required, and it will be necessary to confirm whether the DPF regeneration cycle is sufficient to remove soot from the sensor electrode surfaces.

Initial hopes for the sensor included use as an analytical tool for determining the mass concentration of soot in diesel engine exhaust. Unfortunately, work with the Cummins engine, due to its changing particle morphology, showed that, at least in its current form, the PM sensor is not well suited to that task since it is primarily sensitive to particle number density. Perhaps with further development, other electrode geometries may be implemented to reduce the particle size dependency. With an extensive measurement campaign covering a comprehensive range of fueling rate and injections per cycle, engine speed, EGR rate, and boost pressure, a transfer function for PM mass based on sensor output could be developed. However, this would be closely coupled to the engine's emissions performance, which may evolve over time. Perhaps the analytical function of the sensor lies in the future with regulation of PM number density or with control of engine combustion based on knowledge of the number density of soot.

The sensor proved to be much more durable in the Cummins than in the Yanmar due to the decrease in PM mass concentration and decrease in particle size. Sensors were operated for 10's of hours without fouling problems, although there was some evidence

of increased fouling when the EGR rate was high and PM levels were elevated. Sensors installed downstream of the DPF are not expected to have problems with soot fouling due to the low PM concentrations and the periodic regeneration of the DPF, which may have a cleaning effect on the sensor, too. Nevertheless, without long-term testing, it cannot be said for certain what the durability of a sensor would be in that location.

**Modeling**

In spite of its simplicity, the proposed physical model explained the observed behavior of the sensor with first-order accuracy in terms of its response to naturally charged and neutral particles, its orientation in the flow, the velocity of the exhaust gas, and the various parameters which affect the particle morphology. With increasing engine load, the sensor sensitivity increased due to increased number density. Sensor sensitivity went down with EGR rate in spite of the increased PM mass concentration due to the decrease in particle number density. Sensor sensitivity was decreased downstream in the exhaust pipe due to the decrease in number density of the particles since increased residence time in the exhaust pipe allowed more time for agglomeration.

The model complements and updates the one proposed by Warey [43]. Significant differences from that model include the concept of two sources of charge (natural and locally induced); the mechanism of charging particles in an active region of the field electrode, and the transport of charge by ions and electrons rather than the particles themselves.

In his dissertation [43], Warey listed several gaps in the understanding of the model:

"The sensitivity of the sensor signal to the bulk flow velocity is not clearly understood." [p.102] I believe this has adequately been explained as an effect of the flux of particles in the exhaust with naturally charged particles. Evidence was shown and a physical explanation was given for the insensitivity of the sensor to exhaust gas velocity,

at least over the range tested, for electrically neutral particles, as demonstrated in the exhaust of the Cummins engine.

Warey pointed out a non-linearity in the scaling of the sensor signal (normalized conductance) with soot concentration. I have shown the sensor to be sensitive primarily to the number density of particles in the discharge mode, and to be affected by the size distribution of particles in the natural charge mode due to the decrease in charge-to-mass ratio with increasing particle size. The non-linearity of the sensor sensitivity to mass concentration of soot was greatly compounded in the Cummins engine, where I observed drastic changes in the soot morphology at different operating conditions.

Warey also suspected a significant effect of "2-dimensionality of the diffusion effects". In this work, I showed some 2-dimensionality through the effect of the orientation of the sensor in the flow. This was not significant in the Yanmar exhaust, but the different conditions in the Cummins engine revealed the importance of sensor orientation. Masking of the field electrode by the upstream electrode caused a decrease in the sensor sensitivity, but masking of the sensing electrode by the field electrode did not. As the angle of incidence of the exhaust gas onto the field electrode increased, the signal decreased with the cosine of the incidence angle. Thus some level of 2-dimensional effects were shown. The discharge model, however, was based entirely on ion and electron drift and gave acceptable results with a model of essentially 0-dimension.

Finally, Warey lamented the presence of many empirical powers to collapse variables. Unfortunately, without adequate equipment for establishing particle size and charge distributions, it was not possible to form analytical expressions useful for predicting the observed sensor responses in this study. However, an analytical framework was laid to support such work in the future.

Several of the assumptions of the discharge model bear challenging in future work. For example, it is possible that a more complete picture of charging of particles

including diffusion effects could improve the accuracy. Also, the model would be sensitive to errors in the value of the Townsend coefficient, which is essentially empirically determined. I used a correlation for determining Townsend coefficient based on exhaust gas temperature and electric field strength developed for ESP's, and the potential differences between the flows treated by ESP's and those in diesel exhaust pipes may be significant.

The behavior of the model with respect to field voltage is not entirely satisfactory. The inability to match the observed slope and intercept of curve for electrode current with respect to field voltage indicates that perhaps some fundamental physical mechanism is still missing from the model. When the soot particle density in the model was set so that the model electrode current matched the observed electrode current, the sensitivity to field voltage was too high, but when the field concentration factors were adjusted to match the voltage sensitivity, the electrode currents were too low. One possible physical effect which could be incorporated into the model would be the interaction of soot particles with the ions and electrons in the electrode gap. The net effect of this would be to decrease the electron and ion densities in the gap as the soot particles "sponged them up." This would have the effect of decreasing the predicted electrode currents. It is possible that not including this effect in the discharge model is responsible for the consistently high predictions of electrode current and the high sensitivity to field voltage.

Also, the assumption of single charging in the context of the insensitivity to flow velocity bears further investigation. Without the ability to directly measure particle sizes at a given engine operating condition, it was not possible to say conclusively that the particle morphology for the conditions over which the sensitivity to exhaust gas velocity was determined were truly the same. I assumed that at a given fueling rate, the particle sizes would be constant, but ultimately, this was a guess. It is possible that the insensitivity observed was coincidental. In addition, the physical explanation for insensitivity to flow did not consider any local flow patterns, and the presence of a shroud

around the electrodes doubtless modifies the flow in complex ways. Suggestions for model improvements can be found in the next section.

**Suggestion for Future Work**

Quantitative prediction of sensor sensitivity in this work was hampered by a lack of size distribution data for particles in the flows measured. Thus, much of the understanding was developed through qualitative observations and inferences of the physical mechanisms using logical arguments. While the OBD function can be adequately satisfied by the current level of understanding of the sensor, in order for it to be useful as an analytical tool in its own right or for feedback in control of combustion in a production engine, it will be necessary to understand the detailed relationship of the sensor sensitivity to particle size.

Unfortunately, I stumbled upon the effects of size distribution on sensor sensitivity late in the research program and it was not possible to acquire the proper particle sizing equipment or to arrange for testing of the sensor at a facility where such equipment is available. Of particular use would be a combination of electrical mobility analyzer and condensation nuclei counter. It would also be useful to have a source of particles of controllable size distribution. Using this combination of tools, it would be possible to record the output of the sensor for exhaust flows with a mono-disperse distribution of soot particle sizes and establish calibration curves relating sensor output to number density for a range of particle sizes. It will likely be the case that the peak sensitivity of the sensor can be tuned to various particle sizes by altering the geometry of the electrodes and the strength and shape of the electric field. This could allow sensors optimized for different functions.

For instance, if a sensor was to be used as a feedback tool for combustion control and was to be placed upstream of a turbocharger, it would be expected to see mostly accumulation mode particles that had not experienced much agglomeration. A high sensitivity to small particles would be appropriate. For a sensor designed to estimate the

incoming flux of soot to a DPF, sensitivity to highly agglomerated particles would be called for. If regulations are developed limiting the number density of particles downstream of a DPF, design sensitivity to nanometer-scale particles is in order.

Another fruitful avenue of future work has already been suggested by Warey in his dissertation. Work in this research program adds context and some specific goals to his recommendation to develop a finite-element multi-physics model to study the flow patterns around the sensors. In particular, the sensitivity to orientation and the masking of the field electrode by an upstream sensing electrode raise interesting questions about the nature of the turbulent wake behind the upstream electrode. It seems desirable to develop an electrode geometry which is not sensitive to orientation in the flow since this would eliminate the need to control orientation of the sensor during installation. This is of particular importance for the sensor if it is to be marketed as original equipment in future engine emission control systems.

A more detailed, higher resolution electric field calculation would reveal the electric field concentration around a particle. The student version of QuickField 5.6 did not have sufficient resolution to capture the local concentrations around a soot particle. In order to have field emission of an electron, electric field intensities of around $10^8$ V/m are necessary, and a higher-resolution model of a soot particle would reveal the concentrations resulting from the branched structure of an accumulation mode soot particle.

Finally, the size and shape of the active region at the electrode surface could be more thoroughly investigated by preparing a series of sensors where the electrode was painted onto the ceramic substrate in stripes of various widths. Insight would be gained by measuring the orientation effects and the sensitivity to field voltage strength.

# APPENDIX A – FLOW CALCULATIONS

## REYNOLDS NUMBER FOR THE ELECTRODES

The nature of the flow field in the vicinity of the electrodes can be determined through a calculation of the Reynolds Number. The diameters of the electrodes in the latest sensors tested was 2mm. Exhaust gas velocity for the sensor orientation study was 30 m/s, and as above, the exhaust temperatures fell in the range from 100 – 400 °C, yielding kinematic viscosities in the range 26-68x$10^{-6}$ $m^2$/s. Thus Reynolds numbers fell in the range 700-2300, and the flow field around the cylinders would in general be characterized by a turbulent wake.

**KNUDSEN NUMBER**

We calculate the Knudsen number as the ratio of the mean free path $\lambda$ to the transport dimension of interest, in this case, the electrode gap width, $L$:

$$\mathrm{Kn} = \frac{\lambda}{L}$$

From the kinetic theory of gases, the mean free path for particles of different sizes can be calculated as

$$\lambda_a = \frac{g_{a-b}}{\nu_{a-b}}$$

where $g_{a\text{-}b}$ the reduced thermal (collision) speed is given by

$$g_{a-b} = \sqrt{\frac{8k_BT}{\pi m_{a-b}}}$$

where $k_B$ is the Stefan-Boltzmann constant, and $T$ is the gas temperature. The reduced (collision) mass $m_{a\text{-}b}$ can be calculated by

$$m_{a-b} = \frac{m_a m_b}{m_a + m_b}.$$

$\nu_{a-b}$, the collision frequency is given by

$$\nu_{a-b} = n_b g \left(\frac{D_{PM}}{2}\right)^2 \frac{\pi}{4}$$

assuming that the collision cross section is dominated by the diameter of the particles, $D_{PM}$. Here the collision speed $g$ is dominated by the mean velocity of the air molecules and can be calculated based on the mean molecular mass of the air:

$$g = \sqrt{\frac{8k_BT}{\pi m_{PM}}}$$

Combined, the above expressions yield the Knudsen number:

$$Kn = \left( \frac{m_{air} + m_{PM}}{m_{PM}} \right) \frac{16}{n_{air} L D^2 \pi} \approx \frac{16}{n_{air} L D^2 \pi}$$

The number density of air, $n_{air}$, can be found via the ideal gas equation:

$$n = \frac{P}{k_B T} = \frac{101300(Pa)}{1.38 \times 10^{-23} \left( J/K \right) 700(K)} = 1.05 \times 10^{25} \left( m^{-3} \right)$$

If we use an electrode air gap of 1 mm, we can calculate the Knudsen number. For the smallest particles, $D_{PM}=1x10^{-9}$ m.

$$Kn = \frac{16}{1.05 \times 10^{20} \left( m^{-3} \right) \cdot 1 \times 10^{-3} (m) \cdot \left( 1 \times 10^{-9} (m) \right)^2 \pi} \approx 4.9 \times 10^{-4} \ll 1$$

Collisions, therefore, are dominant, and we can make a continuum approximation.

**REYNOLDS NUMBER FOR INDIVIDUAL PARTICLES.**

The mean aerodynamic diameter of the particles falls in the range from 1 nm to about 10 $\mu$m. The exhaust gas velocities typically fall in the range from 3-100 m/s, with the large discrepancy due to pulsations during an engine tip-in. Exhaust temperatures fall in the range from 100 – 400 °C, depending on engine load and speed, yielding kinematic viscosities in the range 26-68x$10^{-6}$ $m^2/s$. Calculation of the Reynolds number,

$$\mathrm{Re} = \frac{uD}{\nu}$$

yields a range of 4x$10^{-5}$ to 40. Even at the highest Reynolds numbers, the motion of the particles is in the Stokes flow regime, and viscous forces dominate. The drag force on the particles can be given by

$$F_D = 3\pi\mu uD$$

When considering the motion of an individual particle, we can assume that viscous forces dominate inertial, and that a particle moves at its terminal velocity in an electric field.

# APPENDIX B – DISCHARGE MODEL CODE

File – "TownsendPlasma.m" run with MATLAB solver *ode15s*

```
function dy = TownsendPlasma(t,y)
%This differential equation system is published in Shin & Raja
%"Dynamics of Pulse Phenomena in He Dielectric Barrier Atmosperic
%Pressure Glow Discharges."
%Use ode15s to solve:
%y0 = [0 0 0 0];        %initial condition for ne ni ch_l ch_u
%span = [0 5e-5];       %time span for the calculation
%[t,y]=ode15s(@TownsendPlasma,span,y0);
%eletrode current = polyfit(t,y(:,4),1);

%Constants
kB = 1.38e-23;          %J/K - The Stefan-Boltzmann constant
e_charge = -1.602e-19;  %C - electron unit charge

%Parameters
L = 0.001;              %m - the gap between the electrodes
Ae = 2e-7;              %m2 - the electrode area
a = 1.51;               %field concentration factor from Quickfield 2D
Vsource = 1000;         %V - the potential difference across the
                        %electrodes

gamma_i = 0.01;         %secondary emission coefficient
mu_e = -1.13e-1;        %m2/Vs - electron mobility
mu_i = 1.5e-3;          %m2/Vs - ion mobility

q_PM = 1;               %# fundamental charges per PM particle
n_PM = 2.4e+11;         %#/m3 of incoming particles

%Calculated Parameters
E = -Vsource/L;         %V/m - electric field strength
E_ar = abs(E*a);        %local concentration of electric field in
                        %the active region

M_a = +2.85e-4*Tg + 2.20e-2;
B_a = -3.48e+1*Tg - 2.33e+4;

alpha = M_a*E + B_a;          %1/m - Relation from Parker ESP book
alpha_ar = M_a*E_ar +B_a;
```

```
%Differential equations
n_e = y(1);                    %number density of electrons
n_i = y(2);                    %number density of ions

%Upper (field) Electrode
Gamma_e_u = E*mu_e*n_e;        %V/m * m2/Vs * #/m3 = #/m2s
Gamma_i_u = 0;

%Lower (sensing) Electrode
Gamma_e_l = -gamma_i*mu_i*n_i*E;
Gamma_i_l = mu_i*n_i*E;

dy = zeros(4,1);

dy(1) = (1/L)*(Gamma_e_l - Gamma_e_u) + alpha*abs(mu_e*E)*n_e + ...
            alpha_ar*abs(mu_e*E_ar)*q_PM*n_PM;
dy(2) = (1/L)*(Gamma_i_l - Gamma_i_u) + alpha*abs(mu_e*E)*n_e + ...
            alpha_ar*abs(mu_e*E_ar)*q_PM*n_PM;

%lower electrode charge flux
dy(3) = e_charge*(Gamma_i_l - Gamma_e_l)*Ae;
%upper electrode charge flux
dy(4) = e_charge*(Gamma_e_u - Gamma_i_u)*Ae;

% dne1 = n_e * (mu_e*E/L + k_i*N);
% dne2 = n_i * -gamma_i*mu_i*E/L;
%
% dni1 = n_e * k_i*N;
% dni2 = n_i * -mu_i*E/L;
%
% dnedt = n_e * (mu_e*E/L + k_i*N) + n_i * -gamma_i*mu_i*E/L;
% dnidt = n_e * k_i*N + n_i * -mu_i*E/L;
```

# APPENDIX C – GUIDE TO CALTERM III AND THE CUMMINS ENGINE

Access to the internal operational parameters of the Cummins engine is gained through the use of Calterm III, a Cummins developed software package. The University of Texas at Austin has been given a version which allows a limited level of access to the internal operating parameters. Some level of engine control is allowed, and monitoring of many parameters is available.

### STARTUP PROCEDURE

On starting up Calterm, the user is presented with a "Module Selection" screen in which a configuration (*.ecfg) file is selected. The "Automatic" button should be sufficient to choose an appropriate file (last one successfully used). Most of the work in this dissertation was done using `C:\Program Files\CaltermIII\BAD\PG_PU_v2.ecfg`. (BAD refers to the engine product code and is not a reflection of the file quality.)

After selection of the configuration file, Calterm III will attempt to connect to the engine. If the datalink adapter is not plugged in or if the engine ECU power is not on ("Ignition" switch on the Superflow dyno console. The console power must be on for this to work), the user will be warned that the connection was not successful. Switch on the power and retry. After a successful connection, the user will be warned that the product code in the configuration file does not match the product code in the engine firmware. This problem does not have any practical significance for engine operation and can be dismissed without consequence.

After a short while, the screens populate with the selected variables and begin live updating. At this point, the on-screen display reflects the current engine conditions.

### SELECTION OF PARAMETERS TO MONITOR

The user interface screen displays the currently selected parameters. The screen is always split into two columns, with no apparent way to change to a single column. The data logging function records the operating parameters displayed on a screen so that all of the parameters on a screen are written to the same file. Different groups of parameters may be arranged by adding more screens. Data logging for each screen is independently controlled. The user may switch between the screens by clicking tabs at the top of the screen.

To add parameters, click in the blank line at the top of a screen and hit the F1 button to search for parameter names. A few helpful hints for finding parameters:

- Typing in the "Query String" field takes the user to the place in the current list of variables that matches the start of the query string.

- Pressing the "Query" button after typing in the "Query String" field limits the list of variables to those that match the query string. This function is not restricted to matching the first letters of the variable name. Thus it is useful for finding a DPF parameter whose name may start with something other than DPF. For instance, V_ATM_pr_DELTA will not be discovered by only typing "DPF" in the "Query String" field but will be found when the button is pressed.

- Each variable has a "Comments" field which is generally helpful for understanding the purpose of the variable.

- Many of the variable names include prefixes to indicate their function in engine control. For instance, C_ indicates a user-adjustable control, and T_ indicates a control toggle. EMO_ indicates a function related to

emissions management. There are many other prefixes whose meaning were not revealed by Cummins during the research program, although contact with the technical support team was generally fruitful in discovering useful variable names and their functions.

- Many variables display the same information under different names. For example, both "V_ATP_tr_DOC_In" and "_Catalyst_Inlet_Temperature" give the same value, but one is in K and the other in °C.

- Variables with names starting with an underscore will not be logged.

**DATA LOGGING**

There are two data logging features available, an on-board internal data logger (IDL) in which the data is stored in ECM memory, and the normal PC-based data logger. The IDL data-logger was not used in this research. The normal data logger is initiated by pressing the "Start" button that has a red circle. (The "Start" button with the green triangle starts the data monitoring function.) From that time, the engine parameters displayed on the current screen are recorded roughly two times per second. While logging is underway, the button label changes to "Stop", and the image changes to two vertical bars. Logging is controlled separately for each screen, so that different sets of variable may be logged over independent time periods.

Logging is terminated by pressing the button now labeled "Stop". When the "Stop" button is pressed, a "Save as…" screen appears prompting the user to specify a location to write the file.

The saved file is in comma-separated variable format. The first 7 rows contain header information about the program version, and date of file generation. Rows 8-10 are the column headers, with variable name on row 8, units name on row 9, and source address on row 10. The source address refers to the address of the engine ECU and is

only relevant if multiple engines or devices are being tested at the same time. In our setup, the source address is invariably 0x00 any may safely be ignored.

In subsequent rows, the data is written in rows. The first column is always a timestamp with millisecond precision. On import to MS Excel, the precision is reduced (frustratingly) to 0.1 s. Some of the important and useful variable names are listed in the table below along with the units and any relevant comments about the variable.

**Table 3 - Important Calterm Data Logging Variables**

| Parameter Name | Units | Comments |
|---|---|---|
| DLA Timestamp | hhh:mm:ss.sss | represents elapsed time since ECU power-on |
| Compressor_Inlet_Tmptr | Deg_C | Should be the same as ambient room temp |
| EGR_Orifice_Tmptr | Deg_C | Should be the same as coolant temp |
| Final_Timing | deg_BTDC | |
| Coolant_Temperature | Deg_C | Thermostatically held at 90°C. Should not exceed 92°C at risk of boilover. |
| Battery_Voltage | V | |
| Engine_Speed | RPM | |
| Fuel_Delivery_Rate_Per_Min | kg/min | |
| Total_Fueling | mg/cyl/cycle | Listed by Calterm as "mg/stroke" |
| Charge_Flow | kg/min | Mass flow rate of air into the cylinders |
| Net_Brake_Torque | N_m | Estimated. Overpredicts dyno measurement |
| Fresh_Air_Flow | kg/min | Charge Flow – EGR flow |
| Boost_Pressure | kPa_G | |
| Intake_Manifold_Temperature | Deg_C | Lower this by turning on intercooler fans |
| EGR_Flow | kg/min | |
| EGR_Position | % | |
| EGR_Delta_Press | kPa | |
| Filtered_Turbo_Speed | KRPM | |
| EGR_Fraction | None | EGR flow/Charge Flow |
| VGT_Position | % | Variable Geometry Turbine inlet blad position |
| Very_Late_Post_Fueling | mg/cyl/cycle | 0 except when regenerating the DPF |
| PME_SootRate | g/hr | On-board (rough) estimate of |

| | | |
|---|---|---|
| | | the rate of soot deposition in the DPF |
| V_ATP_pr_DPF_Delta | kPa | Pressure drop across the DPF. See "Cummins Engine" binder for loading curve. |
| V_SFP_mg_Soot_Load_Comb | gm | On-board estimate of the DPF soot loading. ECU will request a regen when this exceeds 100 gm. |
| V_ATP_tr_DOC_Out | Deg_K | DOC outlet temp. = DPF inlet temp. During regen this can be 150K higher than DOC inlet temp. |
| V_ATP_tr_DOC_In | Deg_K | DOC inlet temp. should be close to exh gas temp measured by upstream thermocouple. |
| V_ATP_tr_DPF_Out | Deg_K | DPF outlet temp. reaches 900-1000K during regen |
| Exhaust_Tmptr | Deg_C | Exhaust gas temperature in the exhaust manifold upstream of the turbocharger. A good indicator of engine thermal state and warmup condition. |
| Ambient_Air_Press | kPa | |
| Ambient_Air_Tmptr | Deg_C | |
| Accelerator_Pedal_Position | % | This is controlled by a potentiometer in the Superflow Dyno control panel. There is a deadband through about 15%, above which the engine will rise above idle. In the current configuration this sets the desired engine speed. In-vehicle, this typically indicates desired torque level. |
| _Instantaneous_Percent_Load | % | Based on the nominal (ECU limited) max load of 350bhp. |
| T_EMO_State_User_Override | None | If 1, then user controls emission control variables. If 0, then ECU has control |
| T_CBL_EGR_Frac_User_Override | None | If 1, then user sets EGR fraction. If 0, then ECU control EGR fraction |
| C_CBL_EGR_Frac_Override_Value | None | If T_CBL_EGR_Frac_User_Override=1, then ECU sets the EGR fraction to this value. |

### DPF REGENERATION

The DPF can be manually regenerated using what is called a stationary regen. Details of the operation are listed in the binder titled “Cummins Engine.” Steps are

- Make sure the fuel tank is full
- Set “Out of Gear” state variable to 1
- Set the soot load estimate to a value > 100 gm
- Warm up the engine and exhaust by running at high load/speed until DPF outlet temp is > 725K
- When engine sound changes and the very late injections start, close the torque control valve. Engine speed will reduce to 1000 RPM.
- The regeneration will proceed through multiple (6?) stages, each at higher DPF outlet temperature, until the soot load estimate is down to 20mg, at which time the regen will stop.
- Complete regen cycle lasts approximately 40 min.

# REFERENCES


1 Eastwood, P.; Particulate Emissions from Vehicles, John Wiley & Sons, Ltd., *SAE International*, Warrendale, PA, 2008

2 U.S. Environmental Protection Agency (EPA). (2002) "Health assessment document for diesel engine exhaust." Prepared by the National Center for Environmental Assessment, Washington, DC, for the Office of Transportation and Air Quality; EPA/600/8-90/057F. Available from: National Technical Information Service, Springfield, VA; PB2002-107661, and <http://www.epa.gov/ncea>

3 Shindell, D., and Faluvegi, G., "Climate response to regional radiative forcing during the twentieth century," *Nature Geoscience*, Vol. 2 No. 4 pp 294-300, 2009

4 U.S EPA, Code of Federal Regulations, Title 40, Section 86, "Control of Emissions from New and In-use Highway Vehicles and Engines", July 2008 revision.

5 Johnson, Timothy V., "Diesel Emission Control in Review," SAE Paper 2009-01-0121, *SAE International*, 2009

6 Heywood, J.; Internal Combustion Engine Fundamentals, McGraw-Hill Book Company, New York, 1988

7 Jung, H.; and Kittelson, D., "Measurement of Electrical Charge on Diesel Particles," *Aerosol Science & Technology*, Vol. 39 No. 12, pp 1129-35, Academic Search Complete, 2005

8 Kittelson, D., "Engines and nanoparticles: a review," *Journal of Aerosol Science*, Vol. 29, No. 5/6, pp. 575-588, Elsevier, 1998

9 Lanni, T, "Fine urban and precursor emissions control for diesel urban transit buses," *Environmental Pollution*, Vol 123, No 3, pp427-437, Elsevier, 2003

10 Boehman, A.; Song, J.; and Alam, M., "Impact of Biodiesel Blending on Diesel Soot and the Regeneration of Particulate Filters," *Energy & Fuels*, Vol. 19 pp 1875-1864, American Chemical Society, 2005

11 Ahmad, T.; Plee, S., "Application of flame temperature to emissions from a direct injection diesel engine," SAE Paper 831734, *SAE International*, 1983

12 Easley, W.; Mellor, A., "Flame temperature correlation of emissions from diesels operated on alternative fuels," SAE Paper 2001-01-2014, *SAE International*, 2001

13 Liu, Z. G.; Ford, D.; Vasys, V.; Chen, D.; and Johnson, T.; "Influence of Engine Operating Conditions on Diesel Particulate Matter Emissions in Relation to Transient and Steady-State Conditions," *Environmental Science and Technology*, Vol. 41, pp. 4593-4599, 2007

14 Kim, D.; Gautam, M.; Gera, D.; "Parametric studies on the formation of diesel particulate matter via nucleation and coagulation modes," *Journal of Aerosol Science*, Vol. 33, pp 1609-1621, Elsevier, 2002

15 Kittelson, D.; Pui, D.; and Moon, K., "Electrostatic Collection of Diesel Particles," SAE Paper 860009, *SAE International*, 1986

16 Schweimer, G., "Ion Probe in the Exhaust Manifold of Diesel Engines," SAE Paper 860012, *SAE International*, 1986.

17 Harris, S., and Maricq, M.; "Signature size distributions for diesel and gaoline engine exhaust particulate matter," *Journal of Aerosol Science*, Vol 32, pp. 749-764, Elsevier, 2001

18 Mende, T.; Ando, R.; Nagat, M.; Kato, H.; and Kusaka, J., "Detailed analysis of particulate matter emitted from biofueled diesel combustion with high EGR," SAE Paper 2009-01-0483, *SAE International*, 2009

19 Ardenese, R.; Ardenese, M.; Besch, M.; Adams, T.; Thiruvengadam, A.; Shade, B.; Gautam, M.; Oshinuga, A.; Miyasato, M.; "PM Concentration and Size Distributions from Heavy-duty Diesel Engine Programmed with Different Engine-out Calibrations to Meet the 2010 Emissions Limits," SAE Paper 2009-01-1183, *SAE International*, 2009

20 Brown, E.; Clayton, M.; Harris, B.; and King, F., "Compasion of the Particle Size Distribution of Heavy-Duty Diesel Exhaust Using a Dilution Tailpipe Sampler and an In-Plume Sampler during On-Road Operation." *Journal of the Air & Waste Management Association (1995)*, Vol. 50, Issue 8 (August 2000), pp.1407-16, *Academic Search Complete*, EBSCO*host* (accessed July 31, 2009)

21 U.S EPA, Code of Federal Regulations, Title 40, Section 80, "Control of Emissions of Air Pollution From Diesel Fuel", July 2005 revision.

22 Kreso, A.; Johnson, J.; Gratz, L.; Bagley, S; and Leddy, D., "A Study of the Effects of Exhaust Gas Recirculation on Heavy-Duty Diesel Engine Emissions," SAE Paper 981422, *SAE International*, 1998

23 Ladammatos, N.; Abdelhalim, S.; and Zhao, H., "The effects of exhaust gas recirculation on diesel combustion and emissions," *Journal of Engine Research*, Vol. 1, *IMechE*, 2000

24 Zhu, J.; Lee, K., "Effects of Exhaust Gas Recirculation on Particulate Morphology for a Light-Duty Diesel Engine," SAE Paper 2005-01-0195, *SAE International*, 2005

25 Desantes, J.; Bermudez, Garcia, J.; and Fuentes, E., "Effects of current engine strategies on the exhaust of aerosol particle size distribution from a Heavy-Duty Diesel Engine," *Journal of Aerosol Science*, Vol 36, pp 1251-1276, Elsevier, 2005

26 Wagner, R.; Green, J,; Storey, J.; and Draw, S., "Extending Exhaust Gas Recirculation in Diesel Engines," Oak Ridge National Laboratory Internal Paper, 2000

27 Lee, K.; Zhu, J.; Song, J., "Effects of exhaust gas recirculation on diesel particulate matter morphology and $NO_x$ emissions," *Journal of Engine Research*, Vol. 9, *IMechE, 2008*

28 Wei, P., Porter, S., Harvey, N., Nobutaka, K., Khalek, I., Bougher, T., "Diesel Exhaust Particulate Sampler for On-board PM Measurement," SAE Paper 2008-01-1180, *SAE International*, 2008

29 Black, J.; Eastwood, P.; Tufail, K.; Winstanley, T.; Hardalupas, Y.; Taylor, A., "Inter-Correlations between smoke opacity, Legal Particulate Sampling (LPS), and TEOM, during transient operation of a diesel engine", SAE Paper 2007-01-2060, *SAE International*, 2007.

30 Booker, D., Giannelli, R., Hu, J., "Road Test of an On-Board Particulate Matter Mass Measurement System," SAE Paper 2007-01-1116, *SAE International*, 2007

31 Gheorgiu, V.; Ueberschär, D.; Zikoridse, G., "Soot Senor for Diesel Emission Onboard Control Systems," SAE Paper 2006-05-0821, *SAE International*, 2006

32 Sandig, R.; and Zikoridse, G., "Partikelsensoren zur Überwachung der DPF-Funktion-Ergebnisse der Felderprobung an Off-Road-Maschinen," FAD-Konferenz *Herausforderun Abgasnachbhandlung für Dieselmotoren*, Dresden 2008

33 Mehta, D.; Alger, T.; Hall, M.; Matthews, R., "Particulate Characterization of a DISI Research Engine using a Nephelometer and In-Cylinder Visualization," SAE Paper 2001-01-1976, *SAE International*, 2001

34 Warey, Al.; Huang, Y.; Matthews, R.; Hall, M., "Effects of Piston Wetting on Size and Mass of Particulate Matter Emissions in a DISI Engine," SAE Paper 2002-01-1140, *SAE International*, 2002

35 Hunt, A.; Quimby-Hunt, M.; Shepherd, I., "Diesel Exhaust Particle Characterization by Polarized Light Scattering," SAE Paper 982629, *SAE International*, 1998

36 Cai, W., and Ma, L., "Numerical investigation of an optical soot sensor for modern diesel engines," SAE Paper 2009-01-1514, *SAE International*, 2009

37 Rose, D., and Boger, T., "Different approaches to soot estimation as key requirement for DPF applications," SAE Paper 2009-01-1262, *SAE International*, 2009

38 Kingery, W.; Bowen, H.; and Uhlmann, D., Introduction to Ceramics, 2nd Ed., John Wiley & Sons, New York, 1976

39 Diller, T.T., Hall, M.J., and Matthews, R.D. "Further Development of an Electronic Particulate Matter Sensor and Its Application to Diesel Engine Transients," SAE Paper 2008-01-1065, *SAE International*, 2008.

40 Hall, M.J., Diller, T.T., and Matthews, R.D. "Fast-response electronic particulate matter sensor for diesel engine control and DPF failure detection," *8th International Symposium on Combustion Diagnostics*, ISBN 978-3-00-022057-9, Editor Peter Ziegler, AVL Europe, Baden-Baden, Germany, June 10-11, 2008.

41 Diller, T.; Osara, J.; Hall, M., and Matthews, R, "Electronic Particulate Matter Sensor – Mechanisms and Application in a Modern Light-Duty Diesel Vehicle," SAE Paper 2009-01-0657, *SAE International*, 2009

42 Diller, T.; Hall, M.; Matthews, R.; Steppan, J.; Henderson, B., "Behavior of an electronic soot sensor and its use in on-board diagnostic for a diesel particulate filter," submitted for review SAE-10PFL-1063, *SAE International*, for publication in 2010

43 Warey, A., "Development of an Electronic Sensor for Engine Exhaust Particulate Measurements," *Doctoral Dissertation*, The University of Texas at Austin, 2005

44 Warey, A; Hendrix, B.; Hall, M.; and Nevius, T., "A New Sensor for On-Board Detection of Particulate Carbon Mass Emissions from Engines," SAE Paper 2004-01-2906, also in *Journal of Fuels and Lubricants*, Vol. 4, 2004

45 Warey, A.; and Hall, M., "Performance Characteristics of a New On-Board Engine Exhaust Particulate Matter Sensor," SAE Paper 2005-01-3792, also in *Journal of Fuels and Lubricants*, Vol. 5, 2005

46 Modi, A.; Koratkar, N.; Lass, E.; Wei, B., and Ajayan, P. "Miniaturized gas ionization sensors using carbon nanotubes," *Nature* 424: 171-174, 2003.

47 Parker, K., Electrical Operation of Electrostatic Precipitators, The Inst. Of Engineering and Technology, Stevenage, ISBN:9780863419850, 2002.

48 Bohm, J., Electrostatic Precipitators, Elsevier, New York, 1982.

49 Fridman, A. and Kennedy, L.A., Plasma Physics and Engineering, Taylor and Francis, New York, 2004

50 Mitchner, M., and Kruger, C, Partially ionized gases, Wiley, New York, 1973

51 Kelly, E. G., and Spottiswood, D.J., "The theory of electrostatic separations: a review part II: particle charging," *Minerals Engineering*, Vol. 2 No. 2, pp193-205, Elsevier, 1989

52 Liu, B. Y., and Yeh, H. C. "On the Theory of Charging Aerosol Particles in an Electric Field," *Journal of Applied Physics*, Vol. 39, No. 3, 1968

53 Collings, N.; Baker, N.; and Wolber,. W.G., "Real Time Smoke Sensor for Diesel Engines," SAE Paper 860157, *SAE International*, 1986

54 Hong, G., Collings, N., Baker, N. J., "Diesel Smoke Transient Control Using a Real-Time Smoke Sensor," SAE Paper 871629, *SAE International*, 1987

55 Van Gulijk, C,; Marijnissen, J.; Makkee, M.; Moulijn, J.; and Schmidt-Ott; A., "Measuring diesel soot with a scanning mobility particle sizer and an electrical low-pressure impactor: performance assessment with a model for fractal-like agglomerates," *Journal of Aerosol Science*, Vol. 5, No. 5, pp633-655, Elsevier, 2003

56 Burtscher, H., "Physical characterization of particulate emissions from diesel engines: a review," *Journal of Aerosol Science*, Vol 36, pp. 896-932, Elsevier, 2005

57 Cochet, R., "Lois Charges des Fines Particules," *Coll. Int. la Physique des Forces Electrostatiques et Leur Application*, Centre National de la Recherche Scientifique, Paris, 1961

58 Shin, J., and Raja, L., "Dynamics of pulse phenomena in helium dielectric barrier atmospheric-pressure glow discharges," *Journal of Applied Physics*, Vol. 94, No. 12, 2003

# VITA

Timothy Thomas Diller is a native of Austin, Texas, where he attended The University of Texas at Austin starting in 1992, studying a combined course of Mechanical Engineering and German. In 1997, he received his Bachelor of Science degree in Mechanical Engineering, and after working for one year at Spectra Consulting Engineers in Austin, Texas, he entered Course 2 (Mechanical Engineering) at the Massachusetts Institute of Technology in Cambridge, Massachusetts. He received a Master of Science degree from the Massachusetts Institute of Technology in June of 2001. From January of 2001 through January of 2006, he worked at the Michelin Americas Research and Development Corporation in Greenville, South Carolina. In January of 2006, he entered the Graduate School at The University of Texas at Austin to pursue his doctoral degree in Mechanical Engineering.

Dr. Diller may be reached by email at timdiller@gmail.com

This manuscript was typed by the author.